A Single-Colour Spectroscopic Sensor for Monitoring Detergent- and Protein- Induced Vesicle Damage

Claudia Mae Fox Andrews

MSc by Research

University of York

Physics, Engineering and Technology

November 2025

Abstract

Detergent-induced membrane solubilisation is important for several biotechnological applications including cell lysis, virus inactivation and membrane protein extraction. Despite its significance, the mechanistic details remain largely underexplored, owing in part to a lack of suitable technologies that can investigate solubilisation events on the nanoscale. In this work, the use of intramembrane fluorescence de-quenching is presented as a sensitive technique for monitoring the interaction between detergent- and protein-vesicle interactions. The adaptability of this assay is showcased across a range of membrane-bound dye concentrations, surfactant conditions and model membrane vesicles of various sizes and compositions and its utility as a spectroscopic nanoruler is highlighted for a wide variety of biotechnological applications. Using a combination of time correlated single photon counting and fluorescence spectroscopy techniques, this thesis reveals that the widely used detergent Triton X-100 triggers the structural remodelling of lipid vesicles, even at concentrations below its critical micellar concentration, and confirms that vesicle swelling occurs before complete micellization. The study demonstrates that the progressive addition of Triton X-100, results in an enhancement of DiI's fluorescence lifetime, and that this parameter can be used to quantify morphological changes and membrane restructuring events. These conformational changes were also probed using single-vesicle imaging techniques, which confirm the expansion and highlight the formation of toroids before complete solubilisation. The sensitivity of the de-quenching approach can therefore provide a platform for exploring a wide variety of membrane perturbations with important biomedical significance. In this context, preliminary investigations highlight that the fluorescence de-quenching technique can also be utilised to probe the disturbance of lipid vesicles by Amyloid-beta (1-42) aggregates, which are major hallmarks of Alzheimer's Disease. Overall, the single-colour fluorescence de-quenching approach is a robust, sensitive and generalizable tool for detecting nanoscale membrane remodelling events and can be used to resolve detergent- and protein-induced membrane intermediates.

Author’s Declaration

I declare that this thesis is a presentation of original work, and I am the sole author. This work has not previously been presented for a degree or other qualification at this University or elsewhere. All sources are acknowledged as references.

Table of Contents

List of Tables

TABLE **Page**

List of Figures

FIGURE **Page**

Nomenclature

Aβ Amyloid-beta

$Aβ_{1-42}$ Amyloid-beta (1-42)

AD Alzheimer's Disease

CMC Critical Micelle Concentration

DiI 1,1'-Dioctadecyl-3,3,3',3'-Tetramethylindocarbocyanine Perchlorate

DiD 1,1'-dioctadecyl-3,3,3',3'-tetramethy-lindodicarbocyanine 4-chlorobenzenesulfonate salt

DLS Dynamic Light Scattering

DMSO Dimethyl sulfoxide

FRET Förster Resonance Energy Transfer

GUVs Giant Unilamellar Vesicles

HFIP 1,1,1,3,3,3-Hexafluoro-2-propanol

LUVs Large Unilamellar Vesicles

Micro-PL Micro-Photoluminescence

MLV – Multilamellar vesicles

POPC 1-palmitoyl-2-oleoyl-glycero-3-phosphocholine

POPS 1-palmitoyl-2oleoyl-sn-glycero-3-phospho-L-serine

SEM Scanning Electron Microscopy

SSPE Saline-sodium Phosphate-EDTA

SvFLIM Single Vesicle Fluorescence Lifetime Imaging

TCSPC Time-correlated Single Photon Counting

SDS Sodium dodecyl sulfate

TRIS Tris(hydroxymethyl)aminomethane

TX-100 Triton X-100

List of Publications

List of published journal articles from work in this thesis:

- Claudia M.F. Andrews, Christopher M. Hofmair, Lauryn Roberts, Emily James, Katie Morris, Kevin Kramm, Mark C. Leake, Yue Wang, Steven D. Quinn. Detergent-Triggered Membrane Remodelling Monitored via Intramembrane Fluorescence De-Quenching. *ACS Omega* 11 (3): 4465-4474 (2026)

1. Introduction

1.1 General Overview of Thesis

In this thesis, the use of model membrane vesicles and the mechanism of their interactions with both amphiphilic detergent molecules and proteins will be discussed. In particular, a new single-colour assay based on fluorescence de-quenching is introduced, which enables detergent- and protein-induced vesicle disruption on the nanoscale to be assessed. The interaction between large unilamellar vesicles, sized between 100 nm and 1 μm, with the non-ionic detergent Triton X-100 and the small peptide amyloid-beta (Aβ) which is heavily implicated in Alzheimer's Disease is discussed.

In this chapter, the motivation for such investigations is provided and a summary of previous literature in the field of membrane solubilisation and interactions of membranes with detergents and proteins is explored. Additionally, the contribution of Aβ towards Alzheimer's Disease progression is discussed, with key mechanisms for toxicity highlighted. In Chapter 2, experimental techniques and analysis methods used in this thesis to investigate membrane interactions with both detergents and Aβ are described. Chapter 3 then introduces the single-colour fluorescence de-quenching assay and provides a series of results which demonstrate its sensitivity and adaptability towards investigating the impact of environmental variables such as vesicle curvature on the detergent-induced vesicle solubilisation pathway. Importantly, this Chapter demonstrates that single in-tact vesicles expand prior to lysis and micellization – a key finding that refines the existing multi-stage model of detergent-induced membrane solubilisation. Using this optimised assay, Chapter 4 then examines the interaction between large unilamellar vesicles and Aβ, providing evidence for Aβ-induced morphological changes that parallels a disruption mechanism of detergents. Each Chapter of results also discusses these findings and considers future perspectives.

1.2 Detergent-induced membrane solubilisation

1.2.1 Detergents

In molecular biology, a detergent is a molecule that lowers the surface tension or the interfacial tension between two liquids, or a liquid and solid or gas (*1*). Their capability to reduce surface tension is due to their amphiphilic nature. This means that these molecules consist of a hydrophilic head and a hydrophobic tail where, as the hydrocarbon tail increases in chain length, the hydrophobicity of the molecule increases (*2*). Detergents are broadly classified into four basic types, dependent on their headgroup. Non-ionic detergents have an uncharged headgroup which limits their ability to break protein-protein interactions (*3*). Because of this property, they are non-denaturing and play important roles in isolating active membrane proteins, as well as being effective in processes where keeping protein structure intact is important such as drug delivery (*4*, *5*). Within this thesis the detergents Triton X-100 and Tween20 are used as examples of non-ionic detergents. In comparison, ionic detergents contain a charged head group and can be further classified into anionic and cationic, which have a negative and positive charged head group respectively (*6*). The latter generally exhibit stronger effects due to their ability to bind to protein molecules and alter the protein charge and structure. Ionic detergents are typically used for protein solubilisation and cell lysis, with the anionic surfactant sodium dodecyl sulfate (SDS) in particular having applications in gel electrophoresis (*7*–*9*). Finally, zwitterionic detergents contain both negatively and positively charged regions within the structure, and similarly to non-ionic detergents, they have a net neutral charge. This makes them more efficient at breaking protein-protein bonds, similar to ionic detergents, but the effect is less harsh (*10*). Zwitterionic detergents therefore have many useful properties in science such as electrophoresis, and the solubilisation of organelles (*11*, *12*). Generally, the hydrophilic head group is responsible for solubilization of the membrane by dissociating most lipid-protein and protein-protein interactions, allowing physical separation of both proteins and lipids. Different detergents have different tendencies to interact with biomembranes, and this property is primarily dependent on their molecular structure, amphiphilic characteristics and ability to intercalate between lipids (*13*).

Within this set of experiments, the use of three different detergents and their capability to solubilise model-membrane vesicles will be assessed. These are Triton X-100, Tween20 and SDS. The corresponding chemical structures can be seen in Figure 1.1. Triton X-100 (TX-100) is a typical non-ionic detergent used in the study of biomembranes. It plays important roles in the lysing of cells for protein extraction and cellular organelles, as well as permeabilising living cell membranes for transfection (*14*, *15*). This is due, in part, to its non-denaturing nature. It is composed of a hydrophilic polyethylene oxide chain and an aromatic hydrocarbon hydrophobic group (Figure 1.1A). Typical self-assembly of micelles by TX-100 results in the hydrocarbon chain packed in the interior of the micellar core and the hydrophilic chains remaining outside the micelle (*16*, *17*). The formation of these micelles occurs around 0.2 - 0.3 mM in solution (*18*). Tween20, chemically known as Polysorbate20, is another common choice for a non-ionic detergent. It is often used as a solubilising agent of membrane proteins making it useful for protein extraction, cell lysis and enzyme reactions, as well as enhancing drug permeability in pharmaceuticals (*19–21*). It is derived from the addition of ethylene oxide to sorbitol esters, with the polyoxyethylene chains contributing to the hydrophilic portion and the oleic acids forming the hydrophobic parts (Figure 1.1B). Tween20 typically contains between 20 to 30 units of ethylene oxide per molecule. The reported critical micellar concentration (CMC) of Tween20 is 0.06 - 0.07 mM (*22*). The final detergent used within these experiments is SDS. It is a strong ionic detergent that is primarily used for the rapid disruption of biological membranes. Its most notable application in biotechnology is during protein separation techniques such as SDS-page due to ability to break down proteins' tertiary and quaternary structure. SDS is comprised of a 12-carbon hydrocarbon chain attached to a sulfate group, with sodium ions contributing to its ionic property (Figure 1.1C). In comparison to the other non-ionic detergents, the CMC is relatively high, occurring between 8.2 – 10 mM (*23*). This is due to the head group of SDS having a high negative charge which increases the electrostatic repulsion in the molecule and means that higher concentrations of the detergents are required to form micelles.

(A) Triton X-100

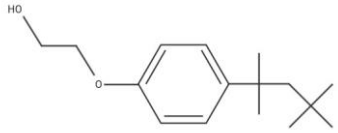

(B) Tween20

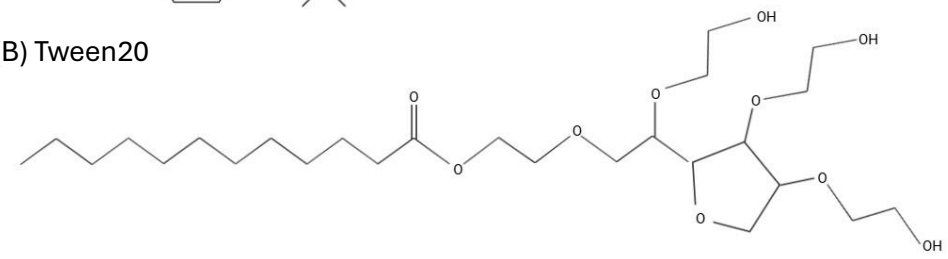

(C) Sodium Dodecyl Sulfate

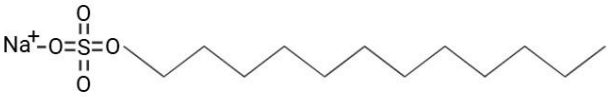

FIGURE 1.1 Chemical structures of detergents used in this study. A) Triton X-100 B) Tween20 and C) Sodium Dodecyl Sulfate.

1.2.2 Three State Model of Solubilisation

The generally accepted model of membrane solubilisation by detergents is a 3-state process (*24*) (Figure 1.2). During state 1, detergent monomers partition the bilayer until a saturation value is reached, causing membranes and vesicles to increase in mass and turbidity. Following this, in state 2, the membrane begins to disintegrate and break into mixed detergent-lipid micelles coexisting within the bilayer. In state 3, the mixed micelles are released into the solution and the membrane solubilises. The formation of mixed micelles occurs at the detergent's CMC which, rather than being a unique quality, encompasses a narrow range of concentrations (*25*). This model is further supported by various thermodynamic studies of vesicle-detergent interactions, microscopy and spectroscopy experiments, and more recently fluorescence-based analysis (*26–29*). Multiple factors can influence the CMC of detergents such as the hydrophobicity of the tail, the introduction of double bonds or branching points, and the charge of the surfactant (*30*, *31*). Typically, non-ionic surfactants have lower CMCs due to there being less electrostatic repulsion between molecules, allowing them to aggregate and form micelles at lower concentrations (*32*, *33*). A crucial step in the process of solubilising the membrane components is the movement of the detergent molecules from one side of

the bilayer to the other (*34*, *35*). This trans-bilayer movement is commonly denoted "flip-flop". Only detergents that can flip between the inner and outer monolayers can cause rapid solubilisation of a detergent saturated bilayer (*36*). When the detergent cannot flip into the inner monolayer, it accumulates on the outer monolayer and causes it to become unstable due to mass imbalance. In comparison, the incorporation of detergents increases the spontaneous curvature of the phospholipid and causes the outer monolayer to form mixed micelle structures (*37–39*). This is due to the imbalance between a detergents curvophilic nature and a phospholipid's tendency to self-assemble along a flat surface. Shedding of these micelles into the aqueous solution results in partial solubilisation, and the consequent leakage of detergent results in trans-membrane equilibrium of detergent and subsequent micellization through a rapid bilayer saturation mechanism. The flip-flop mechanism is often the rate limiting step in bilayer solubilisation and can help further classify detergents into either fast or slow solubilising (*40*). Fast solubilising detergents can incorporate into the bilayer at a higher rate and results in the 3-state model, as previously described, whereas slow solubilising detergents are more likely to induce high curvature stress prior to complete solubilisation (*41*, *42*). For example, TX-100 has a fast flip-flop rate in comparison to Tween20 and SDS, which are considered slow solubilising detergents.

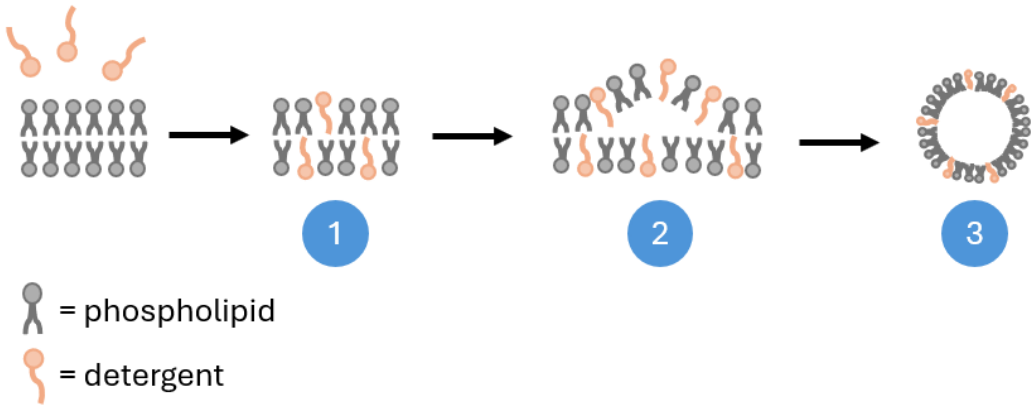

FIGURE 1.2 Membrane Solubilisation by detergents 1) Incorporation of amphiphilic detergent monomers into the phospholipid bilayer 2) Fragmentation within the bilayer. 3) Release of mixed micelles into the solution and solubilisation of the membrane.

1.3 Techniques to Study Changes to the Membrane

1.3.1 Model membranes

The use of unilamellar vesicles provides a simplified model of membranes that allow researchers to analyse systems in a controlled environment (*43*). These synthetic models consists of a spherical liposome bounded by a single bilayer of amphiphilic phospholipid molecules (Figure 1.3). The contrasting hydrophobic and hydrophilic zones of the lipids creates a hydrophobic effect that promotes their molecular aggregation in an aqueous environment (*44*). Their hydrophilic headgroups point towards the vesicle's exterior and interior, and their hydrophobic tails point towards the centre of the bilayer.

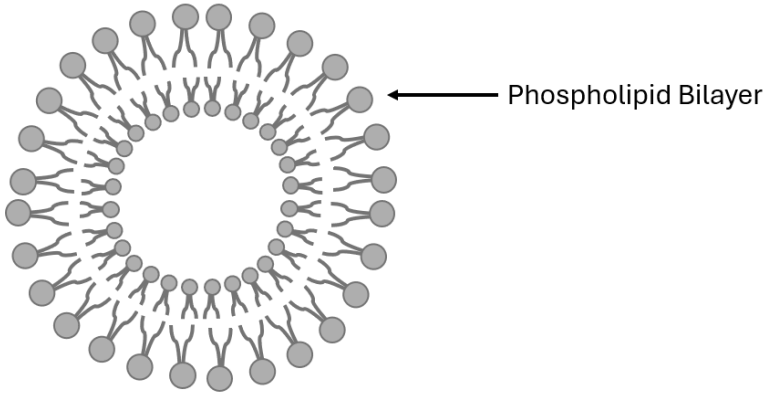

FIGURE 1.3 Diagram of a unilamellar vesicle.

These unilamellar vesicles are classified according to their size, with vesicles that are smaller than 100 nm in diameter classified as small unilamellar vesicles (SUVs), those that are greater than 100 nm classified as large unilamellar vesicles (LUVs) and species greater than 1 micron are classified as giant unilamellar vesicles (GUVs) (*45*). Typically, the size of these vesicles are best determined using dynamic light scattering (DLS) and nanoparticle tracking analysis (NTA) techniques (*46*, *47*). The different vesicle classifications possess properties that make each advantageous for different reasons. Specifically, SUVs are commonly used as drug delivery vehicles due to their ability to encapsulate single molecules and their small size allows them to penetrate better into tissues and cells (*48*). In comparison, LUVs and GUVs are often utilised in research as simplified models of extracellular vesicles and cell membranes respectively. In the case

of the latter, their size is comparable to eukaryotic cells (*43*, *49*). The use of LUVs and GUVs allows for the study of lipid-detergent and lipid-protein interactions in a controlled environment where the membrane properties can be tuned. For example, the molecular composition can be easily changed - altering features such as membrane thickness and charge by changing the phospholipid species or by incorporating additional lipids into the membrane. A commonly used lipid composition for the simple study of membrane interactions is 1-palmitoyl-2-oleoylphosphatidylcholine (POPC). POPC is a zwitterionic phospholipid, resulting in a net neutral charge at physiological pH. It is often the lipid of choice due to its biological relevance in eukaryotic cell membranes, as Phosphatidylcholine (PC) is the most abundant lipid in mammalian cell membranes (*50*).

1.3.2 Non-fluorescence Techniques

While extensive research has been undertaken to define the general mechanism of detergent-induced solubilisation, key information detailing each stage of the model is yet to be fully explored. Many of the mechanistic and kinetic details regarding vesicle behaviour prior to complete solubilisation remains largely unexplored, owing in part to a lack of suitable technologies capable of assessing nanoscale disruption events. This leaves some unanswered questions such as: How do detergents interact with and remodel membranes prior to complete solubilisation? What is the sequence of morphological transitions that lead up to complete solubilisation? And how do these processes vary across detergent and lipid types?

Techniques such as Cryo-EM and dynamic light scattering have been able to provide snapshots into membrane conformation but they lack the ability to provide dynamic information (*51*). For example, the use of these techniques was able to show the formation of mixed-micelles from 100 nm LUVs with the addition of TX-100 by restructuring the vesicles (*52*). Additionally, this structural remodelling was seen during a transitional phase, after state 2 of the conventional model of solubilisation, which alters the vesicles structure and integrity. (*53*). This reshaping has been supported by an observed swelling prior to solubilisation, seen using quartz crystal microbalance with dissipation (QCM-D) monitoring of surface tethered vesicles with the addition of Tween20. This indicated that the vesicles increase in mass and turbidity, and this likely takes place concurrently with permeabilization and membrane fusion events (*29*, *54*, *55*).

For example, the non-ionic detergent Tween20 has been shown to trigger structural remodelling which precedes a loss of material to the solution prior to lysis even at concentrations below the reported CMC (*53*). Furthermore, TX-100 induces LUV fusion in vitro by altering the configuration and integrity of freely diffusing and surface immobilised vesicles via a mechanism involving docking, hemifusion, content exchange and full lipid mixing prior to solubilisation and lysis (*54*).

1.3.3 Fluorescence

Fluorescence based techniques have become an increasingly popular approach with wide ranging impacts in molecular cell biology, biophysics and genomics (*56–58*). In particular, these techniques have been used to study detergent-membrane interactions due to its increased sensitivity compared to non-fluorescent methods. For example, the use of fluorescent imaging previously suggested that TX-100 has a restructuring effect on the organisation of phospholipids in GUVs and selectively solubilises the membrane (*59*, *60*). Fluorescence intensity measurements were also used to characterise the behaviour of different detergents and show that the flip-flop motion is dependent on the formation of hydrophobic structural defects in the membrane (*27*, *61*). These techniques use fluorescence dyes known as fluorophores to detect biomolecular components with high selectivity and sensitivity – making it an increasingly popular choice for reporting on the changes described previously (*62*). Fluorophores are chemical compounds that, upon excitation from a distinct wavelength of light, emit photons of fluorescence (*63*). The incident wavelength must correspond to the energetic difference between the initial ground state (S0) and a higher excited singlet state (S2). When this occurs, an electron within the molecule is promoted to the S2 state where it remains for a short period of time. Whilst in an excited state, the electron is considered energetically unstable and will decay to a lower energy level through several relaxation pathways. Two main methods of dissipating energy are non-radiative and do not result in the emission of photons – known as internal conversion and vibrational relaxation (*64–66*). These processes typically occur within picoseconds (10^{-12}s). During vibrational relaxation, the electron decays to the lowest energy level of its current excited singlet state by transferring vibrational energy to nearby molecules, whereas during internal conversion, the electron transitions between singlet states to a lower energy state due to a relatively small energy gap between the two

e.g. S2 to S1. By contrast, fluorescence is emitted as the electron radiatively de-excites back to the ground state – dissipating its energy in the form of a fluorescent photon of longer wavelength than the excitation photon over the course of nanoseconds (10^{-9}s) (*67*) (Figure 1.4). The difference in wavelength between the excitation and emission photon is deemed Stokes shift which is fundamental to the sensitivity of fluorescence techniques.

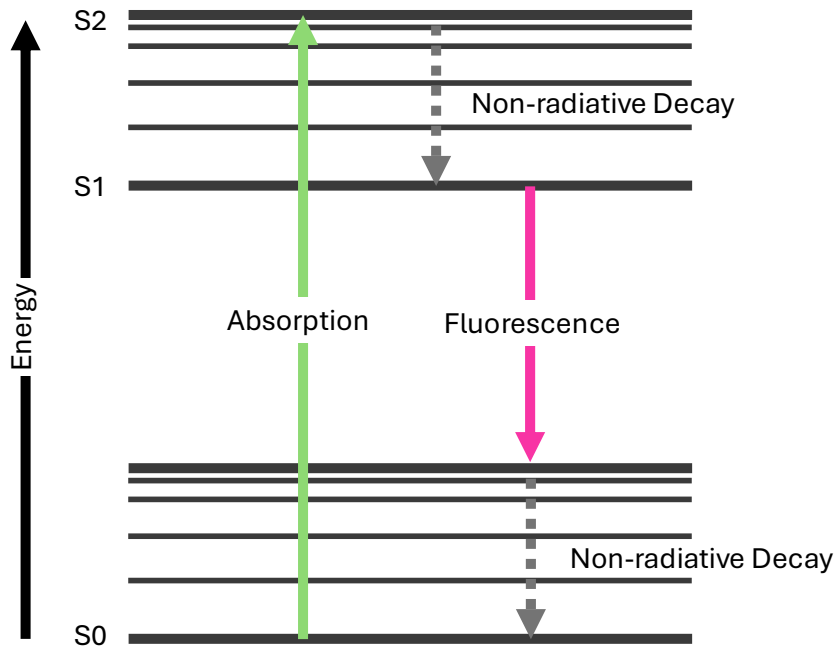

FIGURE 1.4 Jablonski diagram showing the excitation of a single photon to a higher state S_2, followed by vibrational relaxation allowing the electron to move to the lower sublevel S_1. As the electron returns to ground state S_0, a fluorescent photon is emitted at a longer wavelength.

The average amount of time a molecule spends in this excited state is known as the fluorescence lifetime of the excited state (τ), and this can be evaluated using time correlated single photon counting. Here, a short pulse (typically ps) of light excites the sample, and the time it takes for individual photons is recorded. These arrival times are binned into a histogram, and the fluorescence decay is analysed using the Equation 1.1 to extract τ,

$$\boldsymbol{I(t) = I_0 \exp\left(-t/\tau\right)} \qquad (1.1)$$

where I(t) is the time-dependent intensity at time t, and I_0 is the intensity at t=0. If more than one excited state is present, the sample can exhibit multiple decay times. This can occur due to reasons such as different local environments, which is likely when fluorophores are placed in a vesicle bilayer. In this case, the fluorescence decay can be represented by a sum of exponentials according to Equation 1.2.

$$\boldsymbol{I(t) = \sum_{i}^{n} a_i \exp(-t/\tau_i)} \quad (1.2)$$

Where a is the pre-exponential factor representative of the number of fluorophores in each environment.

Typical fluorescence-based approaches involve the use of synthetic molecules such as 1,1'-Dioctadecyl-3,3,3',3'-Tetramethylindocarbocyanine Perchlorate (DiI) for biological labelling. DiI is a carbocyanine membrane dye that enhances fluorescence upon insertion of its lipophilic hydrocarbon chains into the lipid membrane of the cell. It consists of two indoline rings, connected by a three-carbon bridge, and two long alkyl chains attached to the nitrogen atoms of the rings (*68*). The alkyl chain consists of a conjugated-pi system and is essential for the delocalisation of electrons which allows the molecule to act as an electric dipole – absorbing and emitting light. The alternating double bonds results in smaller energy gaps and therefore excitation to higher energy state is easier. The spectral characteristics of carbocyanine dyes are determined by the heteroatoms in the terminal ring systems and the length of the connecting bridge, as opposed to chain length, as seen in (*69*). Upon excitation, DiI emits an orange-red fluorescence at a peak of 565 nm under 549 nm excitation (Figure 1.5A). DiI, whose structure is characterized by two long octadecyl chains attached to a tetramethylindocarbocyanine core (Figure 1.5B) acts as an effective reporter due to its low cell toxicity and its capability to easily embed into vesicles due to its hydrophobic tails. Furthermore, DiI has high photostability which means that the fluorescence intensity remains stable and allows for longer observations (*70*). For these reasons, DiI was chosen as the reporter of choice for all experiments following.

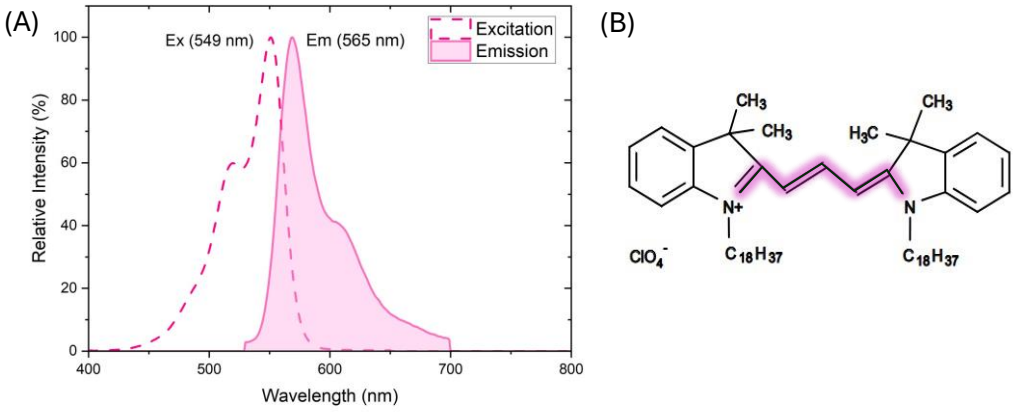

FIGURE 1.5 DiI Fluorescence (A) Spectral plots showing the excitation and emission profiles of DiI. Excitation and emission maxima and their corresponding wavelengths are overlaid. Data has been extracted from the ThermoFisher Scientific fluorescence SpectraViewer. (B) Chemical structure of DiI and the connecting bridge responsible for fluorescence.

1.3.4 Förster Resonance Energy Transfer

Many fluorescence experiments have highlighted the use of Förster resonance energy transfer (FRET)-based analysis to investigate the morphological changes induced by detergents. In this, the extent of energy transfer between a fluorescent donor and acceptor molecule can be attributed to the distance between them. A decrease in the efficiency of energy transfer per vesicle quantitatively reports an increase in vesicle surface area and this has been seen in LUVs labelled with DiI (donor) and DiD (acceptor) in the presence of detergents such as TX-100, Tween20 and SDS (*29*, *53*, *54*). In comparison, conventional optical imaging approaches only allow for visualisation of macroscopic changes in the vesicles and provide little detail on a molecular level. This is due to these techniques being limited by their resolution which typically only allows analysis of large objects with diameters above 5 - 10 µm, whereas FRET is sensitive to 1 - 10 nm distances between dyes (*71*). Despite its increasing popularity, FRET-based approaches for monitoring detergent- and protein-induced membrane damage are limited by requirements for precise donor-acceptor stoichiometry, donor bleed through into the acceptor emission channel, and issues associated with spectral overlap such as direct excitation of the acceptor under donor excitation (*72*). These limitations highlight

the requirement for an equally sensitive approach that can monitor nanoscopic disruption events, while bypassing the experimental complexity that is associated with alternative fluorescence-based methods.

1.3.5 Fluorescence De-quenching

In this work, the use of fluorescence de-quenching has been investigated as an alternate, single colour approach for the sensitive indication of nanoscale morphological changes in vesicles. This approach builds upon the self-quenching phenomenon that is seen from fluorophores, in which the intensity of fluorescence emission and lifetime decreases at high concentrations of fluorophore solution (*73*). This occurs due to various mechanisms such as the formation of non-fluorescence dimers, energy transfer to the non-fluorescent dimers and collision between excited fluorophores (*74–76*). In the context of a membrane where dyes are in close proximity and quenched, molecular events such as an increase in volume or permeability of the membrane causes the local concentration of fluorophores inside the membrane to decrease (*77*). In turn, this causes spatial increase between the probes, and a subsequent increase in fluorescence intensity due to a decrease in self-quenching. In summary, increasing the distance between quenched identical membrane-bound fluorophores leads to fluorescence de-quenching, resulting in increased fluorescence intensities of the probes. While fluorescence quenching and de-quenching has been used to monitor lipid-lipid interactions within the context of a supported lipid bilayer, the technique has not yet been applied to investigating the mechanism of detergent-induced membrane solubilisation. This study hypothesises that detergent-induced vesicle expansion and solubilisation can be evaluated by monitoring the fluorescence intensity and lifetime of membrane-bound probes, where molecular disruption events that increase the dye-dye separation distance would result in fluorescence de-quenching, as schematically illustrated in Figure 1.5. As the vesicle expands, the fluorescence intensity is predicted to increase up to a saturation value, corresponding to the formation of micelles. This would allow for real-time characterization of membrane damage and morphological changes on the nanoscopic level, whilst bypassing many of the limitations attributed to FRET-based approaches. While the fluorescence de-quenching approach will be used within this work to quantitively report on detergent-induced vesicle solubilisation, and to explore the

mechanistic details of the process, the technique could also be applied to protein-vesicle interactions that are implicated in disease.

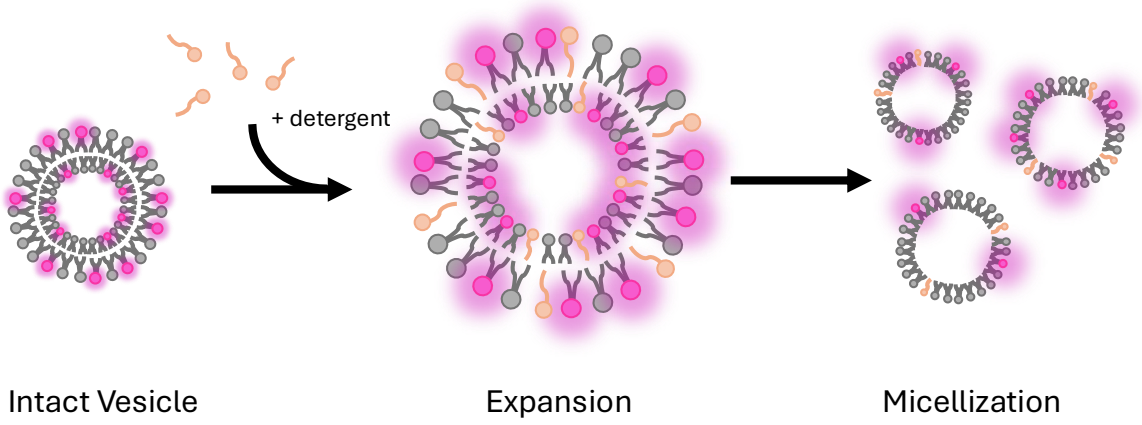

FIGURE 1.6 Schematic depicting the use of fluorescence de-quenching as a reporter of detergent-induced vesicle solubilisation. Detergent monomers incorporate into the bilayer of intact vesicles to induce swelling and micellization which increases the fluorescence intensity of the membrane-bound fluorophores.

1.4 The role of Amyloid-β in Alzheimer's Disease

1.4.1 Characterisation of Alzheimer's Disease

Alzheimer's Disease (AD) is a complex and progressive neurological disorder, characterised by a combination of behavioural and biological markers. Affected individuals experience a loss of cognitive and behavioural abilities such as memory loss, cognitive decline, language problems and ultimately lose the ability to perform simple everyday tasks (*78*, *79*). This can be difficult and distressing for both those directly and indirectly affected by the condition. It is estimated that 1 in 3 people will develop dementia in their lifetime, with projections in the UK predicted to exceed 1 million by 2030 (*80*, *81*). Furthermore, in 2024 dementia and AD wass the leading cause of death in the UK (*82*). This highlights the importance of research to improve our understanding of this disease.

AD is marked by an accumulation of intracellular neurofibrillary tangles and extracellular neuritic plaques in the cerebral cortex (*83*). It is known that the neurofibrillary tangles

contain insoluble aggregates of modified tau protein. Tau is a microtubule associated protein that is important for maintaining the integrity of neurons by stabilising microtubules within the axon and dendrites (*84*). When tau becomes abnormally hyperphosphorylated these microtubules disassemble, resulting in severe deposition of the variants. These free tau molecules aggregate into paired helical filaments and form the neurofibrillary tangles (*85*). This is one of the driving factors towards neuronal cell death. These mutations are suggested to occur due to disruption of cellular signalling resulting in an imbalance in activity of kinases and phosphatases (*86*). In AD, one of the main causes of this disruption is due to changes in amyloid-beta protein (Aβ) metabolism and initial plaque formation, causing an imbalance between the clearance and production of the protein (*87*). This leads to an abnormal build-up of Aβ plaques. This can lead to overactivation of kinases such as mitogen-activated protein kinases, tyrosine kinases and protein kinase C, which all contribute to tau hyperphosphorylation (*88–90*). Alzheimer's research has primarily focussed on this amyloid cascade hypothesis which suggests that the accumulation of Aβ peptides is responsible for a series of events leading to development of the disease, such as neuroinflammation and tau protein tangles (*91*, *92*). Because of this, focus has shifted towards better understanding the Aβ protein, and importantly, its interaction with neuronal membranes.

1.4.2 Amyloid-beta Aggregation

The typical Aβ plaque consists of a central deposit of extracellular amyloid fibrils, surrounded by dendritic neurites and accumulates due to mutations in the gene encoding amyloid-beta precursor protein (APP) (*93*). Aβ allomorphs are generated in the amyloidogenic pathway, in which APP is proteolytically processed by sequential cleavage by beta and gamma secretase (*94*). The two most common isoforms in the AD brain are $A\beta_{1-40}$ and $A\beta_{1-42}$ (*95*). Whilst the 40-residue peptide is more abundant, accounting of 90 – 95% of the population in AD, $A\beta_{1-42}$ is considered more cytotoxic and the main component of the senile plaques. $A\beta_{1-42}$ therefore has higher implications for disease progression (*96*). $A\beta_{1-42}$ contains two additional hydrophobic residues at the C-terminus in comparison to $A\beta_{1-40}$, making it less soluble and resulting in a higher tendency to aggregate at physiological pH (*97*).

The self-assembly of Aβ is a nucleation-dependent polymerisation process consisting of three main stages: nucleation, elongation, and equilibrium (*98*). The increase in mass of the aggregates during this process follows a sigmoidal profile, where an initial lag phase corresponds to nucleation and little change in aggregate concentration. This nucleation phase can be further divided into primary and secondary nucleation. During primary nucleation, nuclei form in spaces with no current aggregates whereas during secondary nucleation aggregation is promoted by the presence of existing aggregates (*99*, *100*). Often, primary nucleation is the rate limiting step in the production of amyloid fibrils (*101*). Following the lag phase is an elongation phase in which the profile becomes hyperbolic as more fibrillar growth occurs than nucleation. This phase continues until an equilibrium is reached and the rate of aggregate formation through nucleation balances the rate of breakdown (*102*). Aβ aggregates from singular, soluble monomers to insoluble fibrils with different intermediate aggregation stages between the two. This includes dimer and trimer, soluble oligomers, and protofibrils, as illustrated in Figure 1.6 (*103*). The self-assembly of amyloid is highly dependent on local environmental factors such as solution composition, temperature, pressure and pH (*104*).

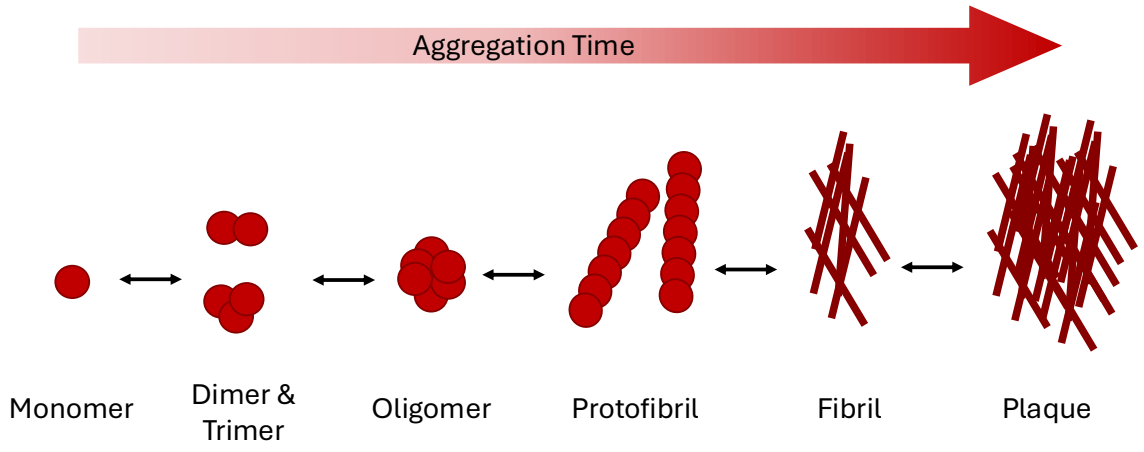

FIGURE 1.7 Schematic of Aβ self-assembly process. Aβ monomers self-assembly into more toxic aggregates as time increases.

The aggregation of Aβ results in the formation of protofibrils consisting of a cross beta structural pattern (*105*). These beta strands orientate perpendicular to the fibril axis and stack together with intermolecular, backbone hydrogen bonds stabilising the structure. -forming the fibrils. Amyloid fibrils are polymorphic structures and have been found to

form three different types of fibril network: amyloid star, bundle and meshwork (*106*). The amyloid star consists of fibrils that radiate out in different directions. The amyloid bundle consists of filaments aligned parallel to one another, and the amyloid meshwork consists of filaments with no obvious overall orientation (*107*). It was concluded that plaque formation is toxic to cells and can induce cell death via perforation of the membrane and lysis, although the interaction between these different networks requires further investigation to quantify (*108*).

1.4.3 Membrane Interactions and Disruption by Amyloid-beta

While previous research has indicated that aggregates of Aβ can directly disrupt the membrane, the precise mechanisms of toxicity have not been fully established (*109*). It has been suggested that Aβ interacts and permeabilises the membrane in four main mechanisms: ion-channel formation, receptor-binding, membrane carpeting or a detergent-like effect (*110*). The mechanism of disruption is highly dependent on the structure of the aggregate – with the oligomeric species being the most disruptive and capable of inducing these mechanisms (*111*). For example, Aβ oligomers have been shown to insert into the membrane to puncture and induce large single ion-channel formation (*112*). This has cytotoxic capabilities as it disrupts ion gradients which can result in lysis or swelling due to difference in osmotic pressure (*113*). Furthermore, changes in ion gradients results in altered cellular signalling which has implications towards disruption of the long-term potential and increases progression of the disease (*114*). Oligomers have also been suggested to bind to membrane-associated receptor proteins which disrupts signalling. In particular, accumulation of Aβ can cause dysregulation of α-amino-3-hydroxy-5-methyl-4-isoxazolepropionic (AMPA) and N-methyl-D-aspartate (NMDA) glutamate receptors which mediate fast excitatory neurotransmission – essential for synaptic plasticity and cognitive function (*115–117*). Additionally, this receptor binding can disturb cellular homeostasis and can lead to the generation of oxidative stress which further compromises membrane integrity (*118*). Whereas the previously described mechanisms of disruption are most commonly observed from amyloid oligomers, fibrillar isoforms of the protein perturb the membrane by embedding into the outer leaflet of the bilayer and altering the structure (*119*, *120*). This displacement of the membrane results in destabilisation and lipid extraction. The

final mechanism, and the main theme of this thesis, is the observed 'detergent-like' effect of oligomers. In this, the addition of amyloid is hypothesised to increase lipid curvature and membrane extraction following a process that mimics that seen by detergents (*121*). Although this disruption has been compared to the solubilisation of the membrane by detergents, the exact stages of the mechanism remains unexplored and it is unclear whether this also mirrors the 3 states of solubilisation previously described. For example, it is unknown whether amyloid induces membrane swelling prior to cell permeabilization.

1.5 Project Aims

This project aims to establish the use of intramembrane fluorescence de-quenching as a general platform for investigating the mechanistic stages of membrane solubilisation by different detergents and to showcase the adaptability and sensitivity of the technique for monitoring detergent-induced morphological changes on the nanoscopic level. This project aims to examine whether detergents such as TX-100 induce structural changes in LUVs below the critical micellar concentration and evaluate morphological transitions as intact vesicles proceed towards complete micellization. Furthermore, this project aims to explore the use of intramembrane fluorescence de-quenching as a tool for probing Aβ-induced membrane disruption.

In short, this work aims to provide the scientific community with a new, alternative, ultrasensitive fluorescence-based approach for detecting detergent- and protein-membrane interactions with important biotechnological and biomedical significance.

2. Materials and Methods

To investigate the de-quenching hypothesis, in which initially quenched fluorescent dyes in intact vesicles becomes progressively de-quenched with the addition of detergents, ensemble fluorescence spectroscopy, time-correlated single photon counting, and single vesicle micro-photoluminescence experiments were performed on fluorescently labelled model membrane vesicles. The adaptability of the assay was also assessed using varying detergents, dye concentrations, vesicle sizes and compositions. In addition to this, morphological changes induced by detergents were visualised using scanning electron microscopy. The de-quenching assay was then utilised to investigate interactions between Aβ(1-42) and model membranes using monomeric and aggregated forms of the peptide.

2.1 Materials

2.1.1 Buffers

All detergent experiments were performed in 50 mM Tris(hydroxymethyl)aminomethane (Tris) buffer, purchased from Sigma-Aldrich, with the pH adjusted to pH 8.0 with concentrated HCl prior to use. $A\beta_{1\text{-}42}$ aggregation experiments were performed in Saline-sodium phosphate-EDTA (SSPE) buffer composed of 150 mM sodium chloride, 10 mM sodium phosphate monobasic monohydrate and 1 mM ethylenediaminetetraacetic acid (EDTA), pH 7.4 and was purchased from Sigma-Aldrich.

2.1.2 Lipids and Fluorescent Dyes

2.1.2.1 Lipids

1-palmitoyl-2-oleoyl-glycero-3-phosphocholine (POPC) and 1-palmitoyl-2oleoyl-sn-glycero-3-phospho-L-serine (POPS) lipids, purchased from Merck, were supplied in chloroform at 10 mg/mL and stored at -20°C prior to use. Both lipid samples were used without any additional purification.

2.1.2.2 Fluorescent Dyes

Lipophilic membrane stains 1,1'-Dioctadecyl-3,3,3',3'-Tetramethylindocarbocyanine Perchlorate (DiI) and 1,1'-dioctadecyl-3,3,3',3'-tetramethy-lindodicarbocyanine 4-

chlorobenzenesulfonate salt (DiD) at 1 mM in ethanol, were purchased from ThermoFisher Scientific and stored at -20°C prior to use.

2.1.3 Detergents

All detergents used were purchased from Sigma-Aldrich and diluted in 50 mM Tris buffer (pH 8.0), previously described, to desired stock concentrations for the titrations. TX-100 was used in concentrations up to 0.6 mM from a stock solution of 20 mM, Tween-20 was used in concentrations up to 0.2 mM from a stock solution of 10 mM, and SDS was used in concentrations up to 4.0 mM from a stock solution of 100 mM.

2.1.4 Amyloid

$A\beta_{1-42}$ was purchased as lyophilized powder from Cambridge Biosciences and stored at -20°C prior to use. Dimethyl sulfoxide (DMSO), which was used for resuspending monomerized $A\beta_{1-42}$ was purchased from Sigma-Aldrich.

2.1.5 Surface Immobilisation Reagent

To immobilise the vesicles to microscope slides, 1% poly-L-lysine purchased from Sigma-Aldrich was used.

2.2 Methodology

2.2.1 Vesicle Preparation

2.2.1.1 Preparation of Large Unilamellar Vesicles

Homogenous, fluorescently labelled phospholipid vesicles were prepared by the extrusion method (*122*, *123*). In this protocol, the phospholipids and lipophilic dye DiI were homogenously dispersed in chloroform and evaporated using nitrogen flow. For exact amounts and concentrations used, see Table 2.1. The remaining lipid film was then rehydrated in 50mM Tris buffer solution (pH 8) and mixed well by vortex. During rehydration, the phospholipids and dyes self-assemble into multilamellar vesicles (MLVs) due to their amphiphilic behaviour (*124*). The MLVs were then selectively decreased in size by extrusion through a membrane filter with a defined pore size.

In this work, the Avanti mini extruder was used (Figure 2.1). The extruder is comprised of a stainless-steel outer casing and retainer nut which holds two internal membrane supports. Each of these supports contains an O-ring in which a 10 mm Whatman Nuclepore polyester filter disc is placed. These discs then further support a 19 mm Whatman Nuclepore polycarbonate membrane filter with a pore of distinct diameter. In these experiments, the following pore sizes were used: 30 nm, 200 nm, 400 nm, and 1 µm. The MLV solution was passed back and forth through the filter, using gas tight syringes 21 times to maximise LUV homogeneity (*125*). This technique is favourable for producing uniform LUVs as it is reliable and variables such as composition, dye content, and vesicle size can be easily changed. For all experiments, a final lipid concentration of 67 µg/mL was used.

Dye Concentration (mol%)	1.5	1	0.1	0.01
Volume of Dye (µL)	62.4	41.6	4.16	0.416

TABLE 2.1 Table of corresponding volumes of dye to create varying concentrations. The volume of dye (from 1 mM stock solution) used to create vesicles of varying dye concentrations. Quantities are relevant for 250 µL of POPC lipids and 500 µL of 50 mM pH8 Tris buffer used during extraction.

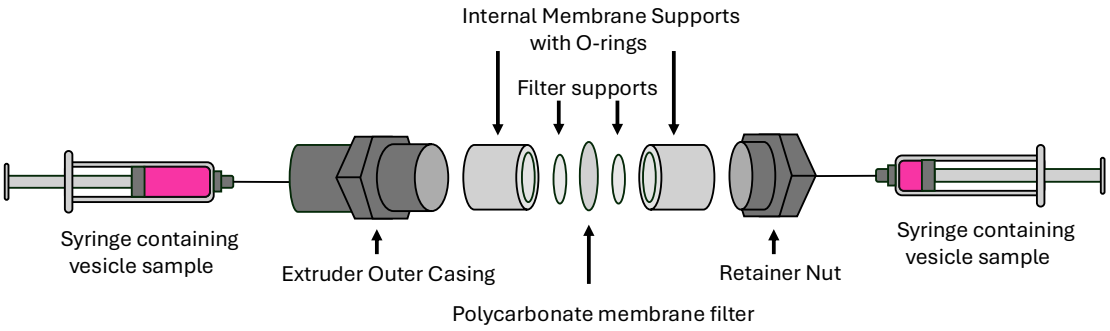

FIGURE 2.1 Schematic of Avanti Mini Extruder set-up. A diagram showing the internal components of the Avanti membrane extruder, with syringes on either side that pass fluid back and forth through the membrane.

2.2.1.2 Preparation of 50 % FRET Vesicles

POPC model membrane vesicles containing the lipophilic membrane dyes DiI and DiD were prepared using the extrusion method previously described and schematically shown in Figure 2.2, using a polycarbonate membrane filter with 200 nm pore size. In this, the quantities of donor (DiI) and acceptor (DiD) were optimised such has that average FRET efficiency per vesicle was initially close to 0.5, allowing for the estimation of nanometer length scale changes by observable variations in the FRET efficiency (*71*). For each dye, 0.2 mol% (0.1 mol% of each dye) was used following the volume seen in Table

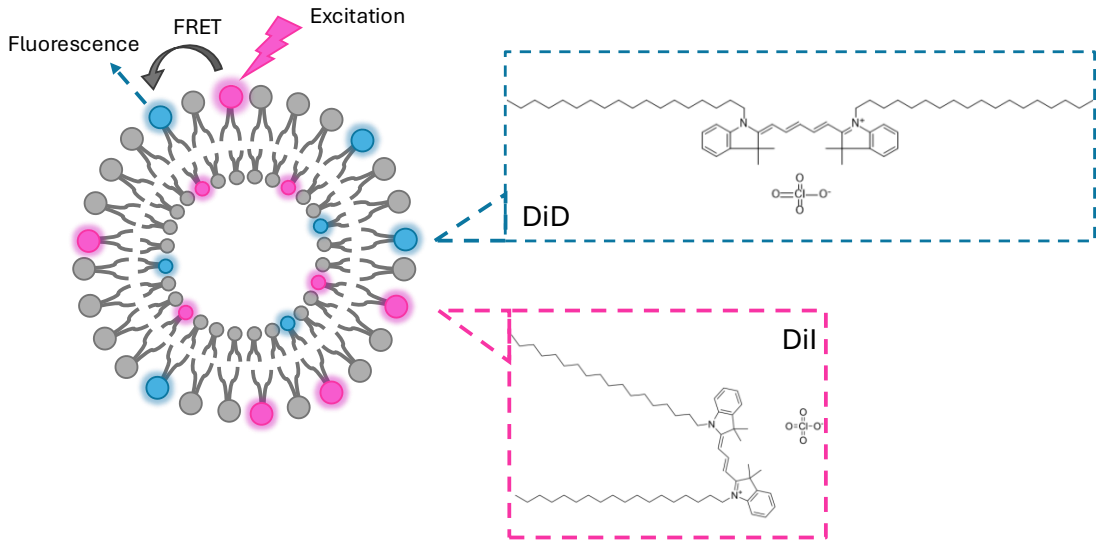

2.1.

FIGURE 2.2 Schematic of FRET vesicles. A diagram showing the synthesised FRET vesicles with chemical structures of DiI (pink) and DiD (blue) as insets and the transfer of energy between the donor and acceptor dyes shown.

2.2.1.3 Preparation of Giant Unilamellar Vesicles

The fluorescently labelled POPC lipid stock doped with 1 mol% DiI was prepared as previously described in section 2.2.1.1. This solution was then thinly spread onto a clean Teflon disc, cut into a 60 mm diameter circle, and subsequently evaporated using a gentle nitrogen stream to ensure chloroform removal. Following this, the Teflon disc was placed into a petri disc, covered with 5 mL 50 mM Tris Buffer (pH 8), sealed with parafilm and left for72 hours, where the longer the solution was left, the more concentrated the GUV

solution was. This protocol promotes lipid rehydration, allowing them to swell from the Teflon disc into the solution prior to investigation, as depicted in Figure 2.3 (*126*).

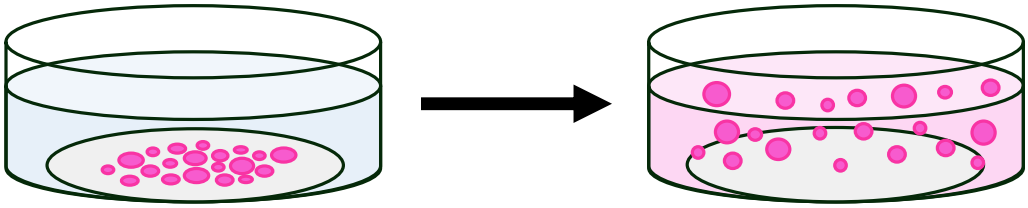

FIGURE 2.3 Schematic of GUV preparation method. A diagram showing the preparation of Giant Unilamellar Vesicles where evaporated lipids rehydrate in buffer and swell from the Teflon disc into the solution.

2.2.2 Dynamic Light Scattering

To investigate the size distribution of vesicles created by extrusion DLS was used. This technique analyses time-dependent fluctuations in scattered light by the sample to determine the hydrodynamic radius of the particles. When the particles are dispersed in solution, they move randomly due to Brownian motion and collide with other particles – transferring energy. Smaller particles move at higher speeds than larger particles due to these collisions and therefore by measuring the speed of the particles, the hydrodynamic radius can be determined. The correlation between the diffusion coefficient, D, and hydrodynamic radius R_H of the particles is given by the Stokes-Einstein equation (Equation 2.1).

$$\boldsymbol{D = \frac{k_B T}{6\pi\eta R_H}} \tag{2.1}$$

where k_B is the Boltzmann's constant, T is the solution temperature (21°C), and η is the viscosity of the medium (0.001 Pa s) (*127*).

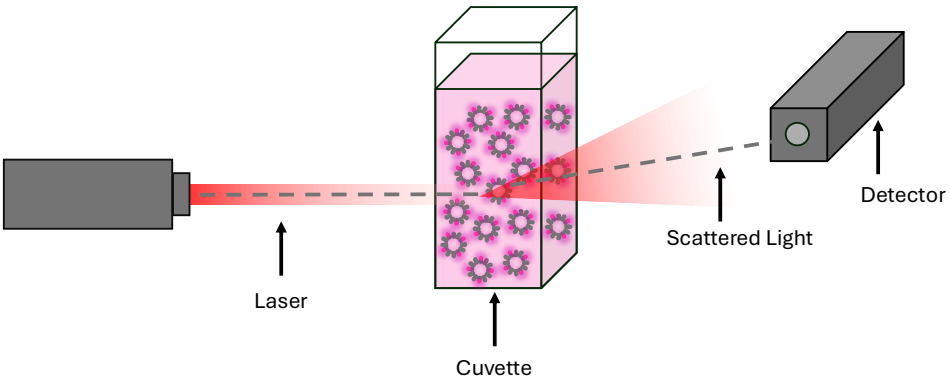

FIGURE 2.4 Schematic of Zetasizer mV DLS system.

In these investigations, a Zetasizer Mv DLS system (Malvern Instruments) was used to determine the size distribution of the vesicles. All DLS data were collected using 178° backward scattering and averaged over three experimental runs of 30 seconds, as seen in Figure 2.4. The backscattering system helps to avoid contributions from contaminants and large dust particles as these tend to scatter more light in the forward direction as their scattering becomes wavelength dependent. Samples were prepared in 50 mM Tris (pH 8) at a final lipid concentration of 67 µg/mL in a cuvette. This process was carried out for vesicles POPC and POPC/POPS mixtures extruded through 200 nm polycarbonate membrane filters and POPC vesicles extruded through 1 µm filters.

2.2.3 Fluorescence Spectroscopy

2.2.3.1 Time Correlated Single Photon Counting

To investigate the extent of membrane disruption by detergents and test the dequenching hypothesis, a picosecond time-resolved photoluminescence spectrometer was used. This instrument was used to measure the fluorescence lifetime of a solution containing DiI-labelled vesicles via time-correlated single photon counting (TCSPC). As discussed earlier, the fluorescence lifetime reflects the average time a fluorophore remains in an excited state. By monitoring the lifetime, changes in the morphology of fluorescently labelled vesicles were assessed in response to varying concentrations of detergents.

In these experiments, the PicoQuant FluoTime 300 spectrophotometer equipped with a hybrid photomultiplier tube (PMT) was used (Figure 2.5). Initially, a pulsed laser is passed through a neutral density filter and directed at the sample chamber which holds a cuvette containing fluorescently labelled vesicles in solution. This filter attenuates the incoming signal. The initial firing pulse acts a distinct 'start' reference and triggers the Time-to-Amplitude Converter (TAC) to begin generating a voltage ramp which linearly increases. The pulse also excites the sample, triggering the emission of a photon which is detected by a photomultiplier tube (PMT). The PMT consists of a light-sensitive photocathode which generates photoelectrons upon photon detections. These electrons are then directed towards a charged electrode called a dynode. The collision between the two produces additional electrons causing a multiplication effect. After further amplification by multiple dynodes, the electrons are collected at the anode of the PMT and output as a current which is directly proportional to the intensity of the initial photon. This signal is passed to the Constant Fraction Discriminator (CFD) which extracts precise timing information from the PMT and acts as a 'stop' signal (Figure 2.6A). The CFD also permits a discriminator level which determines a lower limit threshold that the incoming signal must surpass. This thereby suppresses random background noise. The stop signal is detected by the TAC which in turn stops generating additional voltage. The resulting voltage ramp is proportional to the time difference between the two signals as seen in Figure 2.6B. This information is then passed to an Analog to Digital Converter (ADC) which provides this timing to the histogrammer to output the information as the occurrence of emission over time after the excitation pulse, as shown in Figure 2.6C (*128*). For this experiment, an excitation wavelength of 532 nm and a repetition rate of 80 MHz was used to excite DiI, as this is the closest to the maximal absorption of the dye and the time-resolved fluorescence decays were collected at a wavelength of 567nm until a peak of 10^4 counts was received (*129*).

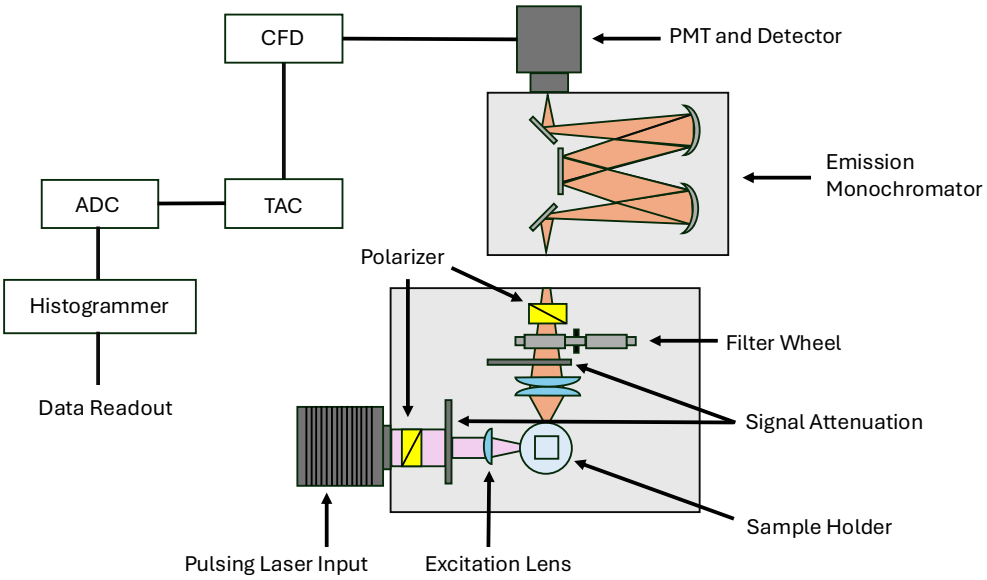

FIGURE 2.5 Schematic of the PicoQuant FluoTime 300 fluorescence spectroscopy instrument. CFD = Constant Fraction Discriminator. TAC = Time-to-Amplitude Converter. ADC = Analog-to-Digital Converter.

An important aspect of TCSPC is the need to maintain a low probability of registering more than one photon per cycle. This is because the detector and electronics have a 'dead' time in which they cannot process another event. This is typically a few nanoseconds long. If the number of photons occurring in one cycle was greater than 1, the system would fail to register any photons after the first has been detected. This results in a misrepresentation of the data and skews towards artificial lower lifetimes. This effect is known as pulse pile-up, as seen in Figure 2.6D. On average only one in 20 to 100 excitation pulses should generate a count at the detector. This was achieved by keeping the working vesicle (and fluorophore) concentration low and attenuating the incoming excitation pulse.

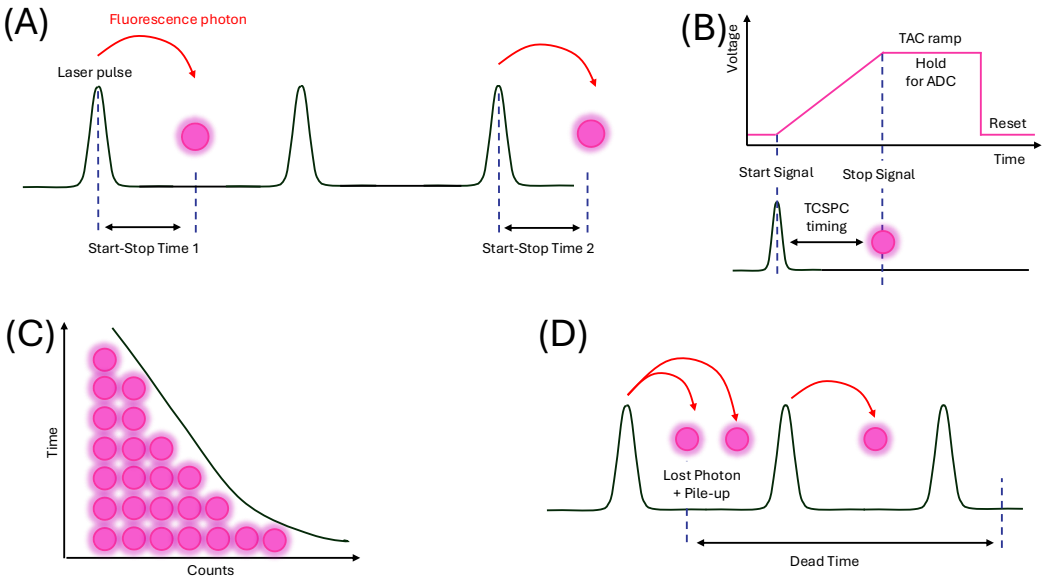

FIGURE 2.6 Schematic showing the start-stop mechanisms of TCSPC. (A) The fluorescence lifetime between an excitation pulse triggering a start signal and a fluorescent photon triggering a stop signal. (B) The voltage ramp process that the TAC performs during TCSPC. (C) The histogram produced from hundreds of start-stop events. Solid black line represents an exponential decay from which the lifetime is extracted. (D) The issue of pulse pile-up caused by the emission of more than one fluorescent photon.

TCSPC is limited by the instrument response function (IRF). The IRF determines the temporal resolution of the fluorescence lifetime measurements and summarises the systems overall timing precision (*130*). In an ideal system the IRF would be infinitely narrow however multiple factors increase the broadening of this factor. This includes the timing resolution in the detector, the width of the excitation source and the jitter in the electronics. An estimate of the overall IRF width can be obtained from the geometric sum of these individual components. The IRF also complicates the analysis of fluorescent lifetime as it is convoluted with the fluorescence lifetime and therefore adds additional variation between measurements. To overcome this, the IRF can be deconvoluted by measuring the fluorescent decays and emission of a non-emissive scatter. For these experiments, Ludox (SiO_2) suspended in 50 mM Tris was used which scatters light without being fluorescent (*131*). An IRF was collected after each lifetime measurement of the

sample of interest. Furthermore, the system was calibrated using Rhodamine 6G suspended in ethanol which is well studied in the literature, and has a lifetime of 4.1 ns (*132*). Time resolved fluorescence decays after reconvolution with the instrument response function were fitted to single- and bi-exponential decays using FluoFit (PicoQuant) fitting software. The titration data was also fitted with a Hill function due to the cooperative behaviour of detergent molecule binding (*133*), seen in Equation 2.2.

$$\boldsymbol{t_{average} = A + B\ \frac{[detergent]^n}{k^n + [detergent]^n}} \tag{2.2}$$

Where A is the initial lifetime, B is the scaling factor, k is the half-maximal concentration constant, and n is the Hill coefficient.

From the acquired decay histogram, the amplitude weighted average fluorescent lifetime ($\tau_{average}$) was calculated using Equation 2.3.

$$\boldsymbol{\tau_{average} = \frac{\sum A_i \tau_i}{A_i}} \tag{2.3}$$

Where A_i is a pre-exponential factor, and τ_i is the individual fluorescent lifetimes. In addition to the amplitude weighted average lifetime, both the contributions of the slow and fast component was measured. The percentage difference between the two was calculated with Equation 2.4,

$$\%\boldsymbol{\tau_{fast} = \frac{\tau_{fast} * A_1}{(\tau_{fast*} A_1) + (\tau_{slow} * A_2)}} \qquad \%\boldsymbol{\tau_{slow} = \frac{\tau_{slow} * A_2}{(\tau_{fast*} A_1) + (\tau_{slow} * A_2)}} \tag{2.4}$$

Where A is the pre-exponential factor of the component with the corresponding lifetime τ. Finally, time-dependent average lifetimes were acquired every minute for 30 minutes following injection of a known concentration of detergent. This data was fitted to an exponential increase with Equation 2.5,

$$\boldsymbol{\tau_{average} = A_1 e^{\frac{x}{\tau_1}}} \tag{2.5}$$

Where A is the pre-exponential factor and τ is the individual fluorescent lifetimes.

2.2.3.2 Widefield Optical Microscopy

Fluorescence images were obtained using an upright Olympus BX43 microscope equipped with a collimated LED and Cy3 filter cube for fluorescence excitation of DiI and 2048 x 2048 complementary metal oxide semiconductor camera (Thorlabs). This instrument acquired fluorescence images of DiI-labelled vesicles, using an excitation wavelength of 532 nm. The light source was passed through a Cy3 excitation filter and 100x objective lens (NA = 1.4, UPLSAPO, Olympus) which focusses the light onto the sample to excite the fluorophores from the specimen. The resulting emitted fluorescence was passed through a Cy3 emission filter which permits the passage of only the fluorescence signal onto the detector (*134*). The resulting field of view was calibrated using a NBS 1952 Resolution Test Target, 3" x 1" and estimated to be 103.5 μm^2. The samples were visualised using a flow-cell microscope slide (*135*) which were prepared by attaching two lengths of double-sided Scotch tape at either edge of a 25 x 25 mm #1 glass coverslip (VWR) onto a 25 mm x 75 mm microscope slide – creating a thin tunnel between the two that draws liquid through via capillary flow (Figure 2.7). 100 µL of 1 % poly-L-lysine was flushed through the tunnel using a KimWipe at the opposite end of the coverslip to the pipette to draw the liquid through after initially filling of the channel and left to incubate for 5 minutes at room temperature. Unbound molecules were then removed by flushing the channel with 50 mM Tris (pH 8). After this, 100 µL of the working vesicle sample was flushed through the tunnel and left to incubate for a further 5 minutes to non-specifically immobilise the vesicles. Finally, any unbound vesicles were removed via another buffer wash. When using the tunnel slide on the microscope, immersion oil with a refractive index of 1.518 was applied onto the oil-immersion objective lens and placed into the slider holder on the microscope body.

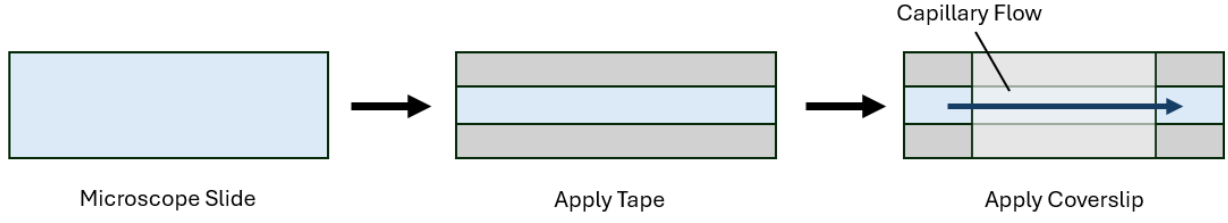

FIGURE 2.7 Schematic of a tunnel slide using in Widefield Microscopy. This is prepared from double-sided scotch tape, a glass microscope slide and coverslip. The liquid is pulled through the thin central tunnel created by capillary action.

2.2.3.3 Spectrophotometer

Fluorescence spectra were acquired using a HORIBA Fluoromax-4 fluorescence spectrophotometer. In this system, a continuous light source was emitted from a 150 W xenon Illuminator onto an excitation monochromator. This selects bands of wavelengths which are directed onto the sample held in a cuvette. The resulting light that passes through the sample was directed onto a second emission monochromator which then shines onto the detector. The entrance and exit ports of the monochromator have continuously adjustable slits. The width of the slits on the excitation monochromator determines the bandpass of light incident on the sample and the width of the emission monochromator slits controls the intensity of fluorescence signal recorded by the signal detector. The narrower the slits, the higher the resolution but at the expense of signal. For these experiments, a 2.5 mm slit width was chosen. The signal detector monitors light emitted from the sample and exiting the emission monochromator, while the reference detector monitors light exiting the excitation monochromator. The signal at the reference detector can be used to compensate for source intensity fluctuations as a function of wavelength or time (*136*). Measurements were acquired by monitoring the ratio of intensity from the signal detector (S) to the intensity of the reference detector (R). An excitation wavelength of 520 nm was used, and the resulting emission was recorded over a range of 535 - 800 nm using an integration time of 1 nm per second.

2.2.3.4 Förster Resonance Energy Transfer

During FRET, the extent of non-radiative energy transfer between two fluorescent dyes in close proximity (~1 - 10 nm) can be used to estimate the distance between them. When incident with an excitation photon, the donor fluorophore excites and transfers its energy to an acceptor fluorophore non-radiatively. The efficiency of this energy transfer (E) can then be used to report on the distance between the two dyes via (Equation 2.6),

$$E = \frac{1}{1 + (\frac{R}{R_0})} \tag{2.6}$$

where R is the inter-dye distance and R_0 is the Förster radius at which E = 0.5. Using this equation, a decrease in the efficiency of energy transfer per vesicle quantitatively reports on an increase in separation between fluorophores which can be attributed to vesicle expansion and/or solubilisation. In addition to the separation between dyes, the rate of transfer is also dependent on the dyes quantum yield, relative orientation, and the refractive index of the solution (*137*, *138*). These parameters are accounted for in the Förster radius, which can be calculated using Equation 2.7,

$$R_0 = 0.211^6\sqrt{k^2 n^{-4} \Phi_D J(\lambda)} \tag{2.7}$$

where k^2 is the orientation factor, typically assumed to be ~2/3 when the donor and acceptor orientations of freely rotating, n is the refractive index, Φ_D is the quantum yield of the donor and J(λ) is the overlap integral (Figure 2.9A). For the FRET pair used in these experiments, DiI and DiD, R_0 = 3.9nm (*139*).

Fluorescence intensities from FRET vesicles were acquired using the HORIBA Fluoromax-4 fluorescence spectrophotometer. The resulting background-corrected spectra was measured in the range of 535 – 800 nm, and the apparent efficiency of the non-radiative energy transfer from the donor to acceptor fluorophore was calculated using Equation 2.8.

$$E_{FRET} = \frac{I_A}{I_A + I_D} \tag{2.8}$$

Where I_D is the intensity of the donor fluorophore (DiI), measured at 565 nm, and I_A is the intensity of the acceptor fluorophore (DiD), measured at 665 nm (Figure 2.9B). Variations in the FRET efficiency was fitted to a Hill model, as previously described.

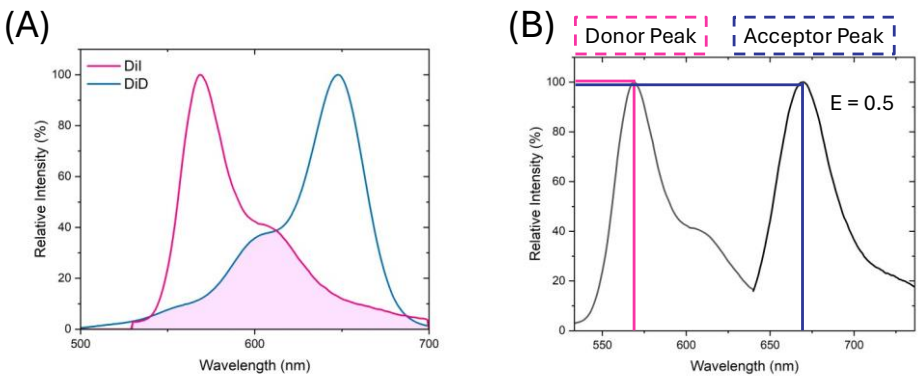

FIGURE 2.8 Example FRET graphs. (A) Overlapping absorption (pink) and emission (blue) spectra from DiI-DiD FRET pair with the spectral overlap highlighted in purple. (B) Emission spectra from DiI-DiD labelled vesicles, where the FRET efficiency is given by Equation 2.8, where I_A is the peak acceptor intensity and I_D is the peak donor intensity.

2.2.3.5 Micro Photoluminescence

Micro Photoluminescence (Micro-PL) allows for measurement of fluorescence emission spectra from single nanoscale objects. The configuration of the Micro-PL set-up used in this work is schematically illustrated in Figure 2.10. A continuous 532 nm laser is passed through a dichroic beam splitter and focused onto the sample by a 50x objective lens with a 2-micron spot density. This directly excites the sample and leads to the emission of photons by the fluorophores. These photons are collected by a spectrometer with a charge-coupled device and the resulting fluorescence emission spectra per field of view is measured (*140*). The laser power throughout the experiment was kept at 1 mW, as to minimise the effect of photobleaching.

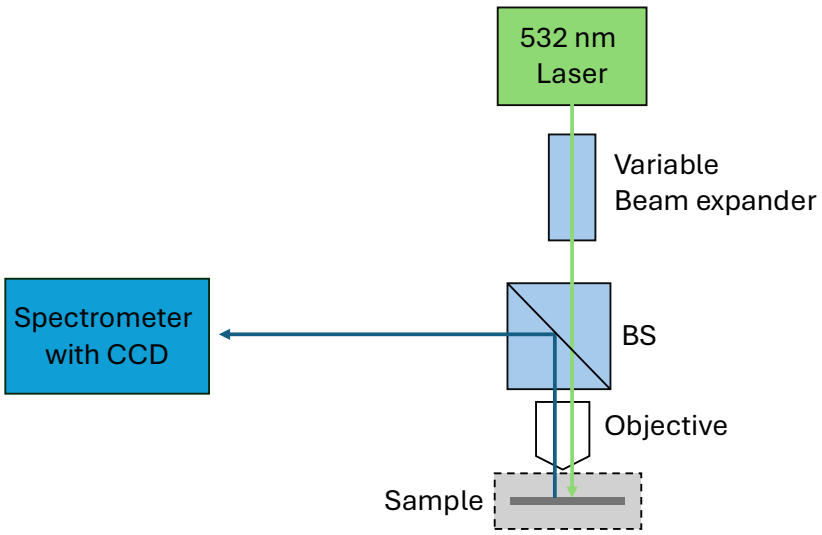

FIGURE 2.9 Schematic of the Micro-PL set-up. BS = Beamsplitter. CCD = Charge-Coupled Device

2.2.3.6 Single Vesicle Fluorescence Lifetime Imaging

Single Vesicle Fluorescence Lifetime Imaging (svFLIM) was performed using a Luminosa single photon counting confocal microscope (PicoQuant) as schematically depicted in Figure 2.11 (*141*). In preparation for svFLIM, vesicles were immobilised onto a high precision microscope slide (ThorLabs). During immobilisation, 1% poly-L-lysine was added to the microscope slide and left to incubate for 5 mins, before the excess was washed away with 50 mM Tris buffer (pH 8). After this 50 µL droplets of 200 nm POPC vesicles labelled with 1% DiI suspended in buffer and left to incubate for a further 5 minutes. Any unbound vesicles were then washed away with Tris buffer before analysis. The Luminosa was equipped with a 60x 1.20 numerical aperture water objective lens, FLIMbee Piezo scanner and single photon avalanche diode (SPAD) detection. Excitation was provided by a 532 nm laser output, operating with a 0.5 mW output power and 20 mHz repetition rate. Luminosa was able to showcase the average lifetime per pixel as well as create an image based on these acquisitions. Fluorescence decays were fitted to a bi-exponential decay, using the Luminosa software package (PicoQuant).

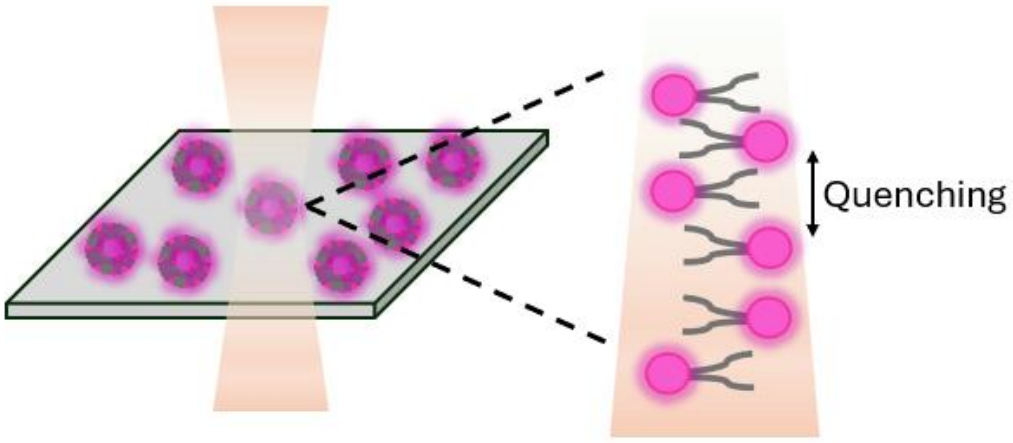

FIGURE 2.10 Schematic of the FLIM approach. Individual vesicles incorporating DiI are immobilised and spatially isolated on a surface, where they are excited by pulsed excitation in a confocal geometry.

2.2.4 Scanning Electron Microscopy

Scanning Electron Microscopy (SEM) was used to visualise and quantify changes in vesicle morphology, before and after the addition of the detergent TX-100. SEM uses kinetic energy to produce signals on the interactions of electrons (Figure 2.12). During this, electrons are emitted from an electron gun and focussed into a beam onto the sample. The electron beam is optimised throughout the instrument by a series of lenses and apertures which remove high angle electrons and further focus the beam to produce higher quality images. The interaction between the electrons and the surface, results in deceleration of the incident electrons and dissipates as a variety of signals. This consists of secondary electrons, backscattered electrons, diffracted backscattered electrons, photons and visible light. The electron signals are collected on a cathode ray tube to generate the image, where typically the secondary electrons are used for displaying sample morphology and topography and backscattered electrons are used for displaying composition contrasts (*142*, *143*).

Before SEM was carried out, a silicon substrate was ultrasonically cleaned to remove any organic contaminants. Here, the substrate was submerged in acetone, as to remove polar residues, and placed in an ultrasonic bath cleaner for 3 minutes. The substrate was

then further cleaned with isopropanol which also washes away acetone from the substrate. Once the substrate was sufficiently cleaned, it was placed in an oxygen plasma asher for a further 3 minutes. The plasma asher uses neutral oxygen radicals to remove the photoresist later of the substrates, which increases the conductivity of the substrate. The vesicle sample was then deposited onto the substrate and subsequently evaporated. The evaporation of the sample is an essential step in SEM, as the microscope operates in a high-pressure vacuum and therefore any water present would immediately evaporate and damage the sample. For these experiments, two alternative methods for the evaporation of the sample were employed: the substrate was placed on a hot plate at 38.6° for 5 minutes, or the water was removed using tissue blotting. After the sample had been evaporated, the substrate was placed in a JEOL JFC-2300HR splutterer, which deposits an 8 nm copper layer over the sample to increase its conductivity and minimise charging effects. SEM images were acquired using a JEOL JSM 7800-F system operating at 5 kV and 48 µA.

To compare the changes in vesicle morphology, the diameter, area and circularity of the vesicles before and after the addition of 0.3 mM TX-100 was analysed using ImageJ. Vesicle circularity was measured via the following equation:

$$\boldsymbol{c = 4\pi\left(\frac{A}{p^2}\right)} \tag{2.9}$$

Where A is the observed area and p is the perimeter. A circularity value of 1 indicates a perfectly circular object whereas a value of 0 indicates elongated polygon.

2.2.5 Preparation of Amyloid-beta 1-42

2.2.5.1 Monomeric Amyloid

0.5 mg lyophilized $A\beta_{1\text{-}42}$ (Cambridge Biosciences) was dissolved in 100% 1,1,1,3,3,3-hexafluoro-2 propanol (HFIP) to make 11 aliquots of 0.045 mg in Protein LoBind Eppendorf Tubes. HFIP was subsequently evaporated by desiccation under vacuum for 5 hours and the dry peptides are stored at -20 °C. Working amyloid was resuspended in 10 µL DMSO to create a final $A\beta_{1\text{-}42}$ concentration of ~2 µM.

2.2.5.2 Amyloid Aggregates

Working amyloid was suspended in 500 µL SSPE buffer (pH 7.4) and incubated at 37 °C, as to promote its aggregation to create a 19.6µM solution. After 15 minutes, 30 minutes, and 24 hours, 100 µL of the incubated sample was removed from the incubator and added to the vesicle sample.

3. Development of a Fluorescence De-Quenching Assay to Monitor Detergent-Induced Membrane Damage

In this Chapter the use of fluorescence de-quenching as a tool for monitoring changes to membranes is explored using the non-ionic detergents TX-100 and Tween 20, and ionic detergent SDS on ensemble model LUVs. The adaptability of the technique will be showcased by exploring changes in lifetime when varying different components of the assay such as dye concentration, vesicle size and lipid composition. Finally, confirmation of the sensitivity of the technique will then be assessed by comparison to ensemble FRET measurements – a highly popular, but limited, technique for measuring changes in vesicle size. Overall, this Chapter introduces a new fluorescence-based assay based on intramembrane de-quenching between membrane-bound dyes as a technique for monitoring conformational changes in model membrane vesicles.

3.1 Results and Discussion

3.1.1 Fluorescence De-quenching of 1% DiI labelled model membrane vesicles using detergents

3.1.1.1 De-quenching assay for membrane disruption by detergents

200 nm LUVs composed of 99% POPC and 1 mol% DiI were prepared as detailed in section 2.2.1.1, suspended in 50 mM Tris buffer (pH 8) and held in a cuvette at a final concentration of 67 μg/mL. Fluorescent lifetime measurements were obtained without the presence of detergents and the decays fitted well to a bi-exponential decay after reconvolution with the instrument response function (Figure 3.1A). The size of the extruded vesicles were also confirmed using DLS and the average diameter was given to be 190.1 ± 1.58 nm, providing confidence that the working vesicles were of desired size (Figure 3.1B). To ensure that any changes in lifetime observed were due to the addition of detergent, and not due to time-dependent variations in the fluorophore photophysics, the average lifetime of DiI was monitored over the course of 30 minutes, with

measurements acquired every 1 minute. This data showed no significant change from the initial value of 0.66 ns (Figure 3.1C).

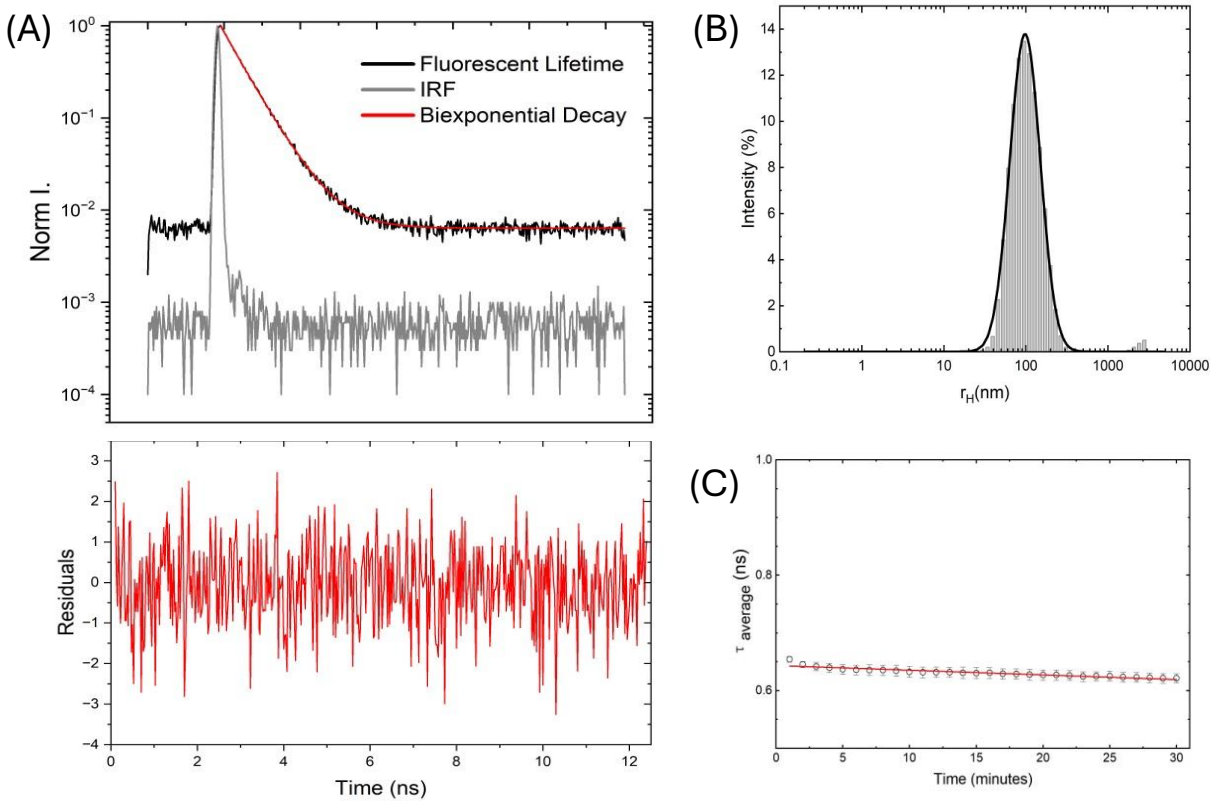

FIGURE 3.1 Fluorescence lifetime of 200 nm 1% DiI POPC vesicles. (A) Fluorescence lifetime data (black) fitted with a biexponential decay function (red) and its IRF (grey). The associated residuals can be seen below. (B) Hydrodynamic radius (r_H) distribution of 200 nm POPC vesicles obtained via DLS (μ = 257.5 ± 1.4, σ = 114.9 ± 1.6). Solid line represents lognormal fit (R^2 = 0.99). (C) Average lifetime of 200 nm POPC vesicles with 1% DiI as a function of time. Data shown represents the mean values obtained from three experimental runs and error bars denote the standard error of the mean.

TX-100 was progressively added to the vesicles in steps of 0.02 mM and the amplitude weighted average fluorescent lifetime was measured with an excitation wavelength of 532 nm by Time Correlated Single Photon Counting (TCSPC), as detailed in the methodology (Figure 3.2A). Similar experiments were also performed using SDS and Tween-20 in steps of 0.2 mM and 0.02 mM, respectively. For TX-100, increasing the concentration up to the CMC (~0.3 mM) increased the amplitude weighted average

lifetime by a factor of 2. The value increased from an initially quenched lifetime of 0.58 ± 0.004 ns to 1.2 ± 0.03 ns, with an obtained half-maximal concentration of 0.18 mM – following a Hill model fit (Figure 3.2B). At sub-solubilising concentrations below the CMC the lifetime progressively increased and increasing concentrations beyond the CMC resulted in a plateau. This increase and subsequent plateau in average lifetime component can also be seen with Tween20 (CMC ~0.06 mM) and SDS (CMC ~8.3 mM) where the observed plateau occurs at and 0.90 ± 0.01 ns for Tween-20 (Figure 3.2C) and 0.76 ± 0.01 ns for SDS (Figure 3.2D). This difference in end point lifetimes could reflect differences in final micelle morphologies. In all cases, the addition of the detergents caused the average lifetime component to increase from a similar initially quenched starting value of ~0.6 ns for sub-solubilising concentrations, indicating that fluorescence de-quenching is sensitive to detergent-induced membrane damage. While the precise nature of the bi-exponential components requires further evaluation, this could be indicative of DiI adopting two conformational states or experiencing two different membrane environments such as the outer or inner leaflet.

To further support a de-quenching process, the ensemble fluorescence emission spectra of DiI were also measured in the range of 535 – 700 nm using the Fluoromax 4 spectrophotometer. TX-100 was progressively added as previously described and the spectra was corrected for background. The data showed that the integral mean intensity of the dye increased by ~20% when the detergent was added, from an initial value of 2.7 $x10^6 \pm 2.2\ x10^5$ to $3.3\ x10^6 \pm 10^5$ a.u. under the conditions tested (Figure 3.2E). This further supports the use of fluorescence de-quenching for probing detergent-induced membrane solubilisation.

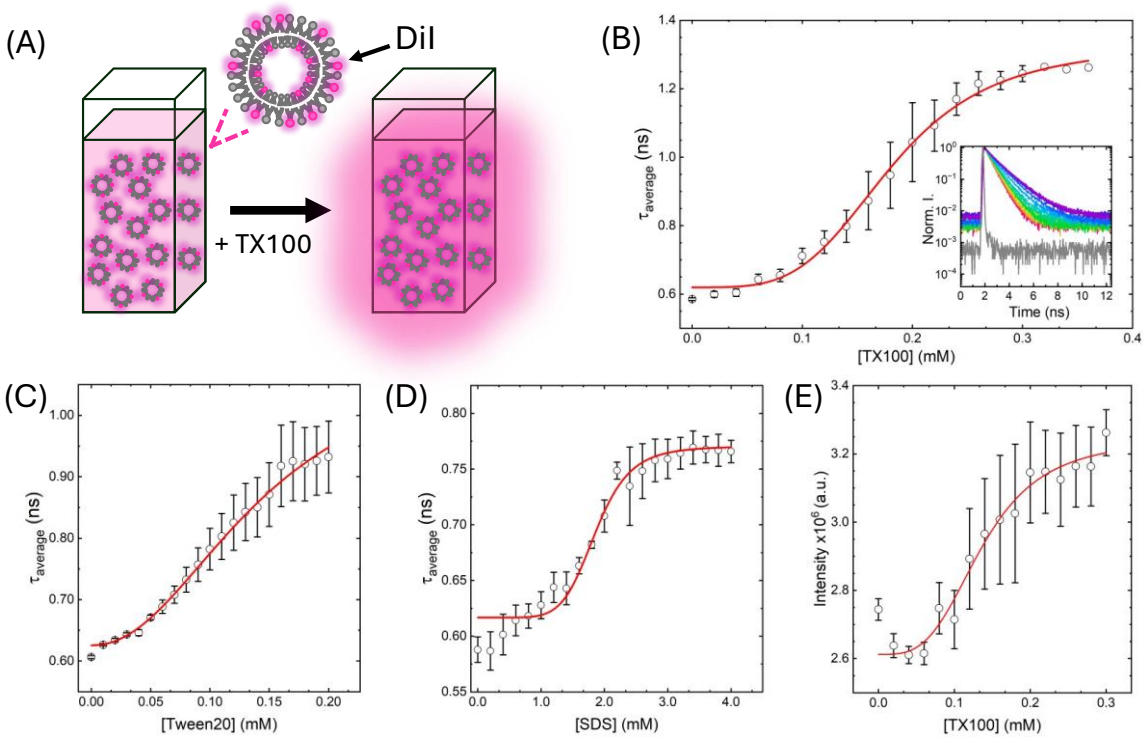

FIGURE 3.2 Increasing concentrations of detergents increases fluorescence lifetime and intensity. (A) Schematic illustration of the assay. Injection of TX-100 into solution containing DiI-labelled POPC vesicles induces vesicle solubilization, triggering an increase in the relative DiI-DiI distance and fluorescence de-quenching. (B) Average amplitude weighted lifetime of 200 nm POPC vesicles with 1% DiI as a function of TX-100 concentration. Solid red line represents a Hill model fit (R^2 = 0.99). Inset: corresponding time-resolved fluorescence decays and IRF (grey). Average lifetimes of 200 nm POPC vesicles with 1% DiI as a function of (C) Tween20 and (D) SDS concentration. Solid red lines represent Hill model fits (R^2 = 0.86 and 0.96, respectively. (E) Integral fluorescence intensity of 200 nm POPC vesicles as a function of TX-100 concentration. Solid red line represents a Hill model fit (R^2 = 0.94). In all cases, data shown represents the mean values obtained from three experimental runs and error bars denote the standard error of the mean.

The results from the experiments suggest that the fluorescence de-quenching technique can be used to monitor morphological changes to vesicles induced by detergents. Of particular note, the fluorescence enhancements were observed in all cases at concentrations below the detergent CMC, suggesting that the assay is sensitive to structural changes such as swelling within intact vesicles. As discussed earlier, this

change in fluorophore lifetime and intensity is likely reflected by a decrease in self-quenching due to an increase in separation between fluorophores as the vesicles solubilise. The increase in distance between identical dyes in the vesicle essentially results in fewer interactions between excited molecules that would reduce their duration in the excited state, such as collisions and energy transfers (*74*). This behaviour is consistent with previous research which highlighted kinetic details of vesicle solubilisation using single vesicle FRET and fluorescence correlation spectroscopy, and which suggest that vesicles undergo morphological changes prior to complete solubilisation (*59*, *144*). In this work, addition of TX-100 triggered vesicles to undergo a ~5% increase in surface area prior to solubilisation. Following Hill fits, the half-maximal concentration constant, k, for all detergents occurs around the range of the CMC which provides confidence that the changes observed are due to solubilisation of the vesicle. It is also worth noting that the magnitude of error bars generally increases around the CMC. This may be reflective of a greater variety of morphologies around this concentration, as it is expected that there would be populations of both intact and partially solubilised vesicles, as well as mixed detergent-lipid micelles (*145*). If the DiI lifetime is sensitive to local environment as suggested, then this would result in a larger spread of lifetimes by the fluorophores – resulting in the observed larger error bars. Furthermore, at concentrations exceeding the CMC, the lifetime plateau which is consistent with the formation of mixed detergent-lipid micelles in stage 3 of the 3-state model (*24*). At this point, the separation between fluorophores is not expected to increase any further as the morphology of the micelles remain relatively stable. An important aspect to note is that although for all detergents the trend in lifetime follows a Hill fit, both the required concentrations and maximum obtained lifetime varies. As seen in Figure 3.2B, the end-point lifetime of TX-100 is higher than both Tween20 and SDS (Figure 3.2C and D), and Tween20 requires lower concentrations to completely solubilise the vesicle. This may, in part, be due to TX-100 and Tween-20 being fast-solubilising detergents - meaning that that they are able to incorporate into and flip the bilayer of the vesicles at a faster rate compared to SDS (*38*). Detergents with a fast solubilisation mechanism are also more likely to break down the membrane by the formation of micelles, whereas slow solubilising detergents are more likely to destabilise the membrane by inducing high curvature stress. For example, TX-100 has higher tendencies to form mixed detergent-

membrane micelles whereas SDS is more likely to create small membrane invaginations to induce solubilisation. This difference in solubilisation mechanisms can be reflected in the amplitude of change in lifetime. For example, the average lifetime for SDS increases by ~30% compared to TX-100 which increases by ~120%. Furthermore, this may result in differing end stage morphologies between the detergents which could explain the difference in the maximum average lifetime component. Taking all this into consideration, further experiments investigating detergent-membrane interactions used TX-100 as the detergent of choice due to the assay's high sensitivity. Where this assay primarily focuses on the change in vesicle morphology during the transition of intact vesicles to the formation of micelles, further information reporting on the initial dynamics of the interactions, for example via molecular dynamics simulations, between the detergent molecules and the membrane would provide greater insight, especially during the initial stages. Despite this, the data shown in Figure 3.2 supports a broad model of detergent-induced solubilisation that involves morphological changes and potential structural remodelling of intact vesicles at concentrations below the CMC prior to lysis.

3.1.1.2 Fast and Slow Lifetime Contributions

To investigate the precise nature of the biexponential decay exhibited by the vesicle-bound DiI, the fast and slow lifetime components obtained from the above titration were also recorded. The results from this suggested that the slow component has greater contributions to the average lifetime component as it increases in a similar trend with the addition of detergent. As seen in Figure 3.3A, the fast component increased by ~51.2% from an initial value of 0.42 ± 0.08 ns to 0.62 ± 0.05 ns with the addition of 0.3 mM TX-100. In comparison, the slow component approximately doubled in magnitude from 0.68 ± 0.04 ns without detergent to 1.37 ± 0.03 ns (Figure 3.3B). The percentage difference between the two components was calculated as detailed in the methodology (Eq 2.4). Whilst both components increase with the addition of TX-100, the results suggests that the slow component has greater contributions to the average lifetime component as it increases in a similar trend. Despite this, when looking at the individual percentage contributions (Figure 3.3C and D), it appears that these remained largely invariant across the titration with both lifetime components accounting for ~50 %. The bi-exponential decay seen under all TX-100 conditions could be occurring because of multiple different factors. The primary cause of this is hypothesised to be due to DiI adopting two local

environments in the vesicle. However, this behaviour could also be due to cooperative atomic binding of the fluorophores during the relaxation process (*146*). Both of these would lead to the presence of multiple fluorophore populations, giving rise to a variety of decays towards the ground state. Further investigations into these components would help provide a more detailed understanding of any subtle changes in the local environment as the experiment progresses. Nevertheless, it is clear from this analysis that the slow lifetime component is the main contributor towards the variations in amplitude weighted average lifetime as shown in the previous experiment.

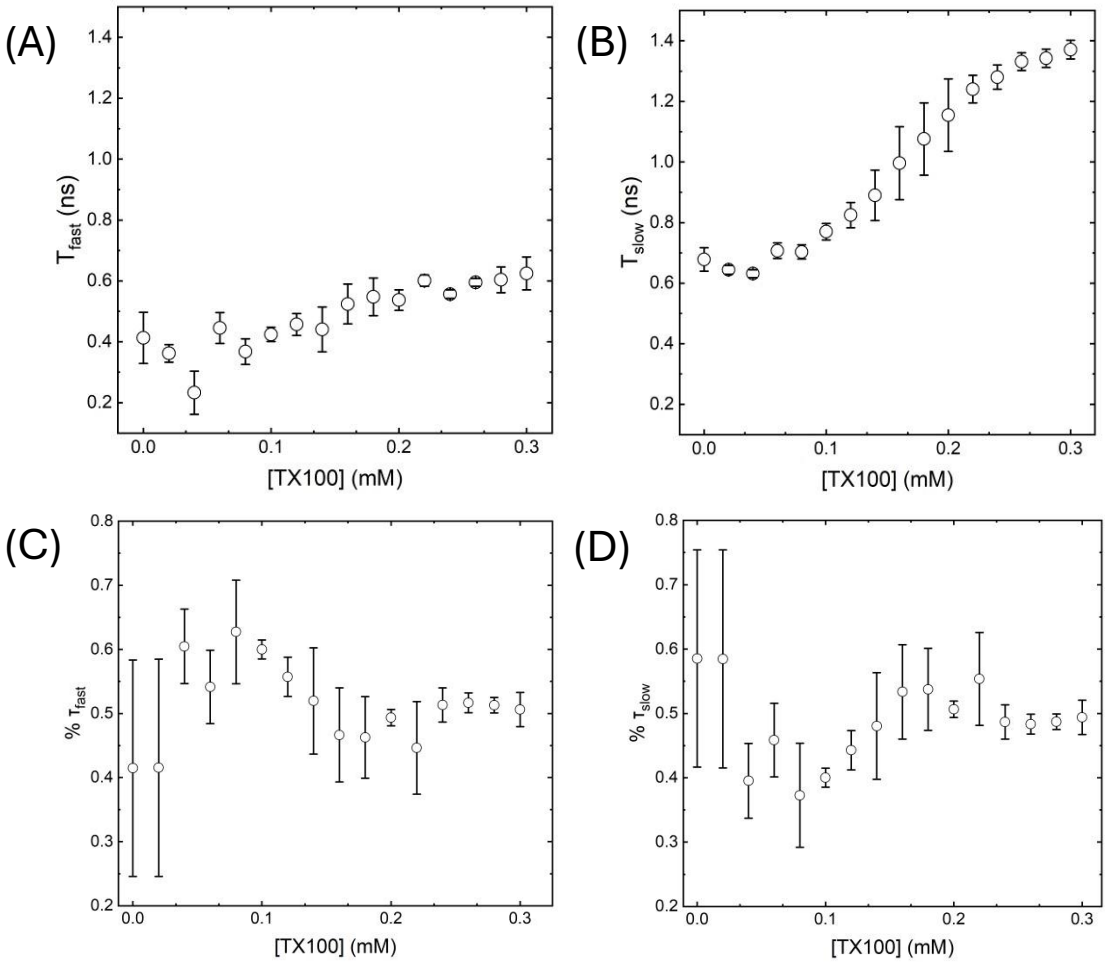

FIGURE 3.3 Contributions of the fast and slow lifetime components to the amplitude weighted average lifetime component. (A) Fast lifetime of 200 nm POPC vesicles with 1% DiI as a function of TX-100 concentration. (B) Slow lifetime of 200 nm POPC vesicles with 1% DiI as a function of TX-100 concentration. Representative variation in % contributions of the (C) fast and (D) slow lifetime components obtained from 200 nm POPC vesicles with 1% DiI as a function of TX-100 concentration. Data

shown represents the mean values obtained from three experimental runs and error bars denote the standard error of the mean.

3.1.1.3 Fluorescence de-quenching at different emission wavelengths

The typical DiI spectra, as seen in Figure 3.4A, shows a peak intensity of fluorescence at 565 nm and a second shoulder peak at 607 nm. The presence of the second shoulder implies that the fluorophore adopts two primary different states during excitation. For example DiI dimers can absorb and emit at red-shifted wavelengths compared to the monomer, and DiI can exist in both a cis and trans isomer form; processes that favour the trans conformation can enhance the fluorescence intensity and contribute to the shoulder (*147*). Monitoring the resulting lifetime when the fluorophore is excited at this shoulder peak wavelength would provide insight into whether fluorescence de-quenching is conformation specific or if it occurs for all conformations of the dye. As seen in Figure 3.4B, the increase in lifetime obtained for both emission wavelengths follow a similar trend, with both starting at the quenched 0.6 ns, and plateauing at ~1.26 ns upon TX-100 addition. The notable difference between the two wavelengths is that emission at 607 nm reports a subtly higher half-maximal concentration of 0.23 ± 0.006 mM compared to 0.18 ± 0.004 mM, as seen in Figure 3.4C. Since the intensity at the wavelength is significantly lower than the intensity at the peak (565 nm), it can be assumed that less molecules are present in this population. This means that higher concentrations would be required to increase the separation between individual molecules, resulting in the observed difference in half-maximal values. Nevertheless, the results from this investigation suggests that the de-quenching behaviour can be observed for all molecule conformations, and importantly the de-quenching signal occurs at concentrations below the CMC.

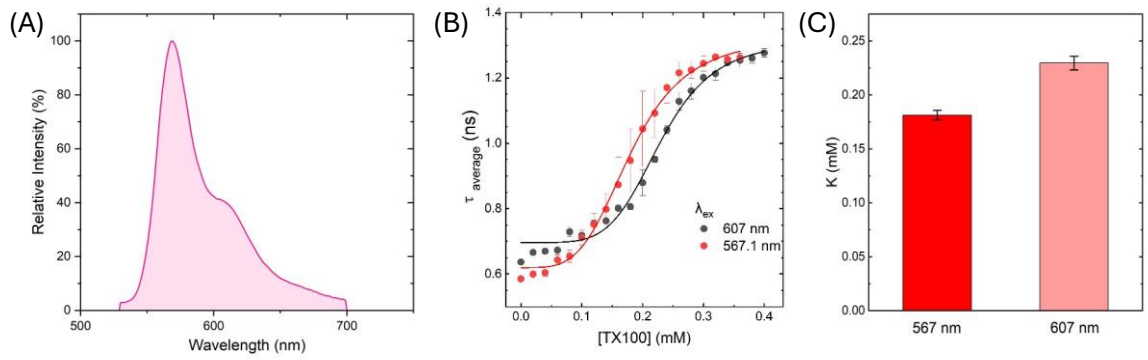

FIGURE 3.4 Comparison between different excitation wavelengths. (A) Example excitation Spectra from fluorophore DiI showing emission peaks at 567 nm and 607 nm. (B) Average lifetime component from 200 nm POPC vesicles with 1% DiI as a function of TX-100 concentration, with resulting lifetime recorded with an excitation wavelength of 567 nm (red) and 607 nm (black). Data shown represents the mean values obtained from three experimental runs and error bars denote the standard error of the mean. Solid lines represent hill model fits (R^2 = 0.99 for both). (C) Comparison between obtained half-maximal concentration constant, k, as a function of excitation wavelength. Error bars are obtained from the error within the fitting.

3.1.1.4 Kinetics of Detergent-Induced Vesicle Solubilisation Monitored by Fluorescence De-Quenching

Following these experiments, the real-time kinetics of solubilisation were obtained from 200 nm, 1% DiI-labelled POPC vesicles, by measuring the lifetimes every 30 minutes following injection of various concentrations of the detergents. For Tween20 and SDS, the results followed a general trend in which increasing the concentration of detergent increased the rate of change in average lifetime. Under the Tween20 conditions tested, the rate of change was found to be 0.003 ns/min for 0.2mM and 0.006 ns/min for 1 mM. The greatest change occurred when 2 mM Tween20 was added, which increased the lifetime at a rate of 0.25 ns/min until the value eventually plateaued at 0.81 ns after approximately 8 minutes (Figure 3.5A). At 0.5 - 10 mM SDS, the rate of change was found to be in the range of 0.01 - 0.03 ns/min before the lifetime similarly plateaued (Figure 3.5B). For TX-100, the induced solubilisation rates could not be quantified as the vesicles solubilised on a timescale faster than the time interval the FluoTime 300 requires to

accurately capture spectral changes (Figure 3.5C). Despite this, multiple problems arose within the data collection that would require further investigations.

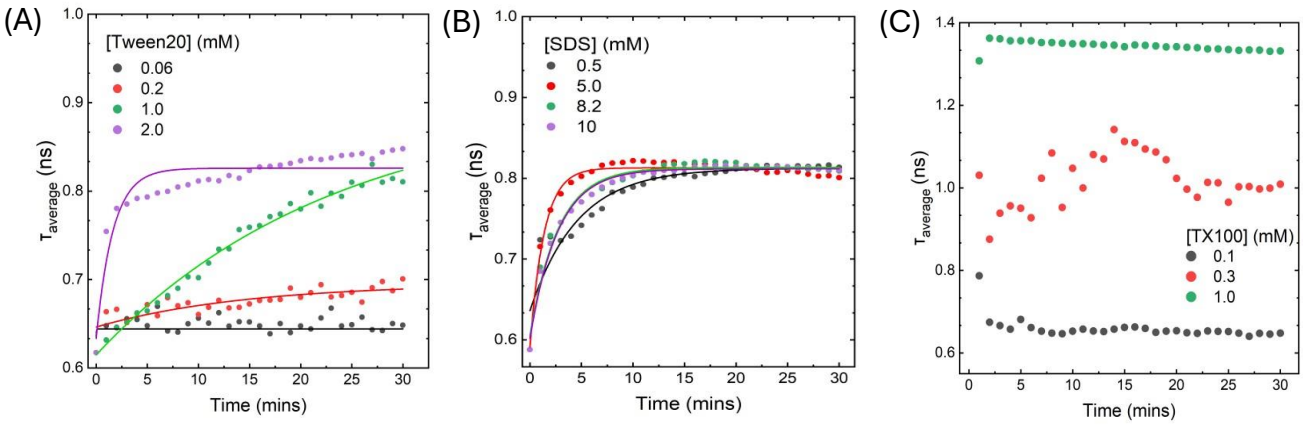

FIGURE 3.5. Kinetics of solubilisation by detergents. (A) Average lifetime component as a function of time in the presence of 0.06 mM (black), 0.2 mM (red), 1.0 mM (green) and 2.0 mM (purple) Tween20. (B) Average lifetime component as a function of time in the presence of 0.5 mM (black), 5.0 mM (red), 8.2 mM (green) and 10 mM (purple) SDS. (C) Average lifetime component as a function of time in the presence of 0.1 mM (black), 0.3 mM (red) and 1.0 mM (green) TX-100. Solid lines represent an exponential growth.

For Tween20, the end point saturation in average lifetime does not plateau at similar values for the concentrations. This is unexpected because, as predicated by the 3-state model observed in earlier experiments, the solubilisation of vesicles by Tween20 would result in the formation of micelles of similar lifetimes. One explanation for this difference could be due to Tween20 being considered a slow solubilising detergent and the acquired kinetics do not fully solubilise the vesicles in the time frame the data was collected between. This would explain, in part, the subtle change in lifetime observed for the lower concentrations 0.06 mM and 0.2 mM. As Tween20 has a relatively low CMC of 0.06 mM, it would be thought that concentrations above this value would result in faster solubilisation due to an increased saturation of the bilayer which can be seen for 1 mM and 2 mM. Another plausible explanation could be that the different concentrations results in different micelle morphologies. This insight has been implied before with the suggestion that micelles formed from Tween20 change with total concentration (*22*). This could also explain why the error bars seemingly increase as the concentration of detergent increases, seen in the titration-based experiments performed previously, because a large variety of different micelle morphologies would be present. Additionally,

this may also explain why the sigmoidal S-shaped fitting is not as defined as the other detergents. For the 2 mM sample, the data seemingly does not fit the exponential growth as well as the other concentrations. This may be due to this higher concentration being able to solubilise the vesicle at a higher rate and therefore the fast and slow components of the lifetimes, as previously discussed, is clearer. As for SDS, all concentrations plateau at ~0.8 ns and fitted to an exponential growth model, consistent with the biexponential behaviour of DiI previously described. This plateau occurs after approximately 10 minutes which suggests that the solubilisation by SDS is not a quick process. In comparison, acquiring the kinetics for TX-100 was difficult due to its rapid solubilisation of the vesicle. For concentrations above the CMC, the average lifetime component increased to values around the maximum seen in the previous experiments almost instantly. As the TCSPC instrument used in this work acquires the first data point 1 minute after the addition of the detergent, it appears that the vesicles are all either partially or fully solubilised within the first minute. Nevertheless, this data demonstrates that fluorescence de-quenching may be a useful tool in the context of evaluating time-dependent detergent-induced morphological changes in single lipid vesicles in solution.

3.1.2 Fluorescence De-quenching is an adaptable technique

3.1.2.1 Changes in lifetime for varying dye concentration, vesicle size and lipid composition.

To demonstrate the adaptability and robustness of the fluorescence de-quenching assay, further experiments were conducted to investigate how changes in experimental parameters, including dye concentration, vesicle size and lipid composition, affect the observed lifetime response. Establishing the consistency of the assay across these conditions is important for identifying optimal experimental settings and for validating its broader application to biologically relevant membrane systems.

200 nm POPC vesicles were prepared and labelled with 0.01 mol%, 0.1 mol%, 1 mol% and 1.5 mol% fluorescent dye DiI, to assess the magnitude of the self-quenching process as a function of dye content to establish the optimal concentration. For all the following experiments, the amplitude weighted average lifetime component was measured as previously described upon progressive addition of 0.02 mM TX-100. When the dye content

was reduced from 1% to 0.1% and 0.01%, the initial quenching magnitude decreased, as indicated by a progressive increase in lifetime in the absence of detergent from 0.59 ± 0.004 ns to 1.03 ± 0.02 ns (Figure 3.6A). However, at 1.5%, the initial lifetime value was similar to that obtained at 1%. In all cases, the fluorescence lifetime increased as a function of TX-100 concentration, and a de-quenched lifetime value of ~1.2 ns was reached after addition of TX-100 above the CMC. All reported half-maximal constants, as fitted by a Hill model, were within the range of the CMC for TX-100 between 0.19 and 0.35 mM (Figure 3.6B). These results indicate that 1% DiI provides an optimal balance between quenching sensitivity and reproducibility, while all dye concentrations converge to a similar de-quenched lifetime upon TX-100 induced vesicle solubilisation.

Additionally, since membrane curvature and surface area can strongly influence detergent-lipid interactions, POPC vesicles of varying diameters were created as previously described. This would therefore assess whether the assay is robust across different diameters and examine the effect of vesicle size. The created vesicles included SUVs of 30 nm, and LUVs of 400 nm, 1 micron as well as the 200 nm sized species prepared beforehand. In all cases, these vesicles were labelled with 1% DiI. For all diameters, the average fluorescence lifetime doubled from a similar initially quenched lifetime of 0.59 - 0.71 ns, and the concentration of TX-100 required to achieve a 50% increase in lifetime were in the range of the CMC, between 0.18 and 0.31 mM (Figure 3.6C and D). Finally, the response from neutral POPC vesicles were compared with negatively charged POPC/POPS mixtures to evaluate how lipid composition influences the de-quenching response, since membrane charge can alter detergent-lipid interactions. POPC/POPS mixtures are particularly relevant because they mimic the neuronal membrane. 200 nm vesicles containing 70% POPC and 30% POPS were created and labelled with 1% DiI and compared to 200 nm POPC only vesicles. A direct comparison of the de-quenching signal between these two components suggested slight variations in concentration of TX-100 required to achieve complete solubilisation (Figure 3.6E). For example, the PC/PS mixture increased by ~77% and the half-maximal constant was 0.26 mM, whereas the PC alone vesicles increased by ~113% with a half-maximal constant of 0.19 mM (Figure 3.6F). This difference in solubilisation sensitivity may be due to the difference in charge between the two lipids, with the PC/PS reducing membrane interactions via electrostatic repulsions.

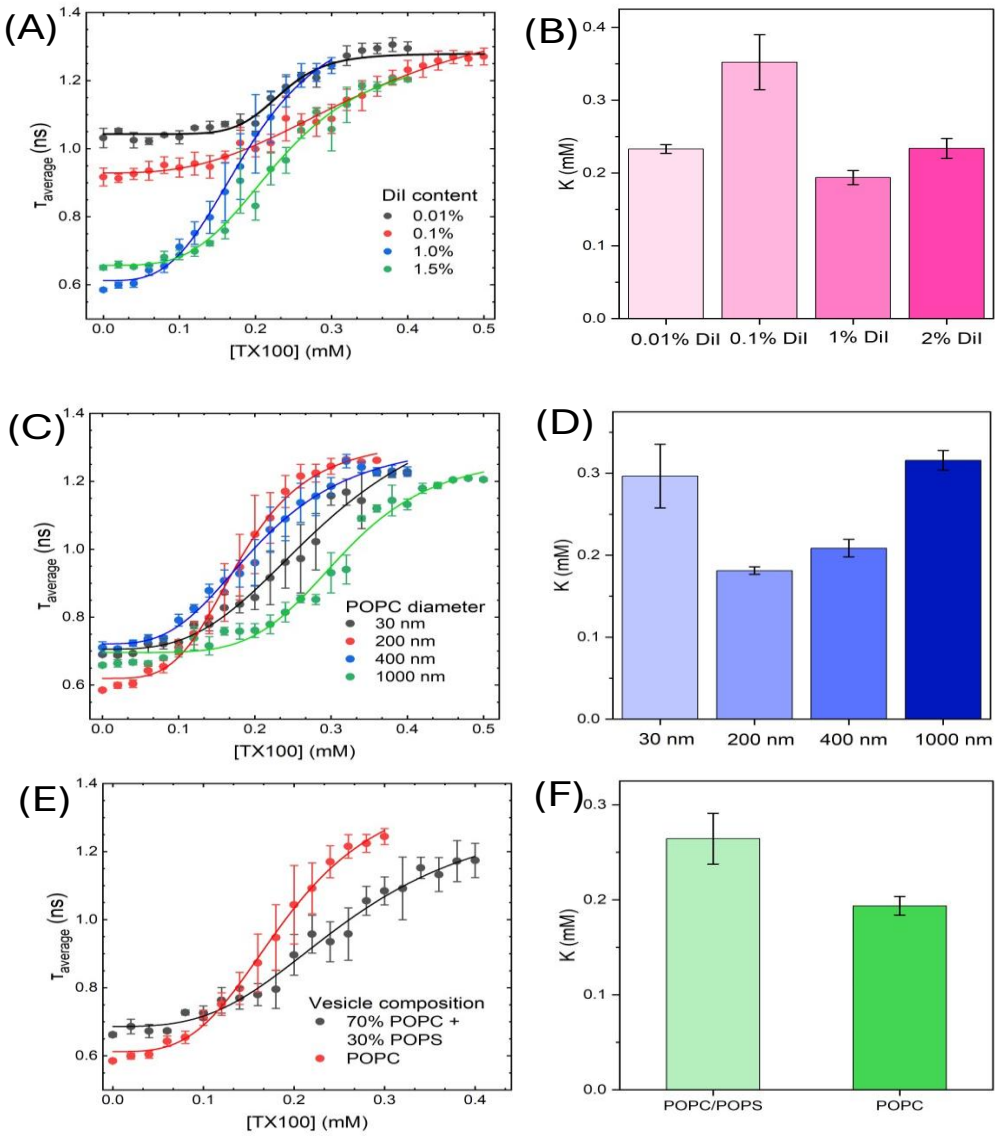

FIGURE 3.6 Variation in Fluorescence de-quenching signal as a function of vesicle size, dye content and lipid composition. (A) Average lifetime of 200 nm POPC vesicles labelled with 0.01 mol% (black), 0.1 mol% (red), 1.0 mol% (blue) and 1.5 mol% (green) DiI, as a function of TX-100 concentration. (B) Average lifetime of 30nm (black), 200 nm (red), 400 nm (blue) and 1000 nm (green) POPC vesicles labelled with 1.0 mol% DiI, as a function of TX-100 concentration. (C) Average lifetime of 200 nm 70 % POPC + 30 % POPS with 1 mol% DiI (black) and 200 nm POPC vesicles with 1.0 mol% DiI (red), as a function of TX-100 concentration. Data shown represents the mean values obtained from 3 experimental runs and error bars denote the standard error of the mean.

The results from varying the dye content, as seen in Figure 3.6A and B, show that decreasing the concentration of fluorophore DiI causes an increase in the initially quenched lifetime component. This is consistent with the notion that if the bilayer is less saturated with fluorophores, the separation between the two would be greater and therefore the observed fluorescence intensity and average lifetime would increase. As detergent is added, the end point saturation in lifetime plateaus at 1.2ns for all dye concentrations which is consistent with the comparable end stage morphologies due to the formation of micelles at these concentrations of detergents. The results suggested that the optimal concentration of dye to use was 1% as this was the lowest doping concentration whilst retaining a high sensitivity.

When investigating the differences between the diameters of LUVs, it was found that the overall trend in the sigmoidal increase in average lifetime starting around 0.65 ns was present across all vesicle sizes tested. As seen in Figure 3.6C, a slight pattern emerges in which larger diameter vesicles (1000 nm and 400 nm) require slightly higher concentrations to solubilise relative to the 200 nm case. This can also be seen in the difference in half maximal concentration values recovered from the Hill model fits where the concentration required to reach 50% of the maximal lifetime increases with size in the order 1000 nm > 400 nm > 200 nm (Figure 3.5D). Where the difference in half-maximal values is not statistically significant between the 400 nm and 200 nm vesicles ($p = 0.35$, paired t-test), the half-maximal value for 1000 nm vesicles is significantly greater ($p < 0.001$, paired t-test). The exception to this trend appears to be with the 30 nm vesicles, which required similar concentrations to the larger 1-micron sized vesicles of ~0.3mM. Whilst this remains in the range of TX-100's CMC, the large error bars are suggestive of a variety of vesicle population present at this concentration. This may be due to the extreme curvature of the 30 nm vesicles which alters lipid packing and reduces detergent insertion efficiency, leading to a response more similar to the very large vesicles, which also resist solubilisation due to their bulk-like bilayer organisation. The intermediate vesicles (200 nm – 400 nm) may represent a 'sweet spot' where curvature and lipid packing balance out, making them somewhat more susceptible to the detergent's action.

Finally, compositions of LUVs were compared using a 70: 30 POPC: POPS mixture. Whereas POPC alone is neutrally charged at physiological pH, POPS is negatively charged. This means that the incorporation of this phospholipid into the LUVs gives an

overall slight negative charge, representative of cell membranes. Because of this property, the POPC/POPS mixture is commonly used as a simple model of the inner leaflet of plasma membranes (*148*). Not only is it important to investigate the effect of this difference in charge, but also to confirm the suitability of these LUVs as a model for the mammalian membrane in future experiments. Both compositions follow the sigmoidal trend with similar obtained half maximal values around the CMC (Figure 3.6F). The PC/PS mixture required higher concentrations to solubilise the membrane with may be due to the detergents incorporating into the membrane slower due to the negative charge of the lipid. POPS increases the electrostatic interactions and membrane cohesion, making the bilayer more resistant to detergent insertion, therefore requiring a higher TX-100 concentration to reach solubilisation. Indeed, this behaviour has been observed before as PS-rich membranes create an electrostatic repulsion between the vesicle and detergent (*149*). Both compositions however experienced similar initial quenched values and plateaued around 1.2 ns, which is consistent with the solubilisation mechanism previously seen.

These results suggest that TX-100 induced solubilisation is dependent on the curvature and size of the vesicles and is related to the lipid composition. Therefore, these experiments serve as a starting point for addressing a wide range of additional experiments using the de-quenching approach. Future experiments could result in valuable information about the sensitivity of the vesicles and fluorophores as the local environment changes. For example, investigating the effects of temperature, differences between the chosen fluorescent dye such as DiO and DiD, as these are sensitive to different wavelengths. Alternate vesicles compositions could also be studied as an investigation into the effects of the lipid charge such as positively charged membranes.

3.1.2.2 Characterisation of vesicle sizes using Dynamic Light Scattering

Alongside the 200 nm POPC vesicles previously described, Dynamic Light Scattering (DLS) was used to investigate the homogeneity and diameters of the 200 nm POPC/POPS and 1 µm POPC vesicles. Solutions of these vesicles were dispersed in 50 mM Tris (pH 8) and the hydrodynamic radius was determined. For the 200 nm POPC/POPS vesicles the

average diameter was given to be 158.46 ± 0.24 nm (Figure 3.7A) and for the 1µm POPC vesicles, the average diameter was given to be 813.46 ± 26.92 nm (Figure 3.7B).

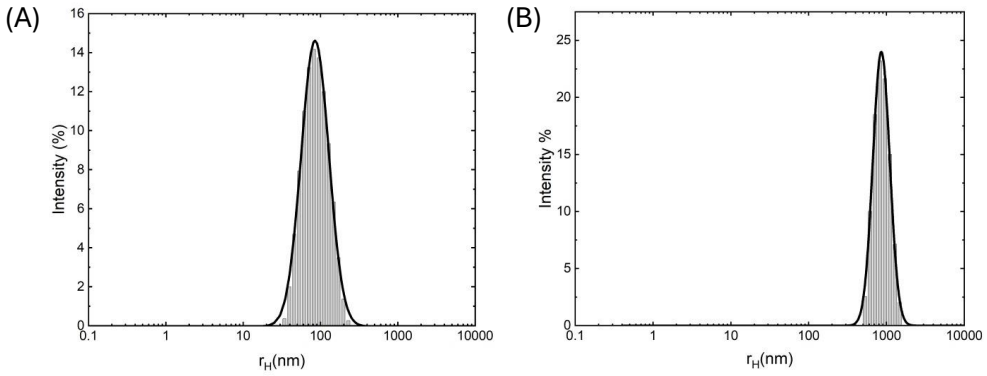

FIGURE 3.7 Representative hydrodynamic radius (r_H) distribution of extruded LUVs obtained via dynamic light scattering. The size distribution of (A) 200 nm POPC/POPS (µ = 219.2 ± 1.2, σ = 83.8 ± 1.4) and (B) 1 µm sized vesicles (µ = 947.5 ± 2.3, σ = 240 ± 2.4). Solid lines represent lognormal fits (R^2 = 0.99 for both).

The results from the DLS suggest that creating the lipids via extrusion is a reliable technique as for all samples the determined hydrodynamic radius was approximately similar in size to the membrane pore size used. DLS has been proposed as a suitable technique for vesicle characterisation due to its simplicity and efficiency when analysing homogenous samples (*150*). However, the technique is limited by its sensitivity to particle contamination and temperature, meaning that artifacts in the samples can result in inaccurate data (*151*). Another technique that compares to DLS is the use of nanoparticle tracking analysis (NTA) which similarly uses Brownian motion to estimate particle size but is able to provide particle-by-particle analysis, rather than the averages obtained by DLS (*152*). The slight horizontal shift left in the graphs seen in Figure 3.7 can be explained by the decrease in homogeneity that is experienced when using greater pore sizes. As the membrane pore increases, there would be an increase in smaller vesicles passing through alongside the desired larger vesicles. This behaviour can be highlighted by the larger distribution and error bars seen in the 1 µm sample compared to the smaller 200 nm vesicles. It is clear from the data that extrusion does not guarantee consistent homogeneity in the vesicles as there is an observed difference between the 200 nm POPC vesicles compared to the same sized POPC/POPS mixture. This could be due to human error during the process such as different forces applied during extrusion, as previous

studies looking into this relationship has shown that as the applied force increases, the size of the extruded vesicles decreases. The use of an automated system that guarantees a constant pressure is applied has been shown to bypass this problem however the manual extrusion using gas-tight syringes was chosen moving forward as this is more cost-effective given the high number of samples produced throughout the experiments (*153*).

3.1.3 De-quenching is as sensitive as FRET for monitoring membrane disruptions

200 nm POPC vesicles were prepared via the extrusion method and labelled with a 1:2 ratio of donor (DiD) and acceptor (DiI) dyes, optimised such that the average FRET efficiency per vesicle was initially 0.5 (Figure 3.8A). TX-100 was progressively added in steps of 0.02 mM and the resulting background-corrected spectra was measured in the range of 535 – 800 nm (Figure 3.8B inset). The apparent efficiency of energy transfer (E_{FRET}) was then calculated using the equation $E_{FRET} = I_A / (I_A + I_D)$, where the intensity of the donor (ID) was measured at 565 nm, and the intensity of the acceptor (IA) was measured at 665 nm. As the concentration of TX-100 increased, the donor and sensitized acceptor emission intensities were anticorrelated (Figure 3.8C), which is the classic hallmark of FRET, and the value for E decreased from an initial value of 0.6 ± 0.005 in the absence of the detergent to 0.09 ± 0.003 in the presence of 0.6 mM (Figure 3.8B). As shown in Figure 3.9, with the addition of detergent the donor signal increases while the acceptor signal decreases and for both intensities, the value begins to plateau at concentrations beyond ~0.4 mM. When comparing this data to the fluorescence de-quenching lifetime data previously described, as seen in Figure 3.8D, the mean variation in FRET efficiency (negative signal) was anticorrelated with the mean average lifetime of DiI (positive signal). This suggests that the single colour fluorescence de-quenching approach is as sensitive as the dual-colour FRET-based assay in the context of TX-100 induced membrane solubilisation and likely enables nanoscale interactions between fluorophores to be monitored on the nanoscale.

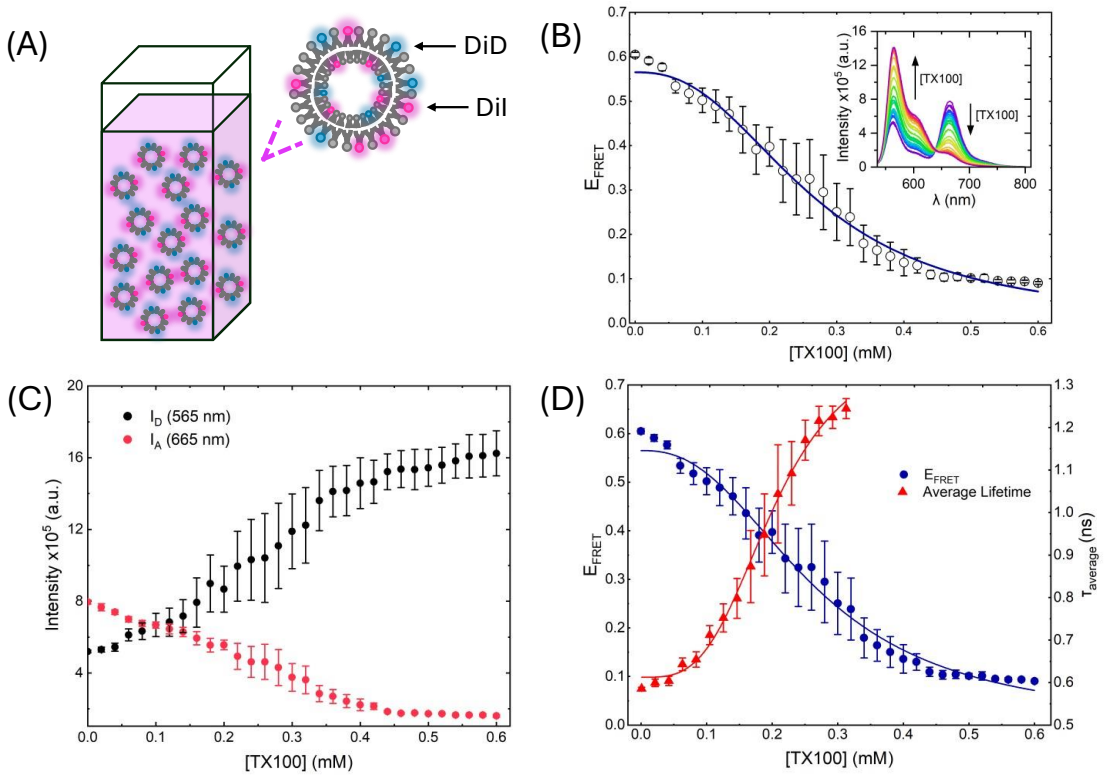

FIGURE 3.8 Comparison of a dual-colour FRET efficiency assay to the single-colour fluorescence de-quenching approach. (A) Schematic of LUVs labelled with a 1:2 ratio of donor (DiI) and acceptor (DiD) dyes. Inset: schematic of FRET vesicle. (B) FRET efficiency of DiI: DiD labelled POPC vesicles as a function of TX-100 concentration. The solid blue line represents a Hill model fit ($k = 0.27$ and $R^2 = 0.99$). Inset: corresponding variation in fluorescence spectra with λ_{ex} = 532 nm. (C) Mean Intensity of donor and acceptor dyes as a function of TX-100 concentration. (D) Comparison of the de-quenching fluorescent lifetime experiment (red) to FRET (blue) for monitoring membrane disruption. Data shown represents the mean values obtained from 3 experimental runs and error bars denote the standard error of the mean.

During FRET, excitation of the donor fluorophore DiI promotes non-radiative energy transfer to the acceptor DiD, and a high efficiency of energy transfer represents close proximity of the dyes (*72*). The results highlighted in Figure 3.8B indicate that as TX-100 is progressively added to the vesicles the FRET efficiency decreases, which is suggestive of a morphological change that increases the inter-dye separation between both fluorophores. This is because the non-radiative energy is transferred through dipole-

dipole interactions therefore the closer the molecules are, the stronger the interaction and the more efficient the energy transfer is (*154*). Indeed, this decrease in efficiency, particularly at concentrations below the TX-100 CMC is suggestive of vesicle swelling and expansion prior to solubilisation. These results are also supported by previous research which used single particle FRET imaging to show that, following addition of TX-100, the radius of LUVs expands by ~1.2 times prior to lysis and micellization (*29*). Combining the two datasets, as shown in Figure 3.8D, allows direct comparison between the sensitivity of the two techniques for monitoring the mechanistic details of membrane solubilisation on the nanoscopic level. While further analysis is required, the de-quenching approach may be subtly more sensitive to membrane disruption, as the maximum value (representing the formation of mixed-micelles by the detergent) occurs at a lower concentration of TX-100. Additionally, the half-maximal constant obtained from the FRET assay was 0.27 mM which is greater than the half-maximal constant from the fluorescence de-quenching assay (0.18 mM).

Both fluorescence-based approaches can be used to monitor detergent-induced solubilisation of the membrane, however the experiments conducted suggest that fluorescence de-quenching may be more advantageous due to its capability to bypass some of the complications associated with FRET. For example, FRET requires precise donor-acceptor stoichiometry to ensure that the FRET efficiency per vesicle is ~0.5. It also relies on fluorophores with similar quantum yields and detection efficiencies, and any photophysical variations in one dye, e.g. pH-induced photobleaching, can manifest itself as a change in FRET efficiency and create signal-to-noise ratio problems. Another limitation associated with conventional FRET-based approaches is donor bleed through into acceptor channels, can make accurate distance determination challenging. While further experiments are required to validate the distance associated with the de-quenching technique, it can be hypothesised that it operates over similar inter-dye separates with capability of encompassing a larger distance range than FRET, which is most effective between ~1 - 10 nm. The key advantage of the fluorescence de-quenching approach, is that it only requires one fluorescent dye, therefore bypassing some of the problems associated with FRET-based approaches. Ultimately, this makes the assay less complex in terms of quantitative characterisation, though not without its own limitations. For example, changes in fluorescence intensity and lifetime could arise from variations

in local dye environments such as concentration, packing and aggregation, and photophysical artifacts including photobleaching. Furthermore, membrane interactions have potential to complicate interpretations. Nevertheless, it is clear from the data presented that the de-quenching technique can effectively reveal morphological changes in vesicle architecture, and in principle, the technique can be used for further investigations, looking at membrane disruption by a wide range of molecular disruptors, including antiviral agents, novel detergents and proteins with biomedical significance.

3.2 Conclusions and Future Work

In this chapter, the results presented support the use of intramembrane fluorophore de-quenching as an appropriate, single colour fluorescence-based approach for monitoring the solubilisation of model membrane vesicles by detergents. The adaptability of this technique was explored using various detergents, dye concentrations, vesicle sizes and composition. For all these variables, measuring changes in the amplitude weighted average lifetime component using TCSPC showed increases in value with the progressive addition of detergent, even at concentrations below the CMC, suggesting morphological changes such as swelling before complete solubilisation, in line with the previously identified 3 state model of solubilisation (*24*). This work indicates that de-quenching can be an applicable technique for a range of investigations involving quantitative analysis of changes to the vesicle structure induced by perturbative agents. Furthermore, direct comparison between the de-quenching approach and established FRET assays highlight the nanoscale sensitivity of the technique, and the requirement for only a single fluorophore offers significant advantages over the FRET-based strategy. This includes avoiding the need for accurate donor-acceptor stoichiometry and spectral bleed through. Despite the showcased ability of the de-quenching assay, there remains several associated limitations, owing in part to its capability being unexplored. For example, fluorophore photophysics such as photoblinking or photobleaching may contribute to the observed signal, and dye aggregation may convolute interpretations. Beyond the technical limitations, the acquisition of fluorescence lifetime data requires fast TCSPC electronics, and while the technique is maturing, this may not be available in all laboratory settings. Additionally, the high intensity laser pulses required for TCSPC

analysis may induce both photodamage and photophysical phenomenon. As such, further research is required to relate the corresponding changes in lifetime to accurate distances, in a manner similar to those calculated for FRET-based approaches. Nevertheless, the data presented provides confidence that the fluorescence de-quenching approach accurately reports on detergent-induced membrane solubilisation and can be used as a tool to quantify concentration constants required for membrane solubilisation, kinetics of the process, and morphological changes at sub-solubilizing detergent concentrations. Although some variables were explored and optimal conditions of the de-quenching assay were obtained, future work would benefit from exploring how other environmental factors such as temperature, pH, charge and salinity affect the de-quenching signal. Secondly, the results from changing the dye concentration indicated that de-quenching could report on nanoscale distances even at DiI concentrations as low as 0.001 mol%. Overall, these experiments support the use of a new ensemble-based fluorescence de-quenching assay for reporting detergent-induced vesicle solubilization, and it can be predicted that further research will be able to use this technique for investigating membrane interactions with biological matter such as proteins.

4. Detection of Morphological Changes Induced by Triton X-100 at the Single Vesicle Level

In this Chapter, the mechanism of detergent-induced changes on model membranes is explored at the single vesicle level. The ability to observe fluorescence de-quenching from single vesicles is highlighted using fluorescence lifetime imaging and Micro-photoluminescence detection approaches. Furthermore, this chapter examines detergent-induced morphological changes and vesicle restructuring at the single vesicle level using Electron Microscopy. Altogether, these experiments further explain the intermediate stages of solubilisation prior to lysis by the non-ionic detergent TX-100, and refine the 3 state model.

4.1 Results and Discussion

4.1.1 Detection of single vesicle de-quenching using Micro-Photoluminescence

1 μm sized POPC vesicles were prepared via the extrusion method and labelled with 1 mol% fluorescent dye DiI. 1 μm vesicles were used in this experiment to match the laser spot size and therefore minimise the number of vesicles monitored. (Figure 4.1A). These were then non-specifically immobilised onto glass microscope slides using poly-L-lysine and varying concentrations of TX-100 were added to the vesicles in steps of 0.1 mM, up to 0.5 mM. The resulting fluorescence emission spectra obtained from single vesicles per field of view was measured with an excitation wavelength of 532 nm, with a 50x objective lens and a 1 μm spot size used to generate the excitation field. The results from this Micro-Photoluminescence (Micro-PL) approach demonstrate that the fluorescence intensity of single surface-immobilized vesicles significantly increases as the concentration of detergent increases, up to the CMC (~0.3 mM) suggestive of an increase in DiI-DiI separation and vesicle swelling. At concentrations beyond the CMC, the intensity was then found to decrease which likely reflects lysis and release of DiI into solution (Figure 4.1B). As shown in Figure 4.1C, the maximum intensity increases by 8 times when 0.2 mM TX-100 is used compared to the absence of the detergent. Vesicle samples were also diluted by a factor of 10 (Figure 4.1D) and 100 (Figure 4.1E) to further decrease the

number of vesicles monitored at once and reduce the probability of the emission signals being acquired from aggregates of multiple species. The spectral enhancements observed here are consistent with fluorescence de-quenching and further support the use of the technique for probing vesicle damage at the single vesicle level.

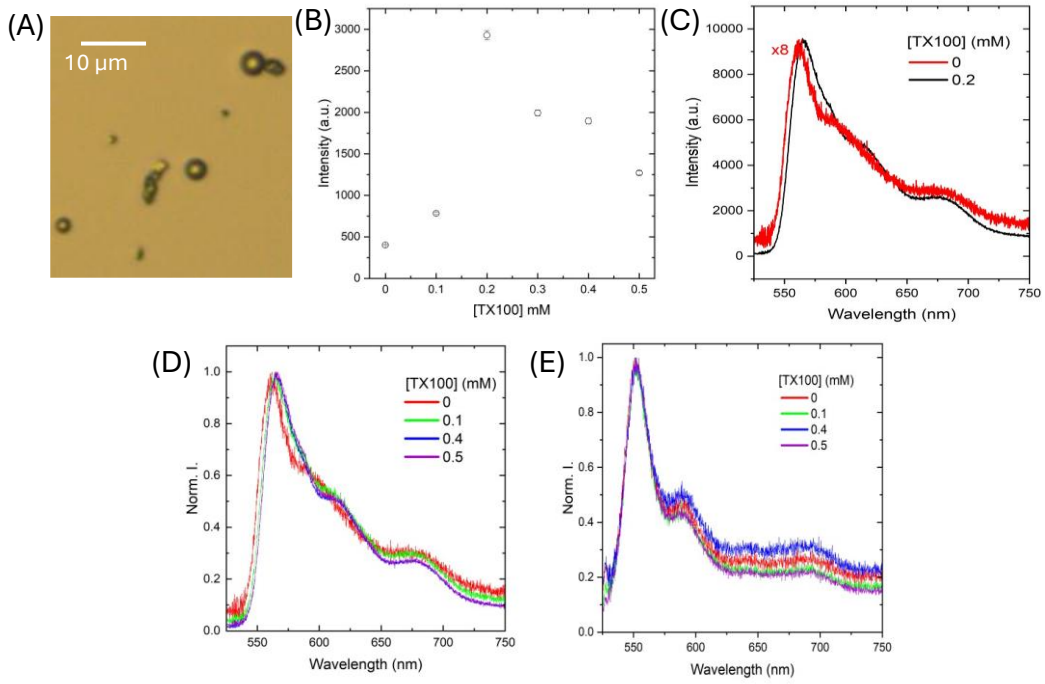

FIGURE 4.1 Detection of fluorescence de-quenching from single vesicles. (A) Example image of 1µm vesicles. (B) Integral fluorescence intensity obtained from 1 µm POPC vesicle with 1% DiI as a function of TX-100 concentration. (C) Fluorescence intensity spectra from the absence of TX-100 (multiplied by a factor of 8) and 0.2 mM TX100. Normalised fluorescence intensity spectra from 1 µm vesicles (D) diluted 10 times (E) and 100 times.

The use of Micro-Photoluminescence (Micro-PL) allows for the detection of fluorescence de-quenching from single vesicles (Figure 4.1A). To ensure that the obtained emission spectra was from a single LUV, the vesicles used in the experiment were of a similar size to the laser spot size (1 micron). This was able to show fluorescence de-quenching behaviour as seen in Figure 4.1A as increasing fluorescent intensities were observed as the concentration of TX-100 increases – up to the CMC. Furthermore, at concentrations greater than 0.3 mM, the intensity decreased. Interestingly, this decrease in intensity at concentrations greater than the CMC is different from that observed in the ensemble

experiments. In the ensemble assay, the fluorescent intensity seemingly plateaus at a maximal value similarly to the lifetime rather showing this decrease. This difference in observation could be explained by vesicle lysis, which would result in the fluorescent dye leaking into the solution and decreasing in intensity. Another reason for this could be due to photobleaching experienced during the assay. Previous research has indicated that fluorophores experience stronger photobleaching effects when in micelles compared to within intact vesicles due to electrostatic interactions (*155*). This photobleaching of the fluorophores was a commonly experienced problem during the acquisition of data and persisted amongst varying laser powers. To mitigate against this as best as possible, the measurements were obtained rapidly over the period of only 1 second with low excitation powers of 1 mW. Another problem encountered during this experiment was the vesicles appeared to be more concentrated in certain areas, making them more difficult to find with the small spot size. This could be explained by the vesicles aggregating together – making some areas sparser and others highly saturated with the lipids. This hypothesis is further supported by Figure 4.1C which showed a small red shift of approximately 8 nm can be seen with the addition of 0.2 mM detergent. This suggests that the original measurements may have been acquired from multiple vesicles clustering together rather than the intended single vesicle. Indeed, previous research has shown that the addition of TX-100 can promote this aggregated behaviour (*16*). To overcome this problem, the sample was diluted by a factor of 10 and 100 using Tris buffer. As seen in Figure 4.1D, diluting the sample by a factor of 10 minimised the observed red shift but did not entirely solve the issue. On the other hand, as shown by Figure 4.1E, diluting by a factor of 100 seemingly reduced the capability of vesicles to cluster and the red shift was no longer observed. Although dilution of the sample appeared to decrease vesicle aggregation, further experiments would benefit from the use of a micro-array plate, which consists of shallow wells typically between 1 and 5 μm in size, to ensure this separation. This however would require using GUVs as opposed to LUVs. Alternatively, visualisation of the sample using microscopy during acquisition would be able to confirm that data is taken from single vesicles. One thing that should be acknowledged is the notable change in spectral shape between the factor of 100 dilution and the previously samples. For concentrations of TX-100, 0.2 and 0.3 mM, there is a dramatic increase in intensity at the second shoulder peak (~600 nm) and a stark increase at ~700 nm that is not seen in other

DiI spectra. It is likely that this characteristic is due to the dilution rather than being an anomalous result due to its presence in all 5 acquisitions per concentration. Whilst this change of spectral shape requires further investigation, the shoulder peak could reveal subtle details about the molecular interactions and transitions that occur within the sample. Additionally, it would be valuable to investigate if this shape change occurs at varying dye concentrations.

4.1.2 Lifetime Distributions from Single Vesicles using Fluorescence Lifetime Imaging

Fluorescence lifetime imaging (FLIM) was performed to assess the distribution of lifetimes from single DiI labelled vesicles. 200 nm LUVs composed of 99% POPC and 1% DiI were prepared via the extrusion method previously described. These were then non-specifically immobilised on a coverslip using 1% poly-L-lysine as detailed in the Methodology. The variation in lifetime distribution across the surface and amongst single vesicles was monitored before and after the addition of TX-100 at 0.15 mM, as an example of a sub-solubilising concentration of the detergent. In the absence of TX-100, fluorescent foci ~200 – 300 per 190 x 190 μm^2 field of view was observed, representing individual non-specifically bound vesicles (Figure 4.2A). As detergent is added to the vesicles, the total number of fluorescent foci per view and therefore the number of in-tact vesicles on the surface, remained largely invariant (Figure 4.2B). The distribution of individual lifetime components obtained across single vesicles was Gaussian distributed with a full width at half-maximum of ~0.2ns, indicating a lack of fused, aggregated or significantly perturbed species on the surface (Figure 4.2C and D). The distribution of lifetime values fitted well to a bi-exponential model with an observed increase in average lifetime by ~68% to 1.671.67± 0.34 ns when 0.15 mM TX-100 was added to the sample (Figure 4.2E) and an increase in both the fast and slow components (τ_{fast} = 1.32 ± 0.09 ns and τ_{slow} = 2.27 ± 0.04 ns), as seen in Figure 4.2 F and G. Furthermore, as detergent is added, the contributions of the lifetime components appears to change to become slower component dominant, as seen by the decrease in the corresponding ratio of amplitudes associated with the fast and slow components (A τ_{fast} /A τ_{slow}) shown in Figure 4.2H.

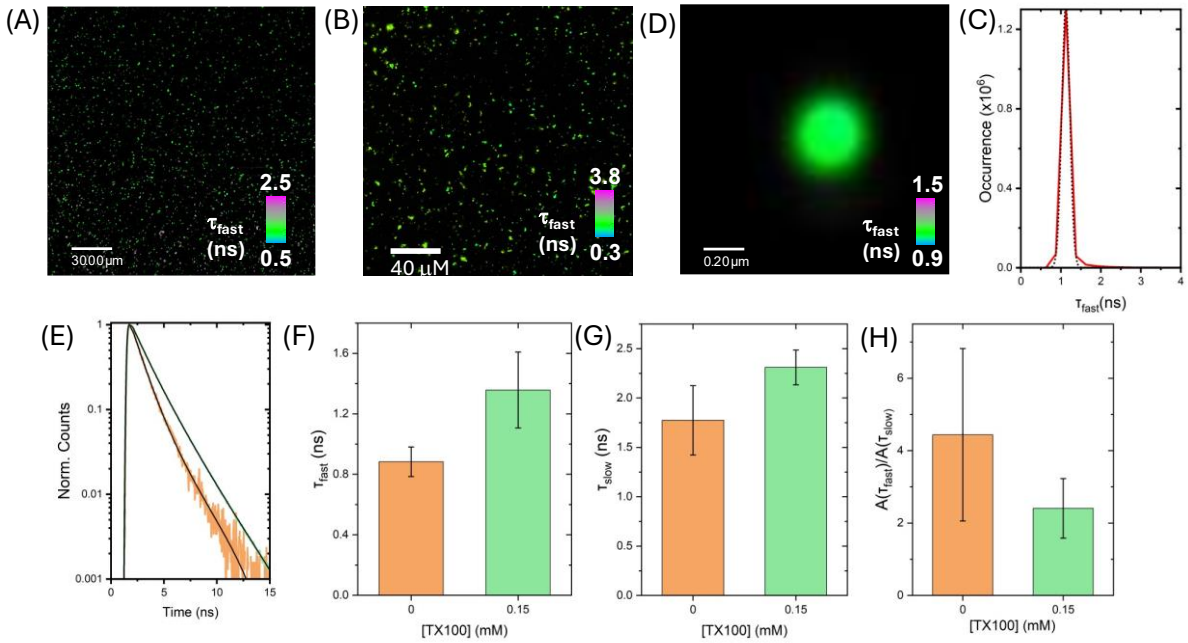

FIGURE 4.2 Variation in Fluorescence Lifetimes of Single Vesicles. Representative FLIM image of surface-immobilised 200 nm POPC vesicles labelled with 1 mol% DiI, in the absence (A) and presence of 0.15 mM TX-100 (B) showing variations in fast component, τ_{fast} across the field of view. C) The corresponding distribution of τ_{fast} values across the vesicle surface. The dotted black line corresponds to Gaussian fit with centre of 1.12 ns, full width at half maximum of 0.2 ns and R^2 = 0.99. D) Representative FLIM image of a single DiI-vesicle (no detergent) showing variations in fast component, τ_{fast}, across the structure. (E) Variation in TCSPC FLIM decays recorded from vesicles in the absence (orange) and presence of 0.15 mM TX-100 (green). Comparative bar charts summarizing the mean variations in F) τ_{fast}, G) τ_{slow}, and H) $A(\tau_{fast})/A(\tau_{slow})$ obtained from N = 5 randomly selected immobilised vesicles. Error bars correspond to the standard deviations.

An important thing to note is that throughout the single-vesicle Fluorescence Lifetime Imaging (svFLIM) measurements, the immobilised vesicles were spatially isolated on the surface as to minimise the possibility of vesicle fusion that has previously been suggested to occur prior to solubilisation with the addition of TX-100. The increase in lifetime observed across single vesicles at low TX-100 concentrations could therefore be attributed to structural changes taking place within the in-tact vesicles, as opposed to complete solubilisation or lipid cell lysis. Furthermore, this supports the idea that the observed de-quenching signal is due to detergent-induced remodelling of the membrane in a mechanism that involves vesicle swelling and/or morphological changes with

minimal loss of lipid material to the bulk solution. Indeed, these results are in line with the previous ensemble-based fluorescence de-quenching measurements, as the distribution of lifetime values from hundreds of surface-immobilised vesicles also fitted well to a bi-exponential model (Figure 4.2C). These observations were also reflected when random sampling of the mean component lifetimes per vesicle revealed a 1.5-fold increase in τ_{fast} (Figure 4.2F) and a 1.3-fold increase in τ_{slow} (Figure 4.2G). Additionally, the corresponding ratio of amplitudes associated with the fast and slow components decreased from 4.4 ± 1.1 to 2.4 ± 0.8 (Figure 4.2H), suggesting that TX-100 alters lipid microenvironment, disrupting dye-dye interactions that favour the fast lifetime component.

4.1.3 Triton X-100 induces morphological changes to model membrane vesicles

4.1.3.1 Monitoring morphological changes to 1-micron sized vesicles

In addition to the fluorescence-based analysis, DiI labelled 1-micron sized POPC vesicles were imaged with SEM. Vesicles were imaged with and without the addition of 0.3Mm TX-100 under vacuum, as seen in Figure 4.3A and B. Acquired images were analysed using ImageJ, and the diameter, area, and circularity of N = 50 vesicles from each sample was evaluated. Figure 4.3C shows the variation in vesicle diameter determined by SEM, where the mean diameter of vesicles without detergent upon addition of detergent increased by approximately 60%, from 0.74 ± 0.04 μm to 1.17 ± 0.05 μm. An important thing to note is that the vesicle size obtained from SEM is generally smaller than from DLS due to the requirement to dehydrate the sample. This significant increase was also seen in vesicle area, as shown in Figure 4.3D. These increases are consistent with vesicle swelling, as suggested in the lifetime assays. Figure 4.3E shows a significant difference in circularity with the addition of TX-100, where the vesicles become more elongated.

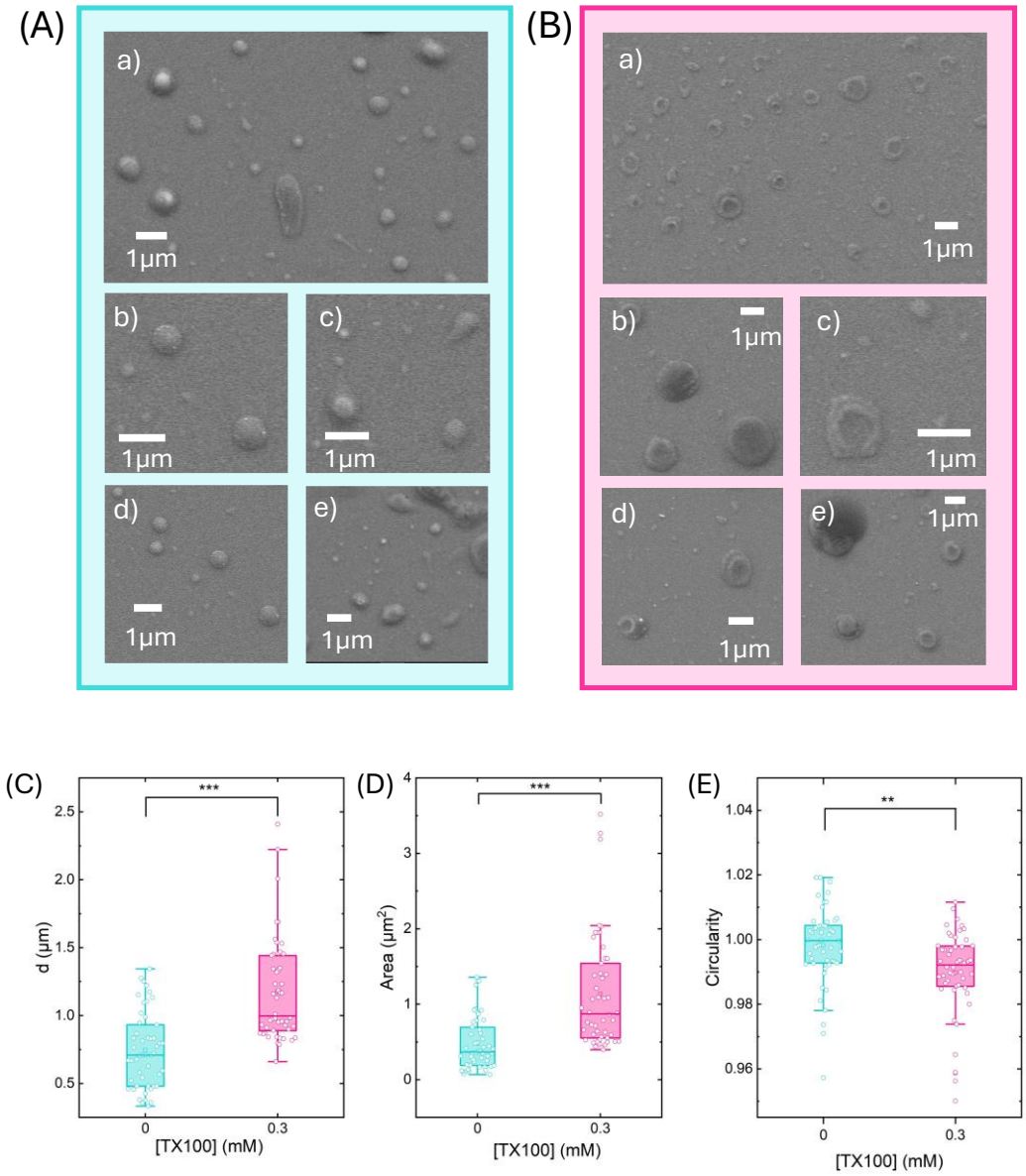

FIGURE 4.3 Vesicle size and morphology evaluated by Scanning Electron Microscopy. A) Example images taken of 1-micron vesicles with SEM with (a) widefield and (b-e) single vesicle images B) Example images taken of 1-micron vesicles with 0.3 mM TX-100 with SEM with (a) widefield and (b-e) single vesicle images. C) Box plot of vesicle diameters measured from SEM images with N = 50 for without TX-100 (blue) and with 0.3 mM TX-100 (pink). D) Box plot of vesicle area with N = 50 for without TX-100 (blue) and with 0.3 mM TX-100 (pink). E) Box plot of vesicle circularity with N = 50 for without TX-100 (blue) and with 0.3 mM TX-100 (pink). *** = $p < 0.001$ and ** = $p < 0.01$(paired t-test).

The SEM images acquired showed that the addition of TX-100 induced a change in morphology in the vesicles. The concentration of 0.3 mM for TX-100 was chosen as this is within the range of the CMC. This would therefore expect to show any changes in shape and size as the vesicles begin to solubilise, without causing complete micellization of the membrane. As seen in Figure 4.3A and B, the vesicles change from being spherical to toroidal in shape. This change is also quantifiable as the average area and diameter increases by 1.5 times with the addition of detergent at the concentration used. This evidence is supportive of the increase in lifetime, seen in the de-quenching assay, being due to vesicle expansion rather than other factors such as changes to the local environment. The toroidal shape suggests that the detergents are creating variations in the fluidity of the membrane that leads to membrane collapse and formation of the ring-like topologies as observed in the SEM images. Previous research has suggested that toroidal pores created in membranes and LUVs are a common disruptive mechanism by antimicrobial peptides – coined the carpet model (*156*). In this, the accumulation of peptides on the outer membrane induces a positive curvature on perpendicular to the membrane but a negative curvature around the formation of the pore. This toroidal shape also could contribute to the formation of the micelles during complete solubilisation due to fusion between the inner and outer lipid monolayer at the location of the pore. This would increase the transbilayer movement of the lipid molecules and increase the likelihood of complete solubilisation. The change is curvature is also supported by the decrease in circularity seen in Figure 4.3D. This suggests that the vesicles become more elongated and elliptical with the addition of detergent which is consistent with invagination prior to solubilisation. As the detergent molecules incorporate into the membrane, they likely induce high curvature stress and cause the membrane to curve inwards on itself until micelles eventually shed from the vesicles. Whilst the results are supportive of detergent-induced morphological changes, the SEM images only provide insight into the 2D effect. Further confirmation of the 3D structure, for example, via electron tomography, would provide insights into the entire conformation of the vesicles and effect of the detergent across the entire volume. It would also be of value to investigate if these morphological changes are consistent with different properties of the vesicles (e.g. curvature and lipid composition), as previously looked at with the lifetime experiments to assess whether toroidal geometries are a general property of the

solubilisation process or specific to 200 nm sized POPC vesicles. Additionally, as TX-100 is a fast-solubilising detergent, it can be thought that its mechanism for disruption is different from a slow solubilising detergent such as SDS due to its ability to incorporate and flip the bilayer at a faster rate, and it remains unclear whether toroidal geometries are formed with other such surfactants. This difference in solubilisation could therefore result in different morphological features and the toroidal shape may not be consistent with all classifications of detergents. Nevertheless, the observation seen here provides valuable insight into mechanisms used by detergents and refines the 3-stage model: morphological variations of single vesicles take place prior to complete solubilisation.

4.1.3.2 Monitoring changes to GUVs

Building on previous findings that studied the impact of TX-100 on LUVs, the study was next extended to analyse giant unilamellar vesicles (GUVs) to test whether the same fluorescence de-quenching behaviour could be observed at larger length scales. GUVs composed of 99% POPC and 1% DiI were prepared as detailed in the Methodology. The size of the prepared GUVs were confirmed using widefield microscopy and SEM. In this, the vesicle sample is added to a flow-cell microscope slide, as described in the methodology, and visualised using a 100x magnification objective lens and 532 nm excitation wavelength (Figure 4.4A). Additional images of GUVs with the addition of 0.5 mM TX-100 were also taken, where the formation of micelles can be seen (Figure 4.4B). Further morphological changes were also seen with the addition of 0.3 mM TX-100, using SEM, as seen in Figure 4.4C and D. In this, a clear pore can be seen within the vesicle. Acquired widefield images were analysed using ImageJ and calculated to have an average diameter of 5.96 ± 0.41 µm (n = 61) as seen in Figure 4.4E. TX-100 was progressively added to the vesicles in steps of 0.02 mM and the amplitude weighted fluorescent lifetime was measured with an excitation wavelength of 532 nm by Time Correlated Single Photon Counting (TCSPC). The GUVs show the fluorescence de-quenching behaviour as seen in Figure 4.4F. Upon TX-100 addition, the average lifetime increases from an initially quenched value of ~0.78 ns to 1.4 ns, at which point the lifetime exhibits the expected plateau in line with solubilisation. Furthermore, the half-maximal value, as predicted by Hill model fitting, occurs at 0.21 mM which is within the range of the CMC (Figure 4.4G). The overall trend in average lifetime follows a similar a pattern to the varying large POPC vesicles previously analysed and the half-maximal constant remains with the range of the

CMC. This supports the idea that fluorescence de-quenching is applicable for both large and giant unilamellar vesicles.

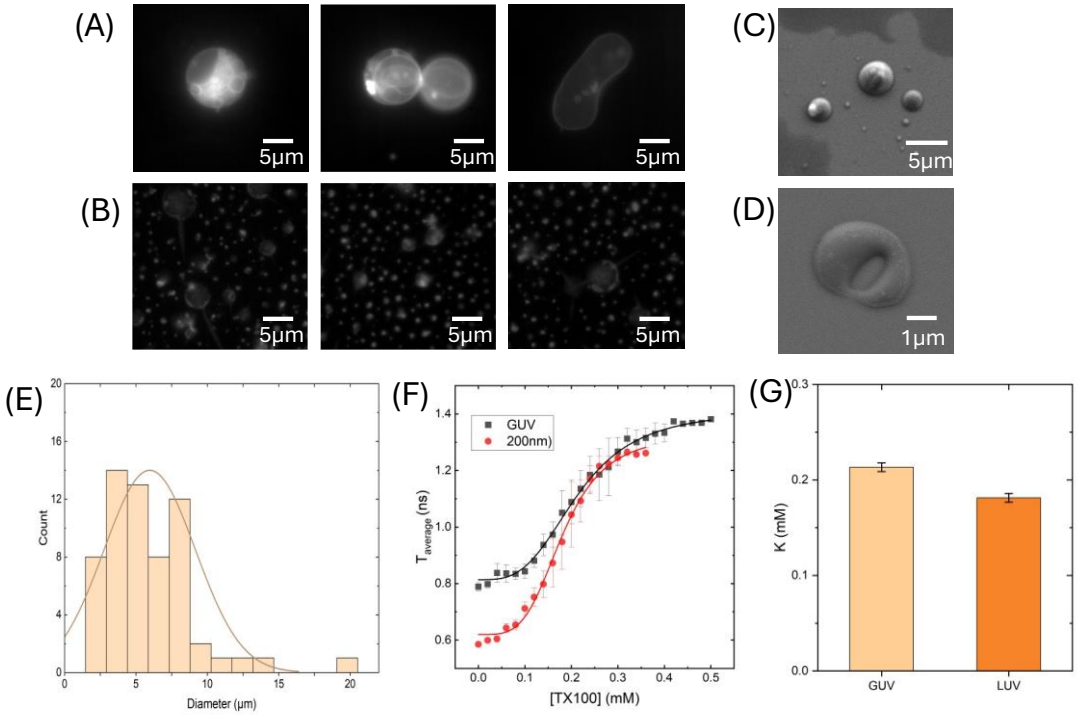

FIGURE 4.4 Fluorescence de-quenching observed in GUVs. Example images of GUVs visualised from widefield microscopy (A) without detergent and (B) with the addition of 0.5 mM TX-100. Example images of GUVs visualised from SEM (C) without detergent and (D) 0.3 mM TX-100. (E) Size distribution histogram of GUV diameters obtained from widefield microscopy, with N = 61. (F) Average lifetime of POPC GUVs with 1% DiI (black) compared to 200 nm POPC LUVSs (red) as a function of TX-100 concentration. Solid lines represent a Hill model fit (R^2 = 0.99 for both). Data shown represents the mean values obtained from 3 experimental runs and error bars denote the standard error of the mean. (G) The change in k value obtained as a function of GUVs vs LUVs labelled with 1% DiI. Error bars are found from the error within the fitting.

GUVs are comprised of a lipid bilayer with an average diameter within the range of 1 - 200 μm. This means that their size and membrane curvature is to an extent, comparable to eukaryotic cells (5 – 100 μm) (*157*). Due to their larger size, they can be also visualised with conventional optical and fluorescence microscopy. The use of widefield microscopy, confirmed that the rehydration method was successful at producing GUVs,

as seen in Figure 4.4A. The average diameter obtained was ~6 μm which is consistent with GUV size and additional features of GUVs can be seen such as membrane blebbing. Blebbing is when the membrane bulges due to a cyclic series of nucleation, expansion and contraction. This is typically due to pressure differences across the membrane. In mammalian cells, blebbing is a feature of several biological processes such as apoptosis and cell division, as well as having implications in tumour invasion (*158*). This observation is also consistent with research that suggests blebbing in GUVs can occur preceding a rearrangement of membrane domains (*159*). Further research how and why this mechanism occurs in model membranes will help better understand cell membrane dynamics which have implications towards drug development in diseases such as tumour progression where blebbing can be seen. It is also clear from the obtained images that GUVs undergo solubilisation, leading to the formation of micelles, as seen in Figure 4.4B. As well as membrane blebbing and micellization, the SEM images shown in Figure 4.4C and D support the previous observations in LUVs of the change in morphology to the toroidal structures. Nevertheless, it is clear from the results that GUVs were created successfully and therefore experiments investigating fluorescence de-quenching of these GUVs could be carried out. As seen in Figure 4.4F, the GUVs exhibited the de-quenching behaviour as a similar sigmoidal curve was witnessed with an eventual plateau at concentrations above the CMC. In contrast to the 200 nm LUVs previously researched, the GUV showed a high initially quenched lifetime of ~0.8 ns. As the diameter in the GUVs are greater than the LUVs, using the same DiI concentration would mean that the fluorophores are more spatially separated across the membrane. This would result in a less self-quenching which would increase the lifetime of the fluorophores. To overcome this problem, a higher DiI concentration would have to be used. Furthermore, GUVs require higher concentrations of detergents to solubilise, as the lifetime begins to plateau around 0.4 mM, with an observed higher half-maximal value of 0.21 mM (Figure 4.4G). One thing that must be noted is the large error bars that can be seen at concentrations around the CMC. This may be due to a limitation with the rehydration method for creating GUVs which is a difficulty to maintain homogeneity in the vesicle population as they bud from the Teflon disk. This can be expected to create a large spread of average lifetimes per sample, as larger GUVs would experience less fluorescence de-quenching. Furthermore, it is difficult to confirm the dye concentration per sample using this method

as it appeared the longer the vesicles were left to swell, the more concentrated the sample was – visually appearing brighter in colour. The simplest way to quantify the concentration is to count the number of vesicles per field of view using an optical microscope however this would not be consistent throughout the whole sample.

4.2 Conclusions and Future Work

The results from this Chapter showed that fluorescence de-quenching behaviour was able to be seen at the single vesicle level – further highlighting the sensitivity and wide range of applications for this technique's use. Furthermore, we are able to build upon these observations and correlate changes in lifetime to sub-solubilising mechanisms of disruption by TX-100. In this, we propose that vesicle expansion and the formation of toroidal-like geometries occurs prior to lysis, and in-tact vesicles undergo structural remodelling that results in expansion up to a saturation value – at which point micelles begin to form and release into the solution. The use of electron microscopy confirmed the swelling behaviour but also revealed that vesicles undergo a conformational change in the presence of TX-100, altering its structure to being toroidal. Further research would benefit from investigating how this change in morphology varies at different detergent concentrations, and if it is specific to TX-100 or occurs with other detergents such as Tween20 and SDS. These findings have implications for various biotechnological applications using detergents, where control over conformation changes is important for desired function, such as drug delivery systems and biotechnological tools.

5. The Disruption of Model Membrane Vesicles by Amyloid-Beta (1-42)

In this Chapter, the use of fluorescence de-quenching will be utilized to explore the effects of neurotoxic $A\beta_{1-42}$ on the membrane, as an insight into its mechanism of disruption in AD. A comparison between monomeric and aggregated forms of the protein will also be investigated, to determine if the protein induces membrane disruption in a similar mechanism to that observed by detergents, and if this behaviour is specific to the aggregation of amyloid.

5.1 Results and Discussion

5.1.1 Monomeric Amyloid has no effect on model membrane vesicles

Having confirmed fluorescence de-quenching as a sensitive indicator of morphological changes in vesicles, the assay was used to investigate disruptions to the membrane by Aβ. 200 nm vesicles of 70% POPC and 30% POPS labelled with 1% DiI were prepared via the extrusion method. This was the chosen lipid composition as it mimics the neuronal membrane composition (*158*). Vesicles were suspended in 5mM SSPE buffer (pH 7.4) and held in a cuvette. $A\beta_{1-42}$ monomers was progressively added to the vesicles in steps of 0.2 μM until a final concentration of 2 μM was achieved, and the resulting amplitude weighted average fluorescent lifetime was measured as previously described, using TCSPC. The final concentration of 2 μM was chosen as previous literature suggests that in neuronal cell cultures, Aβ toxicity is highest within the range of 1 – 10 μM (*160*). The results showed no change in average lifetime, as the concentration of monomeric $A\beta_{1-42}$ increased (Figure 5.1A), indicating a lack of morphological variations during the titration. The lifetime was then measured following 30 minutes, 1 hour, 24 hours and at 1 week, allowing for monomer-membrane interactions to take place in solution. The lifetime decreased by 13.3% after 30 minutes and this value began to rise and eventually stabilise after 1 week (Figure 5.1B). After the week, the lifetime has decreased by 4.1%, suggesting that monomers had little long-term effect.

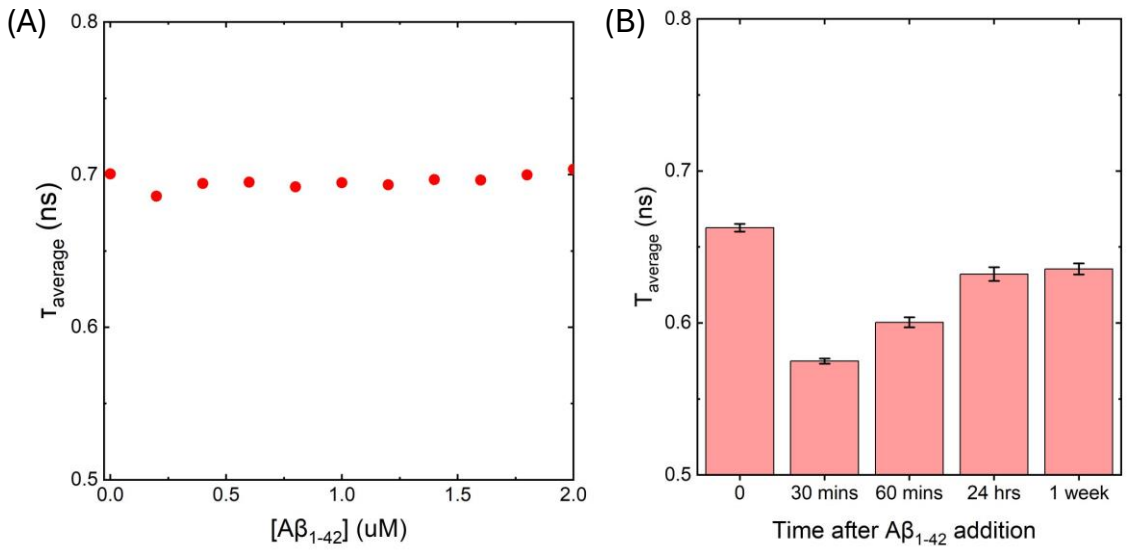

FIGURE 5.1 Increasing concentration of $A\beta_{1-42}$ monomer has minimal effect on fluorescence lifetime both immediately and longer term. A) Average lifetime of PC/PS vesicles with 1% DiI as a function of Aβ concentration. B) Average lifetime of PC/PS vesicles with 1% DiI immediately after addition of 2 μM Aβ as well as 30 minutes, 60 minutes, 24 hours and 1 week later. Error bars represent standard error given by Spectrophotometer.

The results from the lifetime assay, shown in Figure 5.1A, suggests that monomeric amyloid has no immediate effect on the vesicles as the average lifetime component remained ~0.66 ns upon progressive addition of Aβ42. This result is consistent with the literature which suggests that monomeric amyloid generally has little effect on membrane integrity (*161*). In comparison, previous research has suggested that the aggregated forms of Aβ are responsible for the protein's toxic behaviour through mechanisms such as inducing ion-channel like pores in the membrane, activating abnormal signalling pathways, oxidative stress and direct membrane damage (*160*). Despite this, monomeric amyloid remains a target of interest for AD due to its tendency to aggregate into these more aggressive oligomers and fibrils. Furthermore, it is important to investigate the interaction between monomeric amyloid and cell membranes because increasing evidence suggests that this interaction accelerates the accumulation of the protein (*162*). Different membrane characteristics have been suggested to influence the generation of these aggregates. For example, thicker membranes induce Aβ fibril

formation and membrane structural remodelling, and membrane thickness and vesicle area were suggested to be anticorrelated with the incorporation of amyloid (*163*, *164*). As AD is considered a progressive disorder, it is also important to consider the longer-term impact of the protein. As seen in Figure 5.1B, although after 30 minutes the lifetime decreases, suggesting a minimal vesicle-compaction event, this value increases again and eventually stabilises to a value of ~0.63 ns, suggesting recovery of the vesicle to the initial conformation. This further supports the conclusion that monomeric amyloid has little-to-no impact on membrane morphology. Future experiments could provide insight into the decrease seen after 30 minutes, as this experiment alone does not provide a mechanistic explanation. Furthermore the reliability of these results could be verified by the use of a positive control to confirm that the Aβ used in the experiments was functional, for example using cell-based assays to measure the viability of cells, such as neurons, after exposure to the aggregates (*165*, *166*).

5.1.2 Amyloid Aggregates disrupt membranes in a mechanism similar to detergents

Monomeric amyloid aggregation was promoted by suspending the peptide in 500 µL SSPE (pH 7.4) and incubating at 37 °C. After 15 minutes, 30 minutes and 24 hours, 100 µL of the sample was added to 200 nm POPC/POPS vesicles suspended in 5 mM SSPE and held in a cuvette. The amplitude weighted average fluorescence lifetime was measured immediately after amyloid addition, as well as after 30 minutes, 1 hour, 24 hours and 1 week. All the aggregated species increased the average fluorescence lifetime after 1 week (Figure 5.2A). In particular, the early aggregates (15 minutes) and fibrils (24 hours)

had the greatest effect of the different species, with both increasing the lifetime by ~43% (Figure 5.2B).

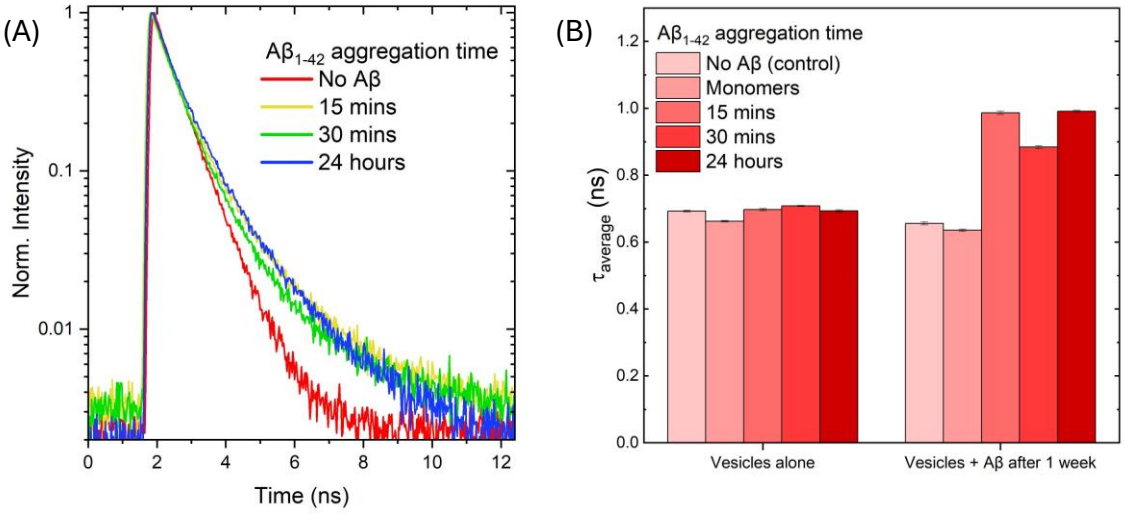

FIGURE 5.2 Average lifetime increases with the addition of amyloid aggregates after 1 week A) Corresponding time-resolved fluorescence decay curves of different amyloid aggregates after 1 week. B) Representative bar charts showing the average lifetime component of 200 nm vesicles with and without the addition of different isoforms of amyloid after 1 week.

The results from this experiment suggest that amyloid aggregates disrupt the membrane via a mechanism that induces spatial separation of the membrane-embedded fluorophores and fluorescence de-quenching. Although monomeric amyloid can be seen to have some biological activity, this effect on the average lifetime is significantly less than that induced by the aggregated forms. The self-assembly of amyloid is highly dependent on local environmental factors such as solution composition, temperature, pressure and pH, therefore incubating the protein in SSPE at 37 °C was chosen to optimally promote aggregation across a rapid timescale (*104*). Samples were taken from the solution after 15 minutes of incubation in these conditions, as an example of early-stage oligomers; 30 minutes, as an example of late-stage oligomers; and 24 hours, as an example of fibrillar amyloid (*167*). All three aggregates significantly increased the average lifetime after 1 week of incubation and these values are significantly greater than for both

monomeric amyloid and no amyloid. Furthermore, the early-stage oligomers and fibrils have the greatest effect. This observation is consistent with previous research which suggested that early-stage aggregates have higher tendencies to interact, permeabilise and cross the plasma membrane whereas late-stage oligomers are more likely to induce the inflammatory response (*167*). This has implications towards the early-stage oligomers being the most toxic. Indeed, the results from this support the idea that the early-stage oligomers and more toxic than the late-stage oligomers as the 15-minute aggregates increased the average lifetime after 1 week to a greater value than the 30-minute aggregates. As a whole, the results suggest that the amyloid aggregates cause an increase in separation between the fluorophores after long term incubation. This suggests a mechanism of disruption that parallels the vesicle disruption induced by detergents seen previously. Indeed, this behaviour has been hypothesised previously – suggesting that amyloid oligomers have a distinct 'detergent-like' effect on lipid bilayers by causing lipid extraction, increased curvature and disruption of the membrane (*121*). Interestingly, this behaviour was implied to occur only with oligomers however the result from the de-quenching assay suggests that this also occurs with fibrils. While the exact mechanism by the different aggregates may differ, both may result in membrane expansion prior to permeabilization.

5.2 Conclusions and Future Work

In this Chapter, fluorescence de-quenching was utilized to explore the interaction between model membrane LUVs and Aβ. Specifically, the proposed detergent like mechanism by the neurotoxic protein during AD progression was investigated to provide a more detailed understanding of the mechanism of membrane perturbation. This work was able to verify that the aggregated species of amyloid are responsible for membrane disruption rather than monomeric species. An increase in amplitude weighted average lifetime was seen after the vesicles were incubated with amyloid for one week, which parallels the increase seen with detergents. This has implications towards a similar mechanism of disruption involving cell membrane remodelling and swelling and expansion prior to the membrane extraction that was previously observed. Further research would be required to prove that this increase in lifetime corresponds to morphological changes in the vesicles however the data presented provides preliminary

evidence supporting this hypothesis. Additional experiments were carried out using SEM to characterise the structure of the aggregates used in the experiments. However, these images revealed the presence of larger aggregates that were likely due to differentiation of aggregates from artefacts within the buffer. This made data analysis extremely challenging and therefore this was not included in the thesis. To overcome this problem, and to better characterise the amyloid present at the different time points, Size Exclusion Chromatography could be used to confirm if the larger aggregates were present throughout the sample or if it was appearing due to crystallisation. Alternatively, techniques such as cryo-electron microscopy or atomic force microscopy could be used to image the different stage aggregates and visualise if these structures change over time.

6. Summary and Conclusions

In conclusion, this thesis has presented fluorescence de-quenching as an appropriate and sensitive technique for reporting on detergent- and protein- induced morphological restructuring and conformational swelling and expansion of intact ensemble and single vesicles. The primary aim of this study was to verify the suitability of the assay for monitoring changes in vesicle morphology during the progressive addition of detergent, in comparison to FRET which is a gold standard reporter in the field. Once the sensitivity was confirmed, environmental parameters (lipid composition, vesicle curvature, dye content) were explored and wider applications of the technique such as protein-membrane interactions were tested. Throughout the investigation, several key findings have been showcased, highlighting mechanisms that underlie these interactions. In particular, data from this thesis suggests that the 3 state model of detergent-induced vesicle solubilisation should be refined to include a step which involves transitions of intact and spherical vesicles to toroidal like structures.

The combination of ensemble and single-vesicle fluorescence de-quenching proves to be a powerful tool for monitoring membrane remodelling, and opens a platform for enabling dynamic, nanometer-scale insights into membrane behaviour. As a single-colour alternative for investigating these changes, this technique is able to bypass complications associated with dual-colour sensing methods such as FRET by avoiding complex fluorophore pairing. Further advantages of the technique include its high adaptability, as it can operate over a range of vesicle and surfactant conditions. It also allows investigation of vesicle structure on a vesicle-by-vesicle bases, bypassing complications associated with ensemble acquisitions.

Utilizing this technique, the sub-solubilising mechanism of detergents was explored to provide insight into how various detergents perturb and damage highly curved vesicles. These results were able to provide insight into an induced swelling event prior to lysis as well as a membrane structural remodelling that transitions intact vesicles to toroidal morphologies. The capacity of both non-ionic and ionic detergent monomers to induce significant morphological rearrangements in model membrane vesicles broadly supports a model of induced solubilisation that involves structural remodelling of intact vesicles prior to lysis. Understanding these structural modifications induced by

surfactants is crucial, as they shine light on the complex mechanism of solubilisation. This opens potential implications for biotechnological applications in which precise control of membrane remodelling is desirable for functionality.

In addition to the detergent studies, fluorescence de-quenching was transferred to use with the neurotoxic protein $A\beta_{1-42}$ to explore its proposed detergent-like effect on membranes. The ensemble fluorescence measurements provide preliminary evidence suggesting that, similarly to detergents, aggregates of the peptide induces conformational changes and promotes morphological variations in highly curved model membrane vesicles after incubation. $A\beta_{1-42}$ is one of the hallmark proteins in AD and the 42-residue peptide in particular is thought to be the most toxic during disease progression. Shining light on the mechanistic details of $A\beta_{1-42}$ membrane interactions may open new opportunities for therapeutic interventions targeting AD.

Bibliography

1. D. Linke, Detergents: an overview. *Methods Enzymol.* **463**, 603–617 (2009).

2. Y. Li, J.-S. Lee, Staring at protein-surfactant interactions: Fundamental approaches and comparative evaluation of their combinations - A review. *Anal. Chim. Acta* **1063**, 18–39 (2019).

3. T. Kundlacz, J. Bender, C. Schmidt, Effects of non-ionic and zwitterionic detergents on soluble proteins during native mass spectrometry experiments. *Int. J. Mass Spectrom.* **468**, 116652 (2021).

4. L. H. Urner, I. Liko, K. Pagel, R. Haag, C. V. Robinson, Non-ionic hybrid detergents for protein delipidation. *Biochim. Biophys. Acta Biomembr.* **1864**, 183958 (2022).

5. J. Jiao, Polyoxyethylated nonionic surfactants and their applications in topical ocular drug delivery. *Adv. Drug Deliv. Rev.* **60**, 1663–1673 (2008).

6. A. Beck, X. Li-Blatter, A. Seelig, J. Seelig, On the interaction of ionic detergents with lipid membranes. Thermodynamic comparison of n-alkyl-+N(CH_3)$_3$ and n-alkyl-SO_4^-. *J. Phys. Chem. B* **114**, 15862–15871 (2010).

7. I. Dapic, L. Baljeu-Neuman, N. Uwugiaren, J. Kers, D. R. Goodlett, G. L. Corthals, Proteome analysis of tissues by mass spectrometry. *Mass Spectrom. Rev.* **38**, 403–441 (2019).

8. A. B. Nowakowski, W. J. Wobig, D. H. Petering, Native SDS-PAGE: high resolution electrophoretic separation of proteins with retention of native properties including bound metal ions. *Metallomics* **6**, 1068–1078 (2014).

9. M. Shehadul Islam, A. Aryasomayajula, P. Selvaganapathy, A review on macroscale and microscale cell lysis methods. *Micromachines (Basel)* **8**, 83 (2017).

10. M. Soulié, A. Deletraz, M. Wehbie, F. Mahler, I. Bouchemal, A. Le Roy, I. Petit-Härtlein, S. Keller, A. Meister, E. Pebay-Peyroula, C. Breyton, C. Ebel, G. Durand, Zwitterionic fluorinated detergents: From design to membrane protein applications. *Biochimie* **205**, 40–52 (2023).

11. I. Bednarz-Misa, P. Serek, B. Dudek, A. Pawlak, G. Bugla-Płoskońska, A. Gamian, Application of zwitterionic detergent to the solubilization of Klebsiella pneumoniae outer membrane proteins for two-dimensional gel electrophoresis. *J. Microbiol. Methods* **107**, 74–79 (2014).

12. S. Luche, V. Santoni, T. Rabilloud, Evaluation of nonionic and zwitterionic detergents as membrane protein solubilizers in two-dimensional electrophoresis. *Proteomics* **3**, 249–253 (2003).

13. P. Champeil, B. de Foresta, M. Picard, C. Gauron, D. Georgin, M. le Maire, J. V. Møller, G. Lenoir, C. Montigny, Interaction of detergents with biological membranes: Comparison of

fluorescence assays with filtration protocols and implications for the rates of detergent association, dissociation and flip-flop. *PLoS One* **14**, e0222932 (2019).

14. D. Koley, A. J. Bard, Triton X-100 concentration effects on membrane permeability of a single HeLa cell by scanning electrochemical microscopy (SECM). *Proc. Natl. Acad. Sci. U. S. A.* **107**, 16783–16787 (2010).

15. B. Mattei, R. B. Lira, K. R. Perez, K. A. Riske, Membrane permeabilization induced by Triton X-100: The role of membrane phase state and edge tension. *Chem. Phys. Lipids* **202**, 28–37 (2017).

16. L. Zhang, X. Chai, P. Sun, B. Yuan, B. Jiang, X. Zhang, M. Liu, The study of the aggregated pattern of TX100 Micelle by using solvent Paramagnetic Relaxation Enhancements. *Molecules* **24**, 1649 (2019).

17. R. J. Robson, E. A. Dennis, The size, shape, and hydration of nonionic surfactant micelles. Triton X-100. *J. Phys. Chem.* **81**, 1075–1078 (1977).

18. U. Anand, C. Jash, S. Mukherjee, Spectroscopic determination of Critical Micelle Concentration in aqueous and non-aqueous media using a non-invasive method. *J. Colloid Interface Sci.* **364**, 400–406 (2011).

19. G. Kaur, S. K. Mehta, Developments of Polysorbate (Tween) based microemulsions: Preclinical drug delivery, toxicity and antimicrobial applications. *Int. J. Pharm.* **529**, 134–160 (2017).

20. J. Chen, Y. Feng, B. Kong, X. Xia, Q. Liu, An eco-friendly extraction method for adsorbed proteins from emulsions stabilized by whey protein isolate by using Tween 20. *Colloids Surf. A Physicochem. Eng. Asp.* **604**, 125332 (2020).

21. S. Hjertén, K. E. Johansson, Selective solubilization with Tween 20 of membrane proteins from Acholeplasma laidlawaii. *Biochim. Biophys. Acta* **288**, 312–325 (1972).

22. H. Knoch, M. H. Ulbrich, J. J. Mittag, J. Buske, P. Garidel, H. Heerklotz, Complex micellization behavior of the polysorbates tween 20 and tween 80. *Mol. Pharm.* **18**, 3147–3157 (2021).

23. M. A. Motin, M. A. Hafiz Mia, A. K. M. Nasimul Islam, Thermodynamic properties of Sodium Dodecyl Sulfate aqueous solutions with Methanol, Ethanol, n-Propanol and iso-Propanol at different temperatures. *J. Saudi Chem. Soc.* **19**, 172–180 (2015).

24. A. Helenius, K. Simons, Solubilization of membranes by detergents. *Biochim. Biophys. Acta* **415**, 29–79 (1975).

25. R. Vittal, H. Gomathi, K.-J. Kim, Beneficial role of surfactants in electrochemistry and in the modification of electrodes. *Adv. Colloid Interface Sci.* **119**, 55–68 (2006).

26. S. Keller, H. Heerklotz, N. Jahnke, A. Blume, Thermodynamics of lipid membrane solubilization by sodium dodecyl sulfate. *Biophys. J.* **90**, 4509–4521 (2006).

27. H. Ahyayauch, M. Bennouna, A. Alonso, F. M. Goñi, Detergent effects on membranes at subsolubilizing concentrations: transmembrane lipid motion, bilayer permeabilization, and vesicle lysis/reassembly are independent phenomena. *Langmuir* **26**, 7307–7313 (2010).

28. E. Opatowski, D. Lichtenberg, M. M. Kozlov, The heat of transfer of lipid and surfactant from vesicles into micelles in mixtures of phospholipid and surfactant. *Biophys. J.* **73**, 1458–1467 (1997).

29. P. A. Dalgarno, J. Juan-Colás, G. J. Hedley, L. Piñeiro, M. Novo, C. Perez-Gonzalez, I. D. W. Samuel, M. C. Leake, S. Johnson, W. Al-Soufi, J. C. Penedo, S. D. Quinn, Unveiling the multi-step solubilization mechanism of sub-micron size vesicles by detergents. *Sci. Rep.* **9**, 12897 (2019).

30. D. R. Perinelli, M. Cespi, N. Lorusso, G. F. Palmieri, G. Bonacucina, P. Blasi, Surfactant self-assembling and critical Micelle concentration: One approach fits all? *Langmuir* **36**, 5745–5753 (2020).

31. H. Li, D. Hu, F. Liang, X. Huang, Q. Zhu, Influence factors on the critical micelle concentration determination using pyrene as a probe and a simple method of preparing samples. *R. Soc. Open Sci.* **7**, 192092 (2020).

32. Y. Moroi, N. Nishikido, M. Saito, R. Matuura, The critical micelle concentration of ionic-nonionic detergent mixtures in aqueous solutions. III. *J. Colloid Interface Sci.* **52**, 356–363 (1975).

33. T. Tadros, "Critical Micelle Concentration" in *Encyclopedia of Colloid and Interface Science* (Springer Berlin Heidelberg, Berlin, Heidelberg, 2013), pp. 209–210.

34. A. D. Berman, S. D. Cameron, J. N. Israelachvili, Mobility of surfactants in and between adsorbed monolayers. *J. Phys. Chem. B* **101**, 5692–5697 (1997).

35. A. A. Gurtovenko, I. Vattulainen, Molecular mechanism for lipid flip-flops. *J. Phys. Chem. B* **111**, 13554–13559 (2007).

36. M. G. Lete, B. G. Monasterio, M. I. Collado, M. Medina, J. Sot, A. Alonso, F. M. Goñi, Fast and slow biomembrane solubilizing detergents: Insights into their mechanism of action. *Colloids Surf. B Biointerfaces* **183**, 110430 (2019).

37. V. A. Bjørnestad, R. Lund, Pathways of membrane solubilization: A structural study of model lipid vesicles exposed to classical detergents. *Langmuir* **39**, 3914–3933 (2023).

38. F.-X. Contreras, L. Sánchez-Magraner, A. Alonso, F. M. Goñi, Transbilayer (flip-flop) lipid motion and lipid scrambling in membranes. *FEBS Lett.* **584**, 1779–1786 (2010).

39. D. Lichtenberg, H. Ahyayauch, A. Alonso, F. M. Goñi, Detergent solubilization of lipid bilayers: a balance of driving forces. *Trends Biochem. Sci.* **38**, 85–93 (2013).

40. D. Lichtenberg, H. Ahyayauch, F. M. Goñi, The mechanism of detergent solubilization of lipid bilayers. *Biophys. J.* **105**, 289–299 (2013).

41. L. Hua, S. Akcesme, K. Müller, H. Heerklotz, A roadmap of responses to asymmetry stress in lipid membranes. *J. Phys. Chem. B* **129**, 1260–1273 (2025).

42. A. Hossein, M. Deserno, Spontaneous curvature, differential stress, and bending modulus of asymmetric lipid membranes. *Biophys. J.* **118**, 624–642 (2020).

43. Y.-H. M. Chan, S. G. Boxer, Model membrane systems and their applications. *Curr. Opin. Chem. Biol.* **11**, 581–587 (2007).

44. C. Huang, D. Quinn, Y. Sadovsky, S. Suresh, K. J. Hsia, Formation and size distribution of self-assembled vesicles. *Proc. Natl. Acad. Sci. U. S. A.* **114**, 2910–2915 (2017).

45. G. Zhang, J. Sun, Lipid in chips: A brief review of liposomes formation by microfluidics. *Int. J. Nanomedicine* **16**, 7391–7416 (2021).

46. M. A. Khan, S. Anand, S. K. Deshmukh, S. Singh, A. P. Singh, Determining the size distribution and integrity of extracellular vesicles by dynamic Light Scattering. *Methods Mol. Biol.* **2413**, 165–175 (2022).

47. N. Comfort, K. Cai, T. R. Bloomquist, M. D. Strait, A. W. Ferrante Jr, A. A. Baccarelli, Nanoparticle tracking analysis for the quantification and size determination of extracellular vesicles. *J. Vis. Exp.*, doi: 10.3791/62447 (2021).

48. R. Pan, D. Chen, L. Hou, R. Hu, Z. Jiao, Small extracellular vesicles: a novel drug delivery system for neurodegenerative disorders. *Front. Aging Neurosci.* **15**, 1184435 (2023).

49. A. Luchini, G. Vitiello, Mimicking the mammalian plasma membrane: An overview of lipid membrane models for biophysical studies. *Biomimetics (Basel)* **6**, 3 (2020).

50. Y.-W. Hsueh, M.-T. Chen, P. J. Patty, C. Code, J. Cheng, B. J. Frisken, M. Zuckermann, J. Thewalt, Ergosterol in POPC membranes: physical properties and comparison with structurally similar sterols. *Biophys. J.* **92**, 1606–1615 (2007).

51. F. M. Goñi, A. Alonso, Spectroscopic techniques in the study of membrane solubilization, reconstitution and permeabilization by detergents. *Biochim. Biophys. Acta* **1508**, 51–68 (2000).

52. H. Niroomand, G. A. Venkatesan, S. A. Sarles, D. Mukherjee, B. Khomami, Lipid-detergent phase transitions during detergent-mediated liposome solubilization. *J. Membr. Biol.* **249**, 523–538 (2016).

53. L. Dresser, S. P. Graham, L. M. Miller, C. Schaefer, D. Conteduca, S. Johnson, M. C. Leake, S. D. Quinn, Tween-20 induces the structural remodeling of single lipid vesicles. *J. Phys. Chem. Lett.*, 5341–5350 (2022).

54. L. G. Dresser, C. Kunstmann-Olsen, D. Conteduca, C. M. Hofmair, N. Smith, L. Clark, S. Johnson, J. C. Penedo, M. C. Leake, S. D. Quinn, Multiple intermediates in the detergent-induced fusion of lipid vesicles. *Commun. Mater.* **5**, 1–12 (2024).

55. J. Juan-Colás, L. Dresser, K. Morris, H. Lagadou, R. H. Ward, A. Burns, S. Tear, S. Johnson, M. C. Leake, S. D. Quinn, The mechanism of vesicle solubilization by the detergent sodium dodecyl sulfate. *Langmuir* **36**, 11499–11507 (2020).

56. V. Pandey, T. Pandey, Biophysical significance of fluorescence spectroscopy in deciphering nucleic acid dynamics: From fundamental to recent advancements. *Biophys. Chem.* **316**, 107345 (2025).

57. J. V. Jun, D. M. Chenoweth, E. J. Petersson, Rational design of small molecule fluorescent probes for biological applications. *Org. Biomol. Chem.* **18**, 5747–5763 (2020).

58. B. Y. Michel, D. Dziuba, R. Benhida, A. P. Demchenko, A. Burger, Probing of nucleic acid structures, dynamics, and interactions with environment-sensitive fluorescent labels. *Front. Chem.* **8**, 112 (2020).

59. B. R. Casadei, C. C. Domingues, E. de Paula, K. A. Riske, Direct visualization of the action of Triton X-100 on giant vesicles of erythrocyte membrane lipids. *Biophys. J.* **106**, 2417–2425 (2014).

60. M. Dezi, A. Di Cicco, P. Bassereau, D. Lévy, Detergent-mediated incorporation of transmembrane proteins in giant unilamellar vesicles with controlled physiological contents. *Proc. Natl. Acad. Sci. U. S. A.* **110**, 7276–7281 (2013).

61. E. Pantaler, D. Kamp, C. W. Haest, Acceleration of phospholipid flip-flop in the erythrocyte membrane by detergents differing in polar head group and alkyl chain length. *Biochim. Biophys. Acta* **1509**, 397–408 (2000).

62. X. Han, Y. Wang, Y. Huang, X. Wang, J. Choo, L. Chen, Fluorescent probes for biomolecule detection under environmental stress. *J. Hazard. Mater.* **431**, 128527 (2022).

63. V. I. Martynov, A. A. Pakhomov, N. V. Popova, I. E. Deyev, A. G. Petrenko, Synthetic fluorophores for visualizing biomolecules in living systems. *Acta Naturae* **8**, 33–46 (2016).

64. J. F. Bille, Ed., *High Resolution Imaging in Microscopy and Ophthalmology: New Frontiers in Biomedical Optics* (Springer Nature, Cham, Switzerland, ed. 2019, 2019).

65. D. E. Wolf, Fundamentals of fluorescence and fluorescence microscopy. *Methods Cell Biol.* **114**, 69–97 (2013).

66. M. R. Ganjali, V. K. Gupta, F. Faridbod, P. Norouzi, "Spectrometric Determination of Lanthanides Series" in *Lanthanides Series Determination by Various Analytical Methods* (Elsevier, 2016), pp. 209–358.

67. J. R. Lakowicz, *Principles of Fluorescence Spectroscopy* (Springer, New York, NY, ed. 3, 2006).

68. L. L. Bruce, M. A. Christensen, B. Fritzsch, Electron microscopic differentiation of directly and transneuronally transported DiI and applications for studies of synaptogenesis. *J. Neurosci. Methods* **73**, 107–112 (1997).

69. M. C. Leake, *Biophysics* (CRC Press, London, England, 2016; http://dx.doi.org/10.1201/9781315381589).

70. C. Cheng, O. Trzcinski, L. C. Doering, Fluorescent labeling of dendritic spines in cell cultures with the carbocyanine dye â€œDiIâ€. *Front. Neuroanat.* **8**, 30 (2014).

71. E. Sobakinskaya, M. Schmidt Am Busch, T. Renger, Theory of FRET “spectroscopic ruler” for short distances: Application to polyproline. *J. Phys. Chem. B* **122**, 54–67 (2018).

72. R. Roy, S. Hohng, T. Ha, A practical guide to single-molecule FRET. *Nat. Methods* **5**, 507–516 (2008).

73. W. Bae, T.-Y. Yoon, C. Jeong, Direct evaluation of self-quenching behavior of fluorophores at high concentrations using an evanescent field. *PLoS One* **16**, e0247326 (2021).

74. T. R. Evans, Singlet quenching mechanisms. *J. Am. Chem. Soc.* **93**, 2081–2082 (1971).

75. I. López Arbeloa, Dimeric and trimeric states of the fluorescein dianion. Part 2.—Effects on fluorescence characteristics. *J. Chem. Soc.* **77**, 1735–1742 (1981).

76. R. F. Chen, J. R. Knutson, Mechanism of fluorescence concentration quenching of carboxyfluorescein in liposomes: energy transfer to nonfluorescent dimers. *Anal. Biochem.* **172**, 61–77 (1988).

77. S. A. Meredith, Y. Kusunoki, S. D. Connell, K. Morigaki, S. D. Evans, P. G. Adams, Self-quenching behavior of a fluorescent probe incorporated within lipid membranes explored using electrophoresis and fluorescence lifetime imaging microscopy. *J. Phys. Chem. B* **127**, 1715–1727 (2023).

78. K. K. Siddappaji, S. Gopal, Molecular mechanisms in Alzheimer’s disease and the impact of physical exercise with advancements in therapeutic approaches. *AIMS Neurosci.* **8**, 357–389 (2021).

79. N. Cloak, C. Schoo, Y. Al Khalili, “Behavioral and psychological symptoms in dementia” in *StatPearls* (StatPearls Publishing, Treasure Island (FL), 2025).

80. Y. Chen, P. Bandosz, G. Stoye, Y. Liu, Y. Wu, S. Lobanov-Rostovsky, E. French, M. Kivimaki, G. Livingston, J. Liao, E. J. Brunner, Dementia incidence trend in England and Wales, 2002-19, and projection for dementia burden to 2040: analysis of data from the English Longitudinal Study of Ageing. *Lancet Public Health* **8**, e859–e867 (2023).

81. V. D’Argenio, R. Tomaiuolo, S. Bargeri, G. Sancesario, Alzheimer’s 2030: From precision genomics to Artificial Intelligence. *Genes (Basel)* **17**, 233 (2026).

82. R. D. by Age, Deaths registered in England and wales: 2024. https://backup.ons.gov.uk/wp-content/uploads/sites/3/2025/10/Deaths-registered-in-England-and-Wales-2024.pdf.

83. M. A. DeTure, D. W. Dickson, The neuropathological diagnosis of Alzheimer's disease. *Mol. Neurodegener.* **14**, 32 (2019).

84. A. Mietelska-Porowska, U. Wasik, M. Goras, A. Filipek, G. Niewiadomska, Tau protein modifications and interactions: their role in function and dysfunction. *Int. J. Mol. Sci.* **15**, 4671–4713 (2014).

85. P. V. Arriagada, J. H. Growdon, E. T. Hedley-Whyte, B. T. Hyman, Neurofibrillary tangles but not senile plaques parallel duration and severity of Alzheimer's disease. *Neurology* **42**, 631–639 (1992).

86. R. Medeiros, D. Baglietto-Vargas, F. M. LaFerla, The role of tau in Alzheimer's disease and related disorders: Role of tau in AD and related disorders. *CNS Neurosci. Ther.* **17**, 514–524 (2011).

87. H. Zhang, W. Wei, M. Zhao, L. Ma, X. Jiang, H. Pei, Y. Cao, H. Li, Interaction between Aβ and tau in the pathogenesis of Alzheimer's disease. *Int. J. Biol. Sci.* **17**, 2181–2192 (2021).

88. G. Mairet-Coello, J. Courchet, S. Pieraut, V. Courchet, A. Maximov, F. Polleux, The CAMKK2-AMPK kinase pathway mediates the synaptotoxic effects of Aβ oligomers through Tau phosphorylation. *Neuron* **78**, 94–108 (2013).

89. K. T. Dineley, M. Westerman, D. Bui, K. Bell, K. H. Ashe, J. D. Sweatt, Beta-amyloid activates the mitogen-activated protein kinase cascade via hippocampal alpha7 nicotinic acetylcholine receptors: In vitro and in vivo mechanisms related to Alzheimer's disease. *J. Neurosci.* **21**, 4125–4133 (2001).

90. H. Motaln, B. Rogelj, The role of c-Abl tyrosine kinase in brain and its pathologies. *Cells* **12** (2023).

91. K. P. Kepp, N. K. Robakis, P. F. Høilund-Carlsen, S. L. Sensi, B. Vissel, The amyloid cascade hypothesis: an updated critical review. *Brain* **146**, 3969–3990 (2023).

92. R. Ricciarelli, E. Fedele, The amyloid cascade hypothesis in Alzheimer's disease: It's time to change our mind. *Curr. Neuropharmacol.* **15**, 926–935 (2017).

93. M. M. Rahman, C. Lendel, Extracellular protein components of amyloid plaques and their roles in Alzheimer's disease pathology. *Mol. Neurodegener.* **16**, 59 (2021).

94. L. Gu, Z. Guo, Alzheimer's Aβ42 and Aβ40 peptides form interlaced amyloid fibrils. *J. Neurochem.* **126**, 305–311 (2013).

95. G.-F. Chen, T.-H. Xu, Y. Yan, Y.-R. Zhou, Y. Jiang, K. Melcher, H. E. Xu, Amyloid beta: structure, biology and structure-based therapeutic development. *Acta Pharmacol. Sin.* **38**, 1205–1235 (2017).

96. T. Iwatsubo, A. Odaka, N. Suzuki, H. Mizusawa, N. Nukina, Y. Ihara, Visualization of Aβ42(43) and Aβ40 in senile plaques with end-specific Aβ monoclonals: Evidence that an initially deposited species is Aβ42(43). *Neuron* **13**, 45–53 (1994).

97. D. Im, T. S. Choi, Distinctive contribution of two additional residues in protein aggregation of Aβ42 and Aβ40 isoforms. *BMB Rep.* **57**, 263–272 (2024).

98. A. Balupuri, K.-E. Choi, N. S. Kang, Aggregation mechanism of Alzheimer's amyloid β-peptide mediated by α-strand/α-sheet structure. *Int. J. Mol. Sci.* **21**, 1094 (2020).

99. M. Wogulis, S. Wright, D. Cunningham, T. Chilcote, K. Powell, R. E. Rydel, Nucleation-dependent polymerization is an essential component of amyloid-mediated neuronal cell death. *J. Neurosci.* **25**, 1071–1080 (2005).

100. W.-F. Xue, S. W. Homans, S. E. Radford, Systematic analysis of nucleation-dependent polymerization reveals new insights into the mechanism of amyloid self-assembly. *Proc. Natl. Acad. Sci. U. S. A.* **105**, 8926–8931 (2008).

101. E. Chatani, N. Yamamoto, Recent progress on understanding the mechanisms of amyloid nucleation. *Biophys. Rev.* **10**, 527–534 (2018).

102. E. Axell, J. Hu, M. Lindberg, A. J. Dear, L. Ortigosa-Pascual, E. A. Andrzejewska, G. Šneiderienė, D. Thacker, T. P. J. Knowles, E. Sparr, S. Linse, The role of shear forces in primary and secondary nucleation of amyloid fibrils. *Proc. Natl. Acad. Sci. U. S. A.* **121**, e2322572121 (2024).

103. L. Wang, K. Eom, T. Kwon, Different aggregation pathways and structures for Aβ40 and Aβ42 peptides. *Biomolecules* **11**, 198 (2021).

104. S. D. Quinn, P. A. Dalgarno, R. T. Cameron, G. J. Hedley, C. Hacker, J. M. Lucocq, G. S. Baillie, I. D. W. Samuel, J. C. Penedo, Real-time probing of β-amyloid self-assembly and inhibition using fluorescence self-quenching between neighbouring dyes. *Mol. Biosyst.* **10**, 34–44 (2014).

105. M. Sunde, L. C. Serpell, M. Bartlam, P. E. Fraser, M. B. Pepys, C. C. Blake, Common core structure of amyloid fibrils by synchrotron X-ray diffraction. *J. Mol. Biol.* **273**, 729–739 (1997).

106. M. Kollmer, K. Meinhardt, C. Haupt, F. Liberta, M. Wulff, J. Linder, L. Handl, L. Heinrich, C. Loos, M. Schmidt, T. Syrovets, T. Simmet, P. Westermark, G. T. Westermark, U. Horn, V. Schmidt, P. Walther, M. Fändrich, Electron tomography reveals the fibril structure and lipid interactions in amyloid deposits. *Proc. Natl. Acad. Sci. U. S. A.* **113**, 5604–5609 (2016).

107. S. Li, Detergents and alternatives in cryo-EM studies of membrane proteins. *Acta Biochim. Biophys. Sin. (Shanghai)* **54**, 1049–1056 (2022).

108. S. Han, M. Kollmer, D. Markx, S. Claus, P. Walther, M. Fändrich, Amyloid plaque structure and cell surface interactions of β-amyloid fibrils revealed by electron tomography. *Sci. Rep.* **7**, 43577 (2017).

109. S. A. Kotler, P. Walsh, J. R. Brender, A. Ramamoorthy, Differences between amyloid-β aggregation in solution and on the membrane: insights into elucidation of the mechanistic details of Alzheimer's disease. *Chem. Soc. Rev.* **43**, 6692–6700 (2014).

110. T. L. Williams, L. C. Serpell, Membrane and surface interactions of Alzheimer's Aβ peptide--insights into the mechanism of cytotoxicity: Membrane interactions of Alzheimer's Aβ peptide. *FEBS J.* **278**, 3905–3917 (2011).

111. M. Verma, A. Vats, V. Taneja, Toxic species in amyloid disorders: Oligomers or mature fibrils. *Ann. Indian Acad. Neurol.* **18**, 138–145 (2015).

112. R. Kayed, Y. Sokolov, B. Edmonds, T. M. McIntire, S. C. Milton, J. E. Hall, C. G. Glabe, Permeabilization of lipid bilayers is a common conformation-dependent activity of soluble amyloid oligomers in protein misfolding diseases. *J. Biol. Chem.* **279**, 46363–46366 (2004).

113. D. V. Zaretsky, M. V. Zaretskaia, Intracellular ion changes induced by the exposure to beta-amyloid can be explained by the formation of channels in the lysosomal membranes. *Biochim. Biophys. Acta Mol. Cell Res.* **1869**, 119145 (2022).

114. D. C. Bode, M. D. Baker, J. H. Viles, Ion channel formation by amyloid-β42 oligomers but not amyloid-β40 in cellular membranes. *J. Biol. Chem.* **292**, 1404–1413 (2017).

115. H. H. Jarosz-Griffiths, E. Noble, J. V. Rushworth, N. M. Hooper, Amyloid-β receptors: The Good, the bad, and the prion protein. *J. Biol. Chem.* **291**, 3174–3183 (2016).

116. S. Guntupalli, J. Widagdo, V. Anggono, Amyloid-β-induced dysregulation of AMPA receptor trafficking. *Neural Plast.* **2016**, 3204519 (2016).

117. K. Taniguchi, F. Yamamoto, A. Amano, A. Tamaoka, N. Sanjo, T. Yokota, F. Kametani, W. Araki, Amyloid-β oligomers interact with NMDA receptors containing GluN2B subunits and metabotropic glutamate receptor 1 in primary cortical neurons: Relevance to the synapse pathology of Alzheimer's disease. *Neurosci. Res.* **180**, 90–98 (2022).

118. C. Cheignon, M. Tomas, D. Bonnefont-Rousselot, P. Faller, C. Hureau, F. Collin, Oxidative stress and the amyloid beta peptide in Alzheimer's disease. *Redox Biol.* **14**, 450–464 (2018).

119. L. Milanesi, T. Sheynis, W.-F. Xue, E. V. Orlova, A. L. Hellewell, R. Jelinek, E. W. Hewitt, S. E. Radford, H. R. Saibil, Direct three-dimensional visualization of membrane disruption by amyloid fibrils. *Proc. Natl. Acad. Sci. U. S. A.* **109**, 20455–20460 (2012).

120. J. R. Brender, S. Salamekh, A. Ramamoorthy, Membrane disruption and early events in the aggregation of the diabetes related peptide IAPP from a molecular perspective. *Acc. Chem. Res.* **45**, 454–462 (2012).

121. D. C. Bode, M. Freeley, J. Nield, M. Palma, J. H. Viles, Amyloid-β oligomers have a profound detergent-like effect on lipid membrane bilayers, imaged by atomic force and electron microscopy. *J. Biol. Chem.* **294**, 7566–7572 (2019).

122. L. D. Mayer, M. J. Hope, P. R. Cullis, Vesicles of variable sizes produced by a rapid extrusion procedure. *Biochim. Biophys. Acta* **858**, 161–168 (1986).

123. T. F. Zhu, I. Budin, J. W. Szostak, Vesicle extrusion through polycarbonate track-etched membranes using a hand-held mini-extruder. *Methods Enzymol.* **533**, 275–282 (2013).

124. H. Nsairat, D. Khater, U. Sayed, F. Odeh, A. Al Bawab, W. Alshaer, Liposomes: structure, composition, types, and clinical applications. *Heliyon* **8**, e09394 (2022).

125. S. A. Spinella, R. B. Nelson, D. E. Elmore, Measuring peptide translocation into large unilamellar vesicles. *J. Vis. Exp.*, e3571 (2012).

126. E. Rideau, F. R. Wurm, K. Landfester, Self-assembly of giant unilamellar vesicles by film hydration methodologies. *Adv. Biosyst.* **3**, e1800324 (2019).

127. J. Stetefeld, S. A. McKenna, T. R. Patel, Dynamic light scattering: a practical guide and applications in biomedical sciences. *Biophys. Rev.* **8**, 409–427 (2016).

128. M. Wahl, Time-correlated single photon counting. https://www.picoquant.com/images/uploads/page/files/7253/technote_tcspc.pdf.

129. M. C. Leake, S. D. Quinn, A guide to small fluorescent probes for single-molecule biophysics. *Chem. Phys. Rev.* **4** (2023).

130. D. S. Talaga, Information-theoretical analysis of time-correlated single-photon counting measurements of single molecules. *J. Phys. Chem. A* **113**, 5251–5263 (2009).

131. Rahul Chib, Sunil Shah, Zygmunt Gryczynski, Rafal Fudala, Julian Borejdo, Bogumil Zelent, Maria G Corradini, Richard D Ludescher and Ignacy Gryczynski, Standard reference for instrument response function in fluorescence lifetime measurements in visible and near infrared (2015). https://iopscience.iop.org/article/10.1088/0957-0233/27/2/027001/pdf.

132. A. M. Nagy, F. O. Talbot, M. F. Czar, R. A. Jockusch, Fluorescence lifetimes of rhodamine dyes in vacuo. *J. Photochem. Photobiol. A Chem.* **244**, 47–53 (2012).

133. S. Shimizu, N. Matubayasi, Cooperativity in micellar solubilization. *Phys. Chem. Chem. Phys.* **23**, 8705–8716 (2021).

134. C. Oelsner, F. Birke, E. Ermilov, D. Gerber, V. Buschmann, A. Devaux, R. Erdmann, Measuring steady-state and time-resolved photoluminescence from a positionable, micrometer-sized observation volume with the FluoMic Microscope. https://www.picoquant.com/images/uploads/downloads/applicationnote_fluomic.pdf.

135. J. M. Dickhout Wetsus, European Centre of Excellence for Sustainable Water Technology, Oostergoweg 9, 8911 MA Leeuwarden, The Netherlands, J. M. Kleijn, R. G. H. Lammertink, W. M. de Vos, Adhesion of emulsified oil droplets to hydrophilic and hydrophobic surfaces - effect of surfactant charge, surfactant concentration and ionic strength. *Soft Matter* **14**, 5452–5460 (2018).

136. W. H. Venable Jr, Spectrophotometric Standards. *J. Res. Natl. Bur. Stand. A Phys. Chem.* **76A**, 509–510 (1972).

137. W. R. Algar, N. Hildebrandt, S. S. Vogel, I. L. Medintz, FRET as a biomolecular research tool - understanding its potential while avoiding pitfalls. *Nat. Methods* **16**, 815–829 (2019).

138. R. B. Sekar, A. Periasamy, Fluorescence resonance energy transfer (FRET) microscopy imaging of live cell protein localizations. *J. Cell Biol.* **160**, 629–633 (2003).

139. S. L. Yefimova, T. N. Tkacheva, I. Y. Kurilchenko, A. V. Sorokin, Y. V. Malyukin, Spectroscopic study of interactions between dye molecules in micelle and liposome nanovolumes. *J. Appl. Spectrosc.* **79**, 914–921 (2013).

140. I. Sychugov, "Micro-photoluminescence (μ-PL)" in *Lecture Notes in Nanoscale Science and Technology* (Springer International Publishing, Cham, 2023), pp. 55–86.

141. V. I. Shcheslavskiy, M. V. Shirmanova, K. S. Yashin, A. C. Rück, M. C. Skala, W. Becker, Fluorescence lifetime imaging techniques-A review on principles, applications and clinical relevance. *J. Biophotonics*, e202400450 (2025).

142. E. R. Fischer, B. T. Hansen, V. Nair, F. H. Hoyt, D. W. Dorward, Scanning electron microscopy. *Curr. Protoc. Microbiol.* **Chapter 2**, Unit 2B.2. (2012).

143. C. G. Golding, L. L. Lamboo, D. R. Beniac, T. F. Booth, The scanning electron microscope in microbiology and diagnosis of infectious disease. *Sci. Rep.* **6**, 26516 (2016).

144. T. P. Sudbrack, N. L. Archilha, R. Itri, K. A. Riske, Observing the solubilization of lipid bilayers by detergents with optical microscopy of GUVs. *J. Phys. Chem. B* **115**, 269–277 (2011).

145. N. A. N. Hanafy, M. El-Kemary, S. Leporatti, Micelles structure development as a strategy to improve smart cancer therapy. *Cancers (Basel)* **10** (2018).

146. G. Zazeri, A. P. R. Povinelli, M. de F. Lima, M. L. Cornélio, Detailed characterization of the cooperative binding of piperine with heat shock protein 70 by molecular biophysical approaches. *Biomedicines* **8**, 629 (2020).

147. J. E. Berlier, A. Rothe, G. Buller, J. Bradford, D. R. Gray, B. J. Filanoski, W. G. Telford, S. Yue, J. Liu, C.-Y. Cheung, W. Chang, J. D. Hirsch, J. M. Beechem, R. P. Haugland, R. P. Haugland, Quantitative comparison of long-wavelength Alexa Fluor dyes to Cy dyes: fluorescence of the dyes and their bioconjugates. *J. Histochem. Cytochem.* **51**, 1699–1712 (2003).

148. P. Jurkiewicz, L. Cwiklik, A. Vojtíšková, P. Jungwirth, M. Hof, Structure, dynamics, and hydration of POPC/POPS bilayers suspended in NaCl, KCl, and CsCl solutions. *Biochim. Biophys. Acta* **1818**, 609–616 (2012).

149. N.-F. Lipp, R. Gautier, M. Magdeleine, M. Renard, V. Albanèse, A. Čopič, G. Drin, An electrostatic switching mechanism to control the lipid transfer activity of Osh6p. *Nat. Commun.* **10**, 3926 (2019).

150. T. A. Hartjes, S. Mytnyk, G. W. Jenster, V. van Steijn, M. E. van Royen, Extracellular vesicle quantification and characterization: Common methods and emerging approaches. *Bioengineering (Basel)* **6** (2019).

151. A. V. Malm, J. C. W. Corbett, Improved Dynamic Light Scattering using an adaptive and statistically driven time resolved treatment of correlation data. *Sci. Rep.* **9**, 13519 (2019).

152. V. Filipe, A. Hawe, W. Jiskoot, Critical evaluation of Nanoparticle Tracking Analysis (NTA) by NanoSight for the measurement of nanoparticles and protein aggregates. *Pharm. Res.* **27**, 796–810 (2010).

153. S. Klisch, D. Gilbert, E. Breaux, A. Dalier, S. Gupta, B. Jakobi, G. J. Schneider, Building a simplistic automatic extruder: Instrument development opportunities for the laboratory. *J. Chem. Educ.* **101**, 3292–3300 (2024).

154. A. Kaur, P. Kaur, S. Ahuja, Förster resonance energy transfer (FRET) and applications thereof. *Anal. Methods* **12**, 5532–5550 (2020).

155. S. Kundu, S. Panigrahi, A. Pal, S. K. Ghosh, S. Nath, S. Praharaj, S. Basu, T. Pal, Dye–micelle aggregate formation for effective photobleaching. *Dyes Pigm.* **69**, 177–184 (2006).

156. G. K R, R. Balenahalli Narasingappa, G. Vishnu Vyas, Unveiling mechanisms of antimicrobial peptide: Actions beyond the membranes disruption. *Heliyon* **10**, e38079 (2024).

157. Z. Boban, I. Mardešić, W. K. Subczynski, M. Raguz, Giant unilamellar vesicle electroformation: What to use, what to avoid, and how to quantify the results. *Membranes (Basel)* **11**, 860 (2021).

158. M. A. Khajah, Y. A. Luqmani, Involvement of membrane blebbing in immunological disorders and cancer. *Med. Princ. Pract.* **25 Suppl 2**, 18–27 (2016).

159. G. Dhanawat, M. Dey, A. Singh, N. Parveen, Invagination of giant unilamellar vesicles upon membrane mixing with native vesicles. *ACS Omega* **9**, 46615–46626 (2024).

160. I. Kuperstein, K. Broersen, I. Benilova, J. Rozenski, W. Jonckheere, M. Debulpaep, A. Vandersteen, I. Segers-Nolten, K. Van Der Werf, V. Subramaniam, D. Braeken, G. Callewaert, C. Bartic, R. D'Hooge, I. C. Martins, F. Rousseau, J. Schymkowitz, B. De Strooper, Neurotoxicity of Alzheimer's disease Aβ peptides is induced by small changes in the Aβ42 to Aβ40 ratio. *EMBO J.* **29**, 3408–3420 (2010).

161. Y. Tian, J. Liu, F. Yang, C. Lian, H. Zhang, J. H. Viles, Z. Li, Therapeutic potential for amyloid surface inhibitor: only amyloid-β oligomers formed by secondary nucleation disrupt lipid membrane integrity. *FEBS J.* **289**, 6767–6781 (2022).

162. A. Khondker, R. J. Alsop, M. C. Rheinstädter, Membrane-accelerated amyloid-β aggregation and formation of cross-β sheets. *Membranes (Basel)* **7**, 49 (2017).

163. Z. Niu, Z. Zhang, W. Zhao, J. Yang, Interactions between amyloid β peptide and lipid membranes. *Biochim. Biophys. Acta Biomembr.* **1860**, 1663–1669 (2018).

164. K. J. Korshavn, C. Satriano, Y. Lin, R. Zhang, M. Dulchavsky, A. Bhunia, M. I. Ivanova, Y.-H. Lee, C. La Rosa, M. H. Lim, A. Ramamoorthy, Reduced lipid bilayer thickness regulates the aggregation and cytotoxicity of amyloid-β. *J. Biol. Chem.* **292**, 4638–4650 (2017).

165. H. Long, S. Zeng, D. Li, Cellular and animal models to investigate pathogenesis of amyloid aggregation in neurodegenerative diseases. *Biophys. Rep.* **8**, 14–28 (2022).

166. L. B. J. McIntire, N. Landman, M. S. Kang, G. M. Finan, J. C. Hwang, A. Z. Moore, L. S. Park, C.-S. Lin, T.-W. Kim, Phenotypic assays for β-amyloid in mouse embryonic stem cell-derived neurons. *Chem. Biol.* **20**, 956–967 (2013).

167. S. De, D. C. Wirthensohn, P. Flagmeier, C. Hughes, F. A. Aprile, F. S. Ruggeri, D. R. Whiten, D. Emin, Z. Xia, J. A. Varela, P. Sormanni, F. Kundel, T. P. J. Knowles, C. M. Dobson, C. Bryant, M. Vendruscolo, D. Klenerman, Different soluble aggregates of Aβ42 can give rise to cellular toxicity through different mechanisms. *Nat. Commun.* **10**, 1541 (2019).